

Nanoindentation Based Estimates of Flexoelectric Properties of Piezoelectric
Crystals

A Thesis

Presented to

the Faculty of the Interdisciplinary Program in Materials Engineering

University of Houston

In Partial Fulfillment

of the Requirements for the Degree

Master of Science

in Materials Engineering

by

Cody R. Robinson

May 2012

This work is dedicated in memory of my grandfather, Bose Emmett Robinson, aunt,
Wendy Marchelle Smith, great grandmother, Emily Lois Hewitt, grandmother, Lois
Yvonne Collard, and friend, Jimmy Lee Brigance.

Acknowledgements

Through most of my undergraduate education, I gave little consideration to the pursuit of an advanced degree. By my senior year, however, my professional interests in materials engineering and the encouragement of many personal and professional associates led me to accept an opportunity for graduate studies presented by Dr. Ken White. I am very grateful for Dr. White's support and guidance in my time as a graduate student as well as his willingness to let me influence the paths of my research and coursework in directions I believed to be most valuable and appropriate.

I would like to thank committee members Dr. Pradeep Sharma and Dr. Ashutosh Agrawal for taking the time to review and consider this work. I also wish to acknowledge Dr. Mohammed Gharbi for many insightful discussions throughout this project.

My family, as well as many friends and teachers, deserve a great deal of credit for their support and interest in my academic and professional endeavors. I cannot overstate how grateful I am for my parents who have gone to extraordinary lengths to provide me with the tools and confidence to make it through 18 years of school.

Finally, I am incredibly thankful for my fiancée, Jessica, and her endless encouragement, support, and understanding during my studies. It has been a great privilege and pleasure to share this journey with her.

Nanoindentation Based Estimates of Flexoelectric Properties of Piezoelectric
Crystals

An Abstract

of a

Thesis

Presented to

the Faculty of the Interdisciplinary Program in Materials Engineering

University of Houston

In Partial Fulfillment

of the Requirements for the Degree

Master of Science

in Materials Engineering

by

Cody R. Robinson

May 2012

Abstract

Flexoelectricity refers to coupling between electric polarization and strain gradients in crystalline dielectrics. Recent work has shown that stiffness data obtained by nanoindentation, combined with an analytical indentation model that predicts size dependent behavior attributable to flexoelectricity, may be used to characterize flexoelectric properties of piezoelectric crystals. In the present work this experimental-analytical method is used and evaluated based on nanoindentation of quartz, LiNbO_3 , LiTaO_3 , $(0.7)\text{Pb}(\text{Mg}_{1/3}\text{Nb}_{2/3})\text{O}_3$ - $(0.3)\text{PbTiO}_3$, and BaTiO_3 with Berkovich, cone, and cube corner indenters. Flexoelectric properties appear negligible in quartz and are estimated to be on the order of $10^{-9} - 10^{-8} \text{ C/m}$ in LiNbO_3 and LiTaO_3 , and around 10^{-4} C/m for BaTiO_3 and PMN-30%PT. The results for quartz agree with previous work, the results for BaTiO_3 conflict, and those for the remaining materials are original and justifiable. Implications of the approach are discussed at length. The methodology in its current state is practical for specific types of dielectric crystals.

Table of Contents

Acknowledgements.....	iv
Abstract	vi
Table of Contents.....	vii
List of Figures.....	xi
List of Tables.....	xiv
Chapter 1 Introduction	1
1.1 Purpose and Organization.....	1
1.2 Motivation and Objectives.....	1
Chapter 2 Literature Review	5
2.1 Electromechanical Behavior in Crystalline Solids.....	5
2.1.1 Crystal Anisotropy, Symmetry, Notation.....	5
2.1.2 Electric Polarization Behavior in Crystals	7
2.1.3 Piezoelectricity	9
2.1.4 Flexoelectricity.....	11
2.2 Experimental Investigations of Flexoelectric Behavior.....	14
2.2.1 Flexure Experiments	14
2.2.2 Experiments Involving Non-Prismatic Bulk Samples	16

2.2.3 Nanoindentation Experiments	17
2.2.4 Summary of Flexoelectric Coefficients for Different Materials.....	18
2.3 Nanoindentation	19
2.3.1 Overview.....	19
2.3.2 Background and Standard Analysis of Nanoindentation Data	20
2.3.3 The Continuous Stiffness Measurement Technique	24
2.3.4 Nanoindenter Tips	27
2.3.5 Pile-up and Sink-in During Nanoindentation.....	32
2.3.6 Pop-In Phenomenon	33
2.4 The Indentation Size Effect	34
2.4.1 General Mechanisms of the Indentation Size Effect.....	35
2.4.2 Indentation Size Effects in Electromechanically Coupled Materials.....	39
2.5 Modeling of Electromechanical Materials during Indentation	43
2.5.1 Indentation of a Transversely Isotropic Piezoelectric Half Space.....	44
2.5.2 Incorporation of Flexoelectric Behavior into the Piezoelectric Model.....	51
2.5.3 Usage of the Model in Conjunction with Nanoindentation Data	57
2.6 Materials in this Study.....	63
2.6.1 Quartz (SiO ₂).....	63

2.6.2 Barium Titanate (BaTiO_3).....	64
2.6.3 Lithium Niobate (LiNbO_3) and Lithium Tantalate (LiTaO_3)	65
2.6.4 Lead Magnesium Niobate – Lead Titanate $(1-x)(\text{Pb}(\text{Mg}_{1/3}\text{Nb}_{2/3})\text{O}_3)-x(\text{PbTiO}_3)$	67
Chapter 3 Experimental Methods	69
3.1 Materials and Sample Preparation.....	69
3.2 Instruments	71
3.2.1 Nanoindentation System	71
3.2.2 Atomic Force Microscope.....	73
3.3 Procedures.....	73
Chapter 4 Experimental Results and Discussion	75
4.1 Quartz	75
4.2 Lithium Niobate (LiNbO_3).....	80
4.3 Lithium Tantalate (LiTaO_3)	91
4.4 Lead Magnesium Niobate – Lead Titanate (PMN-PT)	97
4.5 Barium Titanate (BaTiO_3)	103
Chapter 5 Summary and Conclusions	109
References	117
Appendix A – High Temperature Nanoindentation.....	131

Appendix B – Mounding (Pile-up) Effects	135
Appendix C – X-Ray Diffraction of SrTiO ₃	137

List of Figures

Figure 1. Polarization behavior of ferroelectric crystals	8
Figure 2. Piezoelectric behavior illustrated in a unit of a ZnO crystal.....	11
Figure 3. The concept of flexoelectric behavior in a centrosymmetric NaCl crystal.....	12
Figure 4. Bending test for determination of the transverse flexoelectric term f_{12}	15
Figure 5. Trapezoidal specimen of flexoelectric material used to determine f_{11}	16
Figure 6. Cross section of nanoindentation by an axisymmetric indenter.....	21
Figure 7. Load-displacement curve for a single nanoindentation test cycle.....	22
Figure 8. Oscillatory loading scheme for continuous stiffness measurements.....	25
Figure 9. Dynamic model of a nanoindentation system for CSM	25
Figure 10. Expanding cavity hardness model.....	28
Figure 11. Slip line hardness model.....	28
Figure 12. Geometry and relationships associated with Berkovich indenters	30
Figure 13. Effects of pile-up (mounding) and sink-in during nanoindentation	33
Figure 14. Appearance of a pop-in on a nanoindentation load-displacement curve	34
Figure 15. GND configuration in Nix and Gao's account of the indentation size effect	35
Figure 16. Lattice rotation maps of indentations in W and Cu crystals	39
Figure 17. Indentation of an elastic half space by a rigid flat punch	43

Figure 18. Indentation results for quartz and BaTiO ₃ compared with model predictions	59
Figure 19. The perovskite structure of BaTiO ₃ in its cubic and tetragonal phases	64
Figure 20. Trigonal structure of LiTaO ₃ and LiNbO ₃	65
Figure 21. Cylinder-in-sleeve sample holder for crystals requiring vibratory polishing	70
Figure 22. Schematic cross section of the Nano Indenter XP load-displacement head	71
Figure 23. Nano Indenter XP system specifications	72
Figure 24. Contact radius-displacement relationships for the three indenters.....	73
Figure 25. AFM micrographs for quartz indentations.....	76
Figure 26. Cross section view of a Berkovich indentation in quartz	77
Figure 27. Indentation results for quartz	78
Figure 28. AFM micrographs for LiNbO ₃ indentations	81
Figure 29. Cross section view of a Berkovich indentation in LiNbO ₃	82
Figure 30. Indentation results for LiNbO ₃	83
Figure 31. Indentation results for SrTiO ₃	90
Figure 32. AFM micrographs for LiTaO ₃	92
Figure 33. Cross section view of a Berkovich indentation in LiTaO ₃	92
Figure 34. Indentation results for LiTaO ₃	94
Figure 35. Demonstration of the influence of erroneous flexoelectric model parameters	97

Figure 36. AFM micrographs for PMN-30%PT.....	98
Figure 37. Cross section view of a Berkovich indentation in PMN-30%PT.....	99
Figure 38. Indentation results for PMN-30%PT.....	100
Figure 39. Results of deep Berkovich indentation tests for PMN-30%PT.....	103
Figure 40. AFM micrographs for BaTiO ₃	104
Figure 41. Cross section view of a Berkovich indentation in BaTiO ₃	104
Figure 42. Indentation results for BaTiO ₃	105
Figure 43. Comparison of deep Berkovich indentation results for quartz and BaTiO ₃	108
Figure 44. Nanoindentation at 120°C using the Nano Indenter XP and a custom heat stage.....	134
Figure 45. Raw X-ray diffraction data from test on SrTiO ₃ crystal.....	137

List of Tables

Table 1. Relationship between tensor and matrix notations	6
Table 2. Flexoelectric properties of various crystalline dielectrics.....	18
Table 3. Area and other relationships for indenters of various geometries	31
Table 4. Nomenclature for development of the piezoelectric indentation model	44
Table 5. Material properties for use with the flexoelectric indentation model	70
Table 6. Indenter area coefficients determined for the three indenters in this study	72
Table 7. Flexoelectric estimation results for LiNbO_3	88
Table 8. Flexoelectric estimation results for LiTaO_3	95
Table 9. Flexoelectric estimation results for PMN-30%PT.....	101
Table 10. Flexoelectric estimation results for BaTiO_3	107
Table 11. Influence of mounding on the determination of effective contact radius	136

Chapter 1 Introduction

1.1 Purpose and Organization

The flexoelectric effect refers to linear coupling between mechanical strain gradients and electric polarization or conversely polarization gradients and strain. Since the late 1990's, interest in flexoelectric effects in solid crystalline dielectrics has grown significantly, with notable research areas including size dependency [1-6], behavior of ferroelectric nanocapacitors [7,8], energy harvesting [3,9], and the development of piezoelectric composites using non-piezoelectric constituents [5,6,10-12]. The purpose of the present work is to use and evaluate a recently introduced nanoindentation-based method for estimating flexoelectric properties of piezoelectric crystals. This document is organized into five chapters. In this chapter the motivation and objectives of the research are discussed. A review of the literature pertaining to piezoelectricity, flexoelectricity, flexoelectric material characterization, nanoindentation, and analytical modeling of indentation of electromechanically coupled materials is provided in Chapter 2. Chapter 3 details the experimental methods in this study. Presentation and discussion of the experimental results are provided in Chapter 4. Chapter 5 encompasses the major conclusions of the present work and also addresses some topics that may be of interest in future investigations.

1.2 Motivation and Objectives

Smart materials of all different types have come into widespread use over the last century and particularly in the last few decades. By definition, smart materials are

materials that exhibit controllable or predetermined property changes as a response to changes in their environment. Examples of environmental stimuli include strain, temperature, electric fields, magnetic fields, and pH. In the case of electromechanical smart materials, electric field and mechanical characteristics are coupled. The most well known active electromechanical materials are piezoelectric ceramics, in which uniform mechanical strain gives rise to electric polarization. These materials have been tailored for applications ranging from cigarette lighters and buzzers to strain gauges and atomic force microscope components.

Despite their prevalence and notoriety, piezoelectric materials are in fact less abundant than flexoelectric materials. Piezoelectricity is only possible in crystals lacking a center of inversion symmetry. No such restriction exists for flexoelectric behavior. Swelling interest in the aforementioned flexoelectric research areas, especially the development of micro- and nanostructured flexoelectric composites, has greatly motivated attempts to characterize flexoelectric tensor components in both piezoelectric and non-piezoelectric materials. Flexoelectric properties have been estimated experimentally for materials including BaTiO_3 [2,13], SrTiO_3 [14], $(\text{Ba,Sr})\text{TiO}_3$ [15-17], lead magnesium niobate (PMN) [18], lead zirconate titanate (PZT) [19], and lead magnesium niobate-lead titanate (PMN-10%PT) [20].

Experiments to determine flexoelectric properties of solid crystalline dielectrics may be generally categorized by sample geometry and loading method, e.g., mechanical or electrical. Flexure type experiments (cantilever, three point, or four point bending) are prevalent and involve beam or plate shaped samples. Another common approach employs samples of varying cross sectional area (e.g., trapezoidal, conical) so that uniaxial

mechanical loading results in an inhomogeneous strain distribution. Converse effect experiments, where electric rather than mechanical loads are applied, more commonly involve the later sample geometry.

Recently, Gharbi et al. [1,2] have introduced a methodology for extracting flexoelectric properties of piezoelectric crystals using stiffness data obtained by nanoindentation in conjunction with an analytically derived stiffness-contact radius relationship. Flexoelectric property estimates obtained for barium titanate (BaTiO_3) using the experimental-analytical approach agree reasonably well with flexoelectric properties determined by bending experiments [2,13]. It has also been demonstrated that quartz, accepted as having negligible flexoelectric properties, exhibits no discernable flexoelectric behavior in nanoindentation data for contact radii as small as about 20nm [1]. These findings indicate that though indirect, nanoindentation may be used to produce viable estimates of flexoelectric properties.

The present work focuses on use of the nanoindentation based method as a tool for estimating flexoelectric properties of piezoelectric crystals. There are four primary goals. One is to produce estimates of flexoelectric properties for three new piezoelectric materials: lithium niobate (LiNbO_3), lithium tantalate (LiTaO_3), and lead magnesium niobate-30% (nominal) lead titanate (PMN-30%PT). Quartz and BaTiO_3 will serve as benchmark materials exhibiting apparently negligible and strong flexoelectric behavior, respectively. Second, it is desired to qualitatively compare nanoindentation data obtained with indenters of Berkovich, cone, and cube corner geometry. All of these geometries deviate from the circular flat punch assumed in the flexoelectric indentation model, but they each possess distinct advantages and disadvantages over the idealized punch as well

as one another. The third objective is to demonstrate that a two parameter fit of the analytical model to the experimental data does not unreasonably affect final results of the flexoelectric property estimates but greatly simplifies the estimation procedure. A single parameter fit was used in previous work [2]. Finally, based on the findings related to the three preceding objectives, some assessment of the practicality of the approach will be provided.

Chapter 2 Literature Review

2.1 Electromechanical Behavior in Crystalline Solids

2.1.1 Crystal Anisotropy, Symmetry, Notation

Physical properties of crystals that are not directionally dependent with respect to some reference frame are isotropic. For example, since mass and volume are measurable quantities that are the same regardless of crystallographic orientation, density is an isotropic crystal property [21]. Most physical properties of crystals are directionally dependent and thus anisotropic. No crystal can be anisotropic in all its properties [21].

Just as physical properties depend on direction within a crystal, they also depend on the symmetry elements within the crystal, i.e., the symmetry of a crystal is related to the symmetry of its physical properties [21]. There are four symmetry elements in crystals which, when considered in all possible combinations, define the 32 crystal classes [21]. These symmetry elements are [21]:

- a. Presence of a center of symmetry (inversion symmetry)
- b. Mirror plane
- c. Total rotation symmetry axes (1, 2, 3, 4, or 6)
- d. Total inversion symmetry axes (1, 2, 3, 4, or 6)

A crystal possess inversion symmetry if each point (x,y,z) of the crystal may be inconsequentially moved to point $(-x,-y,-z)$ with $(0,0,0)$ at the center of symmetry [21]. Crystals lacking inversion symmetry are non-centrosymmetric. Mirror plane refers to the presence of a crystal plane where points on each side of the plane are positioned such that

they are mirror images of each other [21]. Symmetry elements and inversion symmetry in particular dictate the type of electromechanical behavior a crystal may exhibit.

To account for the directional dependence of physical crystal properties, tensors are often employed. The tensor mathematically represents physical quantities such as electrical or thermal conductivity and relates them to a given set of axes. The rank, or order or degree, of a tensor indicates the number of subscripts or indices that associates each tensor component with the required number of specified axes. For example, Hooke's law relates stress and strain, represented by second-rank tensors, through the fourth-rank stiffness tensor. Using index notation (summation implied over repeated indices) we have

$$\sigma_{ij} = c_{ijkl} \varepsilon_{kl} \quad (i, j, k, l = 1, 2, 3), \quad \text{Eqn. 1}$$

where ε_{kl} are the strains associated with the set of axes k and l , σ_{ij} are the stresses associated with the set of axes i and j , and c_{ijkl} are the stiffness constants associated with the quartet of axes i, j, k , and l .

In addition to tensor notation, Voigt (matrix) notation may be used to represent anisotropic crystal properties. This notation results in more compact forms of equations since it reduces sets of subscripts into single subscripts as shown in Table 1.

Table 1. Relationship between tensor and matrix notations

Tensor notation	11	22	33	23, 32	31, 13	12, 21
Matrix notation	1	2	3	4	5	6

Reconsidering Hooke's law, we now have

$$\sigma_i = c_{ij} \varepsilon_j \quad (i, j = 1, 2, \dots, 6), \quad \text{Eqn. 2}$$

where the arrays σ_i , ε_j , and c_{ij} are matrices. Understand that c_{ij} are not tensor components and do not transform as tensor components. While the compliance and stiffness tensors are related by $s_{ijkl} = 1/c_{ijkl}$, the similar relation in matrix notation does not hold ($s_{ij} \neq 1/c_{ij}$) without the addition of some factors of 2 and 4 into the definitions relating s_{ij} and s_{ijkl} . The compactness of Voigt notation often justifies the extra attention to detail in dealing with material constants, but the tensor notation provides a better geometric understanding.

2.1.2 Electric Polarization Behavior in Crystals

Dielectric crystals are those which are electrically non-conductive and polarize in the presence of an applied electric field. Relative permittivity, or the relative dielectric constant K , defined as the ratio of stored charge in the dielectric once brought to a given voltage to that obtained between an identical set of electrodes separated by free space (a/a_0 , where $a_0 = 8.85 \times 10^{-12} \text{F/m}$), describes the degree of charge that may be stored in a dielectric material [22]. Values of relative permittivity are typically reported as measured under conditions of zero applied stress (free dielectric constant, K^T) or zero allowed strain (clamped dielectric constant K^S) [22]. The clamped and free dielectric constants may vary significantly in materials with large electromechanical coupling factors [22]. Dielectric susceptibility χ_{ij} , which essentially describes how easily charge accumulates in a dielectric material when exposed to an electric field, is related to dielectric permittivity through $a_{ij} = a_0 \delta_{ij} + \chi_{ij}$ where δ_{ij} is the Kronecker delta (1 for $i = j$, otherwise 0) [23].

Materials which are electrically non-conductive and polarize non-linearly in the presence of an applied electric field are typically called paraelectric. As with plain dielectrics, removal of the applied electric field results in a loss of charge. In contrast with simple dielectric and paraelectric materials, ferroelectric materials charge in the presence of an applied electric field but are able to remain spontaneously polarized when the field is removed. Application of a reverse field is required to return the polarization to zero, and further application of the reverse field will result in a reverse spontaneous polarization. This behavior results in the characteristic hysteresis loops associated with ferroelectrics and shown in Figure 1 [23].

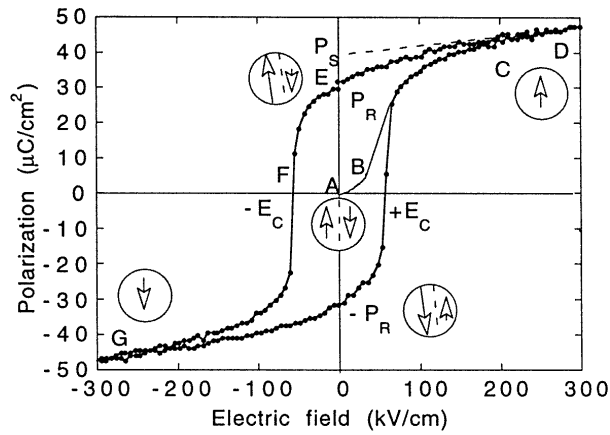


Figure 1. Polarization behavior of ferroelectric crystals

Ferroelectricity is only possible in crystals that allow for atomic arrangements of ions in a way such that positive and negative charge centers in the unit cell do not coincide. More specifically, ferroelectricity necessitates two or more distinct polarization states that may be switched between by application of an electric field [24]. For this reason, many polar crystals such as wurtzite-structure insulators are not ferroelectric [24]. Since many ferroelectrics undergo a structural phase transition to a paraelectric state of higher crystal symmetry as they are heated above their Curie temperature, it is often

convenient to think of ferroelectric structures as distortions of a higher symmetry “reference” phases [24].

Ferroelectric domains are regions of uniform spontaneous dipole orientation within a ferroelectric crystal that serve to minimize overall electrostatic and strain energy associated with the paraelectric to ferroelectric phase transformation [23]. Domains are separated by domain walls, which are typically categorized according to the orientation of the poles they separate (e.g., 180° domain walls separate areas of opposite polarization, 90° domain walls separate areas of orthogonal polarization, etc.) [23]. Applying an electric field to ferroelectric crystals can re-orient domains and may be used to achieve a single- or mono-domain crystal [23]. Application of an electric field to induce some type of polarization reversal is called poling. Ferroelectric ceramics may also be poled to reorient domains within the individual grains and achieve a net polarization [23].

2.1.3 Piezoelectricity

Jacques and Pierre Currie discovered piezoelectricity in 1880 while conducting experiments on quartz, zinblende, and tourmaline crystals [25]. They found that inducing a mechanical strain in certain types of crystals resulted in an electric polarization [26]. This is now commonly referred to as the direct piezoelectric effect. The Curie brothers also found that the same crystals responded to the application of electric polarization by deformation: the inverse piezoelectric effect [26]. In both the direct and inverse cases of piezoelectric behavior the degree of strain and electric polarization are proportional [26].

Absence of a center of symmetry in a crystal is an essential condition for a material to exhibit piezoelectric behavior because it allows for the relative separation of charge centers [25]. Consider, for example, the noncentrosymmetric cation-anion unit of hexagonal-wurtzite structured ZnO as illustrated in Figure 2 [6]. In the unstressed state, the oxygen anions at each corner of the tetrahedral unit produce a negative charge center that is coincident with the positive charge of the central zinc cation [6]. No polarization results. When the cell is subjected to a uniform strain, the negative charge center due to the oxygen anions becomes displaced with respect to the positive charge center associated with the zinc cation, resulting in an electric dipole within the cell [6]. Since these dipoles arise throughout the crystal a net polarization is observed [6]. The relative charge displacement between positive and negative charge centers under uniform strain is the mechanism of piezoelectricity. Since homogeneous stress is centrosymmetric, the only way an asymmetric response such as polarization may develop in a material is if the crystal structure itself lacks a center of symmetry [25].

Mathematically, the resultant polarization of a crystal exhibiting piezoelectric behavior is related to strain through the relation

$$P_i = p_{ijk} \epsilon_{jk} , \quad \text{Eqn. 3}$$

in which \mathbf{P} is the polarization vector, \mathbf{p} is the third rank piezoelectric tensor, and $\boldsymbol{\epsilon}$ is the second rank strain tensor. For crystals that possess a center of symmetry, tensor transformation properties make the odd rank tensor \mathbf{p} vanish [27]. Note that all ferroelectric crystals are piezoelectric due to symmetry requirements.

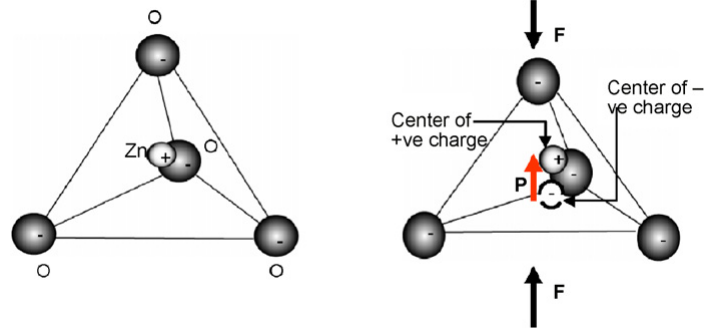


Figure 2. Piezoelectric behavior illustrated in a unit of a ZnO crystal

2.1.4 Flexoelectricity

Mashkevich and Tolpygo [28,29] appear to have been the first to predict that macroscopic strain gradients in solid crystalline dielectrics should give rise to a proportional degree of dielectric polarization [30]. In 1963 Kogan [31] addressed this issue in greater detail and provided a phenomenological description. When a crystal experiences inhomogeneous deformation, any resultant induced polarization should depend on both the deformation itself as well as the spatial derivatives of the deformation at any given point [31]. Formally this notion is represented in the equation

$$P_i = p_{ijk} \varepsilon_{jk} + f_{ijkl} \frac{\partial \varepsilon_{jk}}{\partial x_l}. \quad \text{Eqn. 4}$$

Here, f is a fourth order tensor that relates electric polarization to strain gradient. The phenomenon of strain gradient and electric polarization coupling is now generally referred to as the flexoelectric effect, and the components of f are referred to as the flexoelectric coefficients [6]. Unlike the components of the piezoelectric tensor, which may only be nonzero for crystals lacking a center of symmetry, the components of the flexoelectric tensor f are nonzero for many materials including those that are

centrosymmetric. Theoretically, all dielectric crystals are capable of deformation induced polarization under the right circumstances [6]. Since flexoelectricity is possible in centrosymmetric crystals, it is considered to be a more general material property than piezoelectricity.

Flexoelectric polarization in centrosymmetric crystals is possible because inhomogeneous strain breaks inversion symmetry. This process is illustrated in Figure 3 [6]. Section (a) shows a two dimensional unit cell of a NaCl crystal with a central Na cation and four Cl anions at each corner. In this configuration and under the conditions of uniform strain as shown in (b) the negative and positive charge centers of the anions and cations are coincident with one another and no net polarization results [6]. When the cell is subjected to a strain gradient as shown in (c), the noncentrosymmetric configuration of the displaced atoms causes the positive and negative charge centers to become displaced relative to each other resulting in a net polarization [6]. Flexural bending as illustrated in (d) and (e) induce inhomogeneous strains [6].

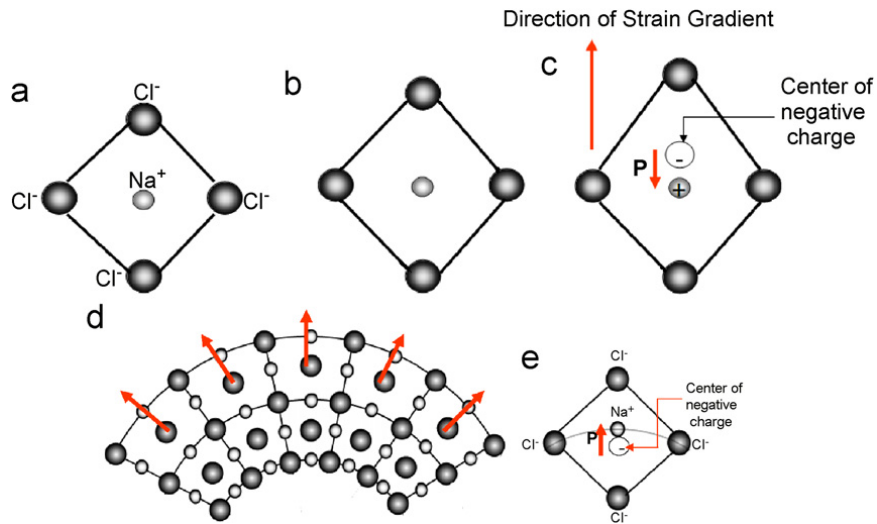


Figure 3. The concept of flexoelectric behavior in a centrosymmetric NaCl crystal

Until relatively recently, many years after the pioneering work of Mashkevich, Tolpygo, and Kogan, there were very few experimental studies on the flexoelectric effect in solid state crystalline materials. The reason for this void of academic investigation has been attributed to the fact that the flexoelectric coefficients for many materials are quite small compared to those associated with piezoelectricity [14]. Indeed, Kogan estimated that the flexoelectric tensor's magnitude should be on the order of e/a , where e is the absolute value of the charge of an electron and a is the lattice parameter [31]. This relation puts the magnitude of the flexoelectric tensor for many materials around 10^{-10} C/m [32]. In addition to the expected small magnitude of the flexoelectric coefficients, there are difficulties associated with the production of large strain gradients in bulk samples which contributed to a lack of research in flexoelectricity for many years [14].

Around 1991 A. K. Tagantsev expanded on the estimate of $f \approx e/a$ and introduced the idea that the flexoelectric coefficients for a given material are proportional to that material's dielectric susceptibility [12,33]. This relationship is commonly expressed as

$$f_{ijkl} = \gamma \chi_{ijkl} \frac{e}{a}, \quad \text{Eqn. 5}$$

where χ is the dielectric susceptibility and γ is a constant. Thus, high dielectric constant materials should exhibit proportionally higher degrees of polarization. Despite this development, there were still very few attempts to experimentally measure flexoelectric coefficients in any materials for the remainder of the decade. In 2000, motivated by the recently proposed prospect of piezoelectric flexoelectric composites, Cross and Ma [18] carried out experiments on the ferroelectric relaxor lead magnesium niobate (PMN) and measured a flexoelectric coefficient orders of magnitude higher than e/a . Subsequent

investigations by Cross and others involving a variety of materials have generally supported Tagantsev's relationship but indicate that dielectric susceptibility alone cannot account for the large and nonlinearly varying flexoelectric coefficients observed in many ferroelectric crystals [15,16,34]. Many of these studies show that the value of the scaling factor γ is not only material dependent but also varies with several factors including dielectric permittivity and strain gradient magnitude [34].

2.2 Experimental Investigations of Flexoelectric Behavior

2.2.1 Flexure Experiments

Most of the early successful attempts at measuring flexoelectric tensor components involved subjecting thin beam specimens to dynamic bending while measuring current produced at the upper and lower beam surfaces. Ma and Cross [18] appear to have been the first to utilize this setup, using a loudspeaker to drive thin cantilever beam samples while simultaneously measuring displacements with a differential variable reluctance transducer (DVRT) and current generated by the sample with a lock-in amplifier. In addition to cantilever beams, Ma and Cross [19] have tested thin beams in quasi static four point bending to generate uniform strain gradients. Zubko et al. [14] successfully carried out flexoelectric measurements by subjecting beams to oscillatory three point bending with a dynamic mechanical analyzer (DMA) and again measuring current due to induced polarization with a lock-in amplifier. This configuration is illustrated in Figure 4 [14]. Also noted in Figure 4, it is typical in flexure type tests to use sputtered gold as electrodes on the upper and lower surfaces of the beam samples.

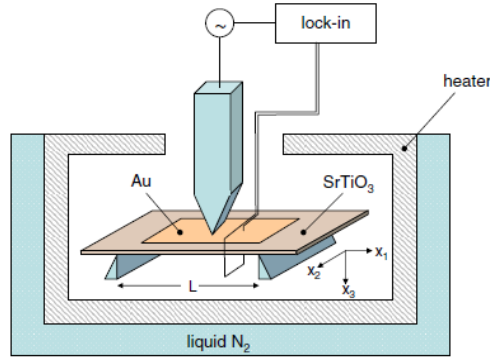


Figure 4. Bending test for determination of the transverse flexoelectric term f_{12}

The primary benefit of flexure testing is that it is a relatively straightforward matter to directly measure all the parameters required to calculate the transverse flexoelectric tensor component f_{1122} , or f_{12} in matrix notation. Following the orientation of x_1, x_2, x_3 in Figure 3, polarization P_3 in the directions normal to the upper and lower beam surfaces is given by [14]

$$P_3 = f_{12} \frac{\partial \varepsilon_{11}}{\partial x_3}. \quad \text{Eqn. 6}$$

Polarization P_3 is found from the electrode measurements and the strain gradient term from sample curvature so f_{12} may be determined [16]. Another benefit of flexure testing is that the presence of a neutral axis at the beam center precludes the effects of residual piezoelectricity that may bias measurements in some materials [16]. Finally, it is relatively easy to setup flexure tests for a variety of sample sizes (from a few millimeters [18] to about $50\mu\text{m}$ [14]) and temperature ranges. As noted in Figure 3 heaters and liquid nitrogen cooling have been used to control testing temperature in flexure investigations.

2.2.2 Experiments Involving Non-Prismatic Bulk Samples

While flexure tests have proven useful for determining the transverse flexoelectric coefficient f_{12} , different methods are needed to determine the longitudinal coefficient f_{1111} (matrix notation f_{11}). Generating longitudinal strain or electric field gradients in axially loaded bulk material is possible by designing samples with non-prismatic geometries such as the truncated pyramid-shaped specimen in Figure 5 [16]. Both direct flexoelectric effect and converse effect approaches have been utilized. Cross [16] has evaluated f_{11} in truncated pyramid-shaped samples by generating cyclic longitudinal stress with an Instron test frame while simultaneously measuring charge release with a lock-in amplifier linked to the Instron driver. Fu et al. [17] have alternatively evaluated f_{11} in samples of trapezoidal geometry by polarizing them in the longitudinal direction and measuring the resultant displacement. In both cases the sample's chosen boundary shape allows for the investigation of flexoelectric phenomenon in the longitudinal axis. A major advantage of these types of tests is that they may easily be conducted in environmental cells so temperature and other environmental factors may be readily controlled.



Figure 5. Trapezoidal specimen of flexoelectric material used to determine f_{11}

2.2.3 Nanoindentation Experiments

The concept of using data obtained during nanoindentation tests to characterize flexoelectric material behavior was introduced by Gharbi et al. [1,2] This work involved the development of an analytical model of the indentation of a transversely isotropic surface that incorporates piezoelectricity and flexoelectricity which can be used in conjunction with indenter contact radius and dynamically measured stiffness data to estimate flexoelectric tensor components. Many commercial nanoindentation systems are capable of continuously measuring material stiffness as a function of indenter displacement into the specimen surface. This is achieved by loading the sample quasi-statically at a constant strain rate to some specified load or depth while simultaneously superimposing a relatively small sinusoidal force and analyzing the dynamic response of the system. Contact radius is known as a function of indenter depth that has been determined through standard calibration methods. Gharbi et al. [2] has estimated f_{12} for BaTiO₃ in good agreement with the results of flexure tests conducted by other groups.

One advantage of being able to use nanoindentation data to estimate flexoelectric coefficients is that obtaining the required data (load, displacement, and dynamic stiffness) is often straightforward using commercial indentation systems in air at room temperature. The other major advantage of nanoindentation testing is that since only a very small volume of material is needed for testing, samples are relatively easy to manufacture and prepare in comparison to the aforementioned truncated pyramid-shaped samples or beams for flexure testing. Unfortunately, nanoindentation testing, and hence flexoelectric property estimation by nanoindentation, is generally limited to temperatures close to ambient for reasons discussed in Appendix A.

2.2.4 Summary of Flexoelectric Coefficients for Different Materials

Only a few materials have been evaluated for their flexoelectric properties. Early studies in flexoelectric ceramics focused on lead magnesium niobate ($\text{Pb}(\text{Mg}_{1/3}\text{Nb}_{2/3})\text{O}_3$), barium strontium titanate ($(\text{Ba}_{2/3}\text{Sr}_{1/3})\text{TiO}_3$) and other ferroelectrics. Many of these studies were conducted by L. E. Cross and others at Pennsylvania State University. Table 2 provides a summary of some materials that have had one or more of their flexoelectric coefficients determined experimentally.

Table 2. Flexoelectric properties of various crystalline dielectrics

Material	f_{11} ($\mu\text{C}/\text{m}$)	f_{12} ($\mu\text{C}/\text{m}$)	Method	Temp.	Reference
BaTiO ₃		10	Cantilever flexure	RT	13
		50		120C	
		4	Nanoindentation	RT	2
SrTiO ₃	0.009	0.004	3-point bending	RT	14
Ba _{0.67} Sr _{0.33} TiO ₃		100	Cantilever flexure	23C	15
	115			25C	16
	121±20		Converse effect, trapezoid blocks	25C	17
Pb(Mg _{0.33} Nb _{0.67})O ₃		4	Cantilever flexure	RT	18
PZT-5H		1.6	4-point bending	20C	19
PMNT10	6-12		Cone ceramic blocks	RT	20

2.3 Nanoindentation

2.3.1 Overview

Nanoindentation is a form of instrumented indentation testing (that is, indenter load and displacement are continuously recorded) which works on principles similar to those in all indentation testing. An indenter of known geometry and material properties is pressed with a specified load into a sample of unknown properties. Based on the behavior of the sample resulting from the indentation procedure, such as residual indentation size, material properties of the sample may be determined. Brinell, Vickers, and Rockwell hardness tests, for example, all operate on this principle. Nanoindentation is distinct from these types of indentation tests primarily in two ways [35]. First, the length scale involved in indenter displacement during nanoindentation testing is (as the name suggests) nanometers (10^{-9} m) as opposed to microns (10^{-6} m) or millimeters (10^{-3} m). Displacement and load resolutions of <0.01 nm and <50 nN, respectively, are typical of commercial nanoindentation systems. Second, the size of a residual nanoindentation impression need not be measured by direct observation for accurate determination of a sample material's properties. Instead, the area of contact at the indenter-sample interface is inferred from the depth of indenter penetration into the sample since for an indenter of known geometry the cross sectional area at any point along the loading axis is a function of distance from the tip. The term "depth sensing indentation" has been applied to nanoindentation due to its reliance on an indenter depth-area function rather than direct observation for the determination of contact area of the residual indentation [35]. Nanoindentation procedures exist today for the determination of a variety of material

properties including hardness, elastic modulus, fracture toughness, viscoelastic properties, and strain hardening exponents [35].

2.3.2 Background and Standard Analysis of Nanoindentation Data

The origins of indentation analysis inevitably trace back to early works by Joseph V. Boussinesq and Heinrich R. Hertz concerning fundamental issues in elastic contact theory. Hertz studied elastic contact between spheres of different radii and elastic moduli, and Boussinesq used potential theory to develop relations for stress and displacements arising from elastic contact between a body and a rigid axisymmetric indenter [36]. Sneddon [37] later considered the Boussinesq axisymmetric punch problem and was able to show that indentation load and depth for any indenter that is a smooth solid of revolution may be related through

$$P = \alpha h^m, \quad \text{Eqn. 7}$$

where P is the load on the indenter, h is the depth of the elastic indentation, α is a constant dependent on the half space properties and indenter geometry, and m is a constant that depends only on indenter geometry (e.g. $m=1$ for cylindrical indenters and $m=2$ for conical indenters) [36]. This power law relationship became a central point in the development of Oliver and Pharr's [36] method of analysis of nanoindentation data, which has remained a widely used and accepted basic approach for nearly 20 years. Oliver and Pharr's technique is based largely on the earlier work of Doerner and Nix [38], who used the initial, linear portion of indentation load versus displacement curves during unloading to estimate material properties. Oliver and Pharr perceived inadequacies

in Doerner and Nix's approach and successfully developed a method in which a power law of the type above is used to describe unloading curves.

Following initial indenter-surface contact at the beginning of a nanoindentation test, material under the indenter is first displaced elastically then elastically and plastically as the indenter is driven into the sample surface. Figure 6 [36] depicts a schematic cross section through a material loaded by an axisymmetric indenter. The applied load is given by P , a is the radius of the contact circle, h is the total displacement, h_c is the contact depth, h_s is the displacement of the surface at the perimeter of the contact, and h_f is the final or residual depth of indentation after the load is removed. The total displacement of the tip with respect to the surface is $h = h_c + h_s$. Figure 7 [36] depicts a load-displacement curve during a single loading and unloading indentation test cycle.

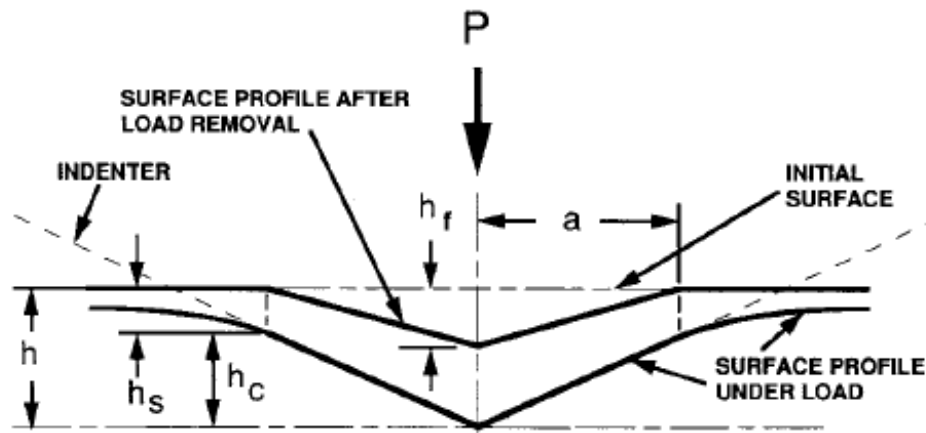


Figure 6. Cross section of nanoindentation by an axisymmetric indenter

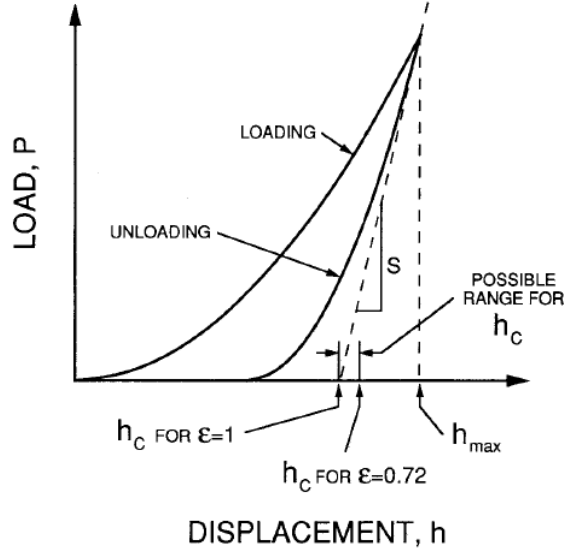


Figure 7. Load-displacement curve for a single nanoindentation test cycle

Analysis of the indentation data begins with defining S , the stiffness of the upper portion of the unloading data as

$$S = \frac{dP}{dh} = \frac{2}{\sqrt{\pi}} E_r \sqrt{A}. \quad \text{Eqn. 8}$$

Here, A is the projected area of elastic contact and E_r is the reduced or combined modulus. The projected contact area A is calculated from an area-depth function,

$$A = f(h_c), \quad \text{Eqn. 9}$$

that has been specifically calibrated to a given tip. The reduced modulus is defined by

$$\frac{1}{E_r} = \frac{(1-\nu^2)}{E} + \frac{(1-\nu_i^2)}{E_i}, \quad \text{Eqn. 10}$$

where E and ν refer to Young's modulus and Poisson's ratio of the sample and E_i and ν_i refer to Young's modulus and Poisson's ratio of the indenter, respectively. It is generally

accepted that Eqn. 8 holds for any indenter that may be described as a body of revolution of a smooth function, and that only minor deviation is encountered when applied to pyramidal indenters [36]. Hardness of the sample is defined as

$$H = \frac{P_{\max}}{A}, \quad \text{Eqn. 11}$$

where P_{\max} refers to the maximum applied load. In Eqns. 8 through 11 all parameters except for h_c are either known beforehand or directly measured during indentation. Once a value for h_c is determined, material properties E and H may be calculated.

Oliver and Pharr [36] describe the unloading data for stiffness measurement with

$$P = B(h - h_f)^m, \quad \text{Eqn. 12}$$

where B , m , and h_f , all of which are constants, are determined by least squares fitting to the measured indentation data. From the definition of contact stiffness, evaluation of the derivative of this expression at peak load and displacement yields stiffness (slope of the load-displacement curve) at the onset of unloading

$$S = \left(\frac{dP}{dh} \right)_{h=h_{\max}} = Bm(h_{\max} - h_f)^{m-1}. \quad \text{Eqn. 13}$$

This stiffness value, along with the maximum load value and a geometric (indenter-dependent) constant, ε , allow for the determination of the displacement of the surface at the perimeter of the contact

$$h_s = \varepsilon \frac{P_{\max}}{S}. \quad \text{Eqn. 14}$$

Since $h = h_c + h_s$,

$$h_c = h_{\max} - \varepsilon \frac{P_{\max}}{S}, \quad \text{Eqn. 15}$$

and the desired properties of the sample may be calculated.

2.3.3 The Continuous Stiffness Measurement Technique

Analyzing the initial segment of the unloading curve of nanoindentation data only allows for determination of mechanical sample properties at discrete load-depth combinations. The continuous stiffness measurement (CSM) technique, developed by Pethica and Oliver [39,40], builds on the principles of the preceding analysis, but allows for mechanical properties to be determined continuously as the indenter is driven into the material surface. Rather than simply applying a continuously and monotonically increasing load to the sample, CSM involves an oscillatory loading scheme which may be considered as the superposition of a sinusoidal load pattern of specified frequency and amplitude with a primary loading pattern as described before. This type of loading, depicted schematically in Figure 8 [41], allows for continuous measurement of contact stiffness, S , by a dynamic analysis of the indentation system.

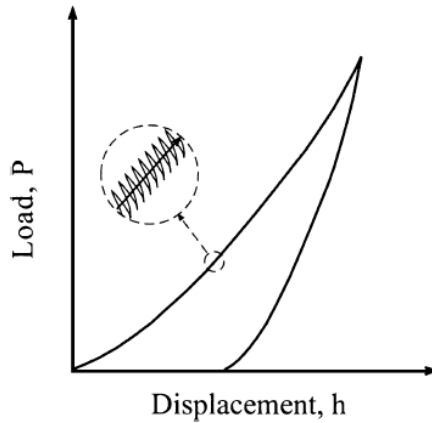


Figure 8. Oscillatory loading scheme for continuous stiffness measurements

The dynamic model of the indentation system consists of five components: a mass element representing the indenter column, three spring elements, and one damping element. The three spring elements represent the springs supporting the indenter column (K_s), the test frame stiffness ($K_f = 1/C_f$, where C_f is frame compliance), and contact stiffness S . The damping element C represents viscous damping due to air present between the plates of the capacitive load cell. This dynamic model is schematically depicted in Figure 9 [41].

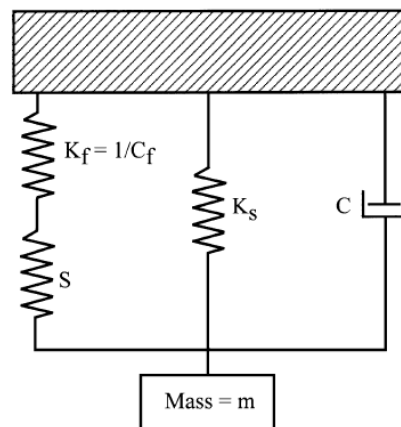


Figure 9. Dynamic model of a nanoindentation system for CSM

Following Li and Bhushan's [41] summary, CSM involves a driving force,

$$P = P_{os} \exp(i\omega t), \quad \text{Eqn. 16}$$

where P_{os} is the magnitude of the load oscillation, ω is the oscillation frequency, and t is time. The displacement response of the indenter is then given by

$$h(\omega) = h_0 \exp(i\omega t + \phi), \quad \text{Eqn. 17}$$

where ϕ is the phase angle between the load and displacement. Based on these signals and the known system model parameters, the contact stiffness during indentation may be determined either from amplitude of the displacement through

$$\left| \frac{P_{os}}{h(\omega)} \right| = \sqrt{\{(S^{-1} + C_f)^{-1} + K_s - m\omega^2\}^2 + \omega^2 C^2}, \quad \text{Eqn. 18}$$

or from the phase difference between applied load and displacement through

$$\tan(\phi) = \frac{\omega C}{(S^{-1} + C_f)^{-1} + K_s - m\omega^2}. \quad \text{Eqn. 19}$$

For very stiff materials, contact stiffness determined from the amplitude measurement tends to be more accurate because the phase angle ϕ becomes very small relative noise in the signal [36].

The CSM technique has proven useful in a wide variety of applications including hardness and modulus determination, creep resistance evaluation, characterization of viscoelastic properties of polymers, and fatigue testing [41].

2.3.4 Nanoindenter Tips

Nanoindenter tips are generally made of diamond ($E \approx 1000 \text{ GPa}$ $\nu = 0.07$ [35]) due to its exceptional hardness and stiffness, but other indenter materials are available for various applications. Tip geometries mostly fall into two basic categories: sharp (e.g., cube corner) or blunt (e.g., spherical). The degree of sharpness or bluntness of the indenter can greatly affect the sample material's response and may be explained in terms of the "expanding cavity" and "slip line" theories of hardness. The expanding cavity model, depicted schematically in Figure 10 [35], emphasizes that plastic deformation under the indenter is due to primarily compressive stresses and that the displaced volume of material during indentation is accommodated almost exclusively by elastic strains outside of the plastic zone [35]. A hydrostatic core region of radius a_c exists just below the indenter out to the edge of contact, and is surrounded by a hemispherical plastic zone of radius c [35]. Blunt indenter geometries tend to favor the expanding cavity model. Sharp indenters, however, make elastic constraint of the plastic zone difficult, and it is common for the displaced volume of plastically deformed material to flow upward around the indenter [35]. This behavior, which involves a distinct "cutting" type of mechanism, is described by slip line theory, illustrated schematically in Figure 11 [35]. For frictionless contact in an isotropic material, stresses at the indenter-sample interface are normal to the interface and the lines of maximum shear stress, or slip lines, are oriented at 45° to the indenter (lines in region ABE in the figure are 45° to line AB) [35]. It is important to recognize the differences in anticipated plastic zone behavior between the two hardness models both when selecting an indenter geometry and in comparing data for the same material obtained with indenters of significantly different geometry.

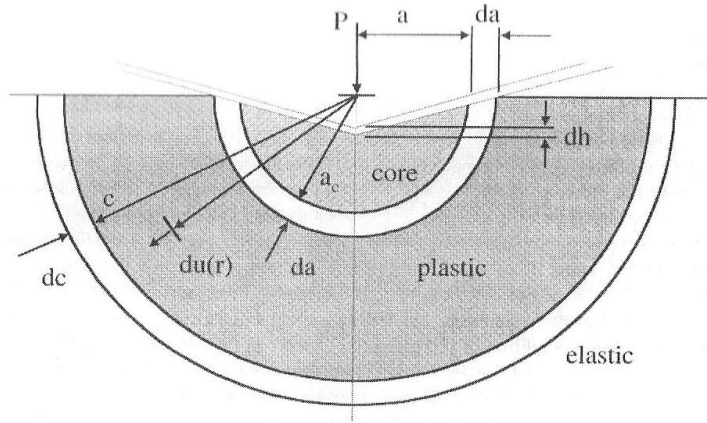


Figure 10. Expanding cavity hardness model

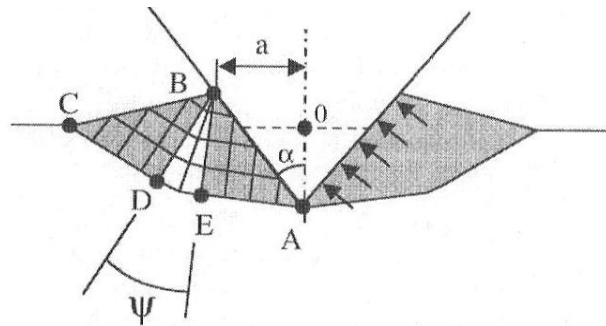


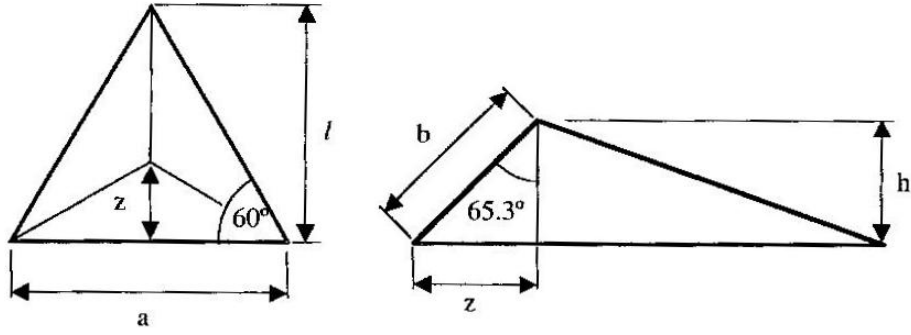
Figure 11. Slip line hardness model

Berkovich, cube corner, and cone indenters are used in this thesis. Berkovich indenters are characterized by their three sided pyramidal geometry which yields the same projected area to depth ratio as a Vickers indenter but allows for greater simplicity in the manufacturing process since three facets preclude the possibility for development of a chisel edge at the tip [35]. Berkovich indenters used in nanoindentation testing have a nominal face angle of 65.3° and are relatively sharp with a tip radius of about 50-100nm [35]. Figure 12 [35] schematically illustrates the geometry of a Berkovich indenter and provides the relationships for projected area and surface area as a function of depth. Berkovich indenters are the most popular type of indenter for nanoindentation testing because they are relatively easy to manufacture and maintain. Additionally, they are

sharp enough for applications requiring very shallow indentations, such as characterization of thin films, but are significantly less fragile than other tips capable of inducing nearly constant plastic strain during impression [42].

Cube corner indenters are also three sided indenters, but with face angles of 35.26° [35], they are much sharper than Berkovich indenters. As the name implies, this geometry is a result of the interception of three mutually orthogonal planes. While Berkovich and Vickers indenters produce very strongly compressive stresses under the tip and approximate the expanding cavity model, cube corner indenters tend to cut into the sample and are more likely described by slip line theory [35]. Cube corner indenters are very effective for inducing cracking during indentation, such as when fracture toughness measurements are to be made.

Unlike the pyramidal Berkovich and cube corner indenters, conical indenters are axisymmetric, that is, their projected contact area is actually in the shape of a circle. A true contact radius may be determined for a given indentation depth with these indenters, and there is an advantage in the absence of plane edges intersecting the contact perimeter which cause stress concentrations [43]. Despite these advantages, as well as a strong connection with many analytical indentation models, conical indenters are not frequently used in nanoindentation studies because they are quite difficult to manufacture and maintain with sharp tips [43]. The included angle may vary quite a bit, but conical indenters are sharp relative to spherical indenters.



Projected area

$$\begin{aligned} \tan 60 &= \frac{l}{a/2} \\ l &= \frac{\sqrt{3}}{2}a \\ A_{\text{proj}} &= \frac{al}{2} \\ &= \frac{\sqrt{3}}{4}a^2 \quad 0.433a^2 \\ \cos 65.27 &= \frac{h}{b} \\ h &= \frac{a \cos 65.3}{2\sqrt{3} \sin 65.3} \\ &= \frac{a}{2\sqrt{3} \tan 65.3} \\ a &= 2\sqrt{3}h \tan 65.3 \\ A_{\text{proj}} &= 3\sqrt{3}h^2 \tan^2 65.3 \\ &= 24.56h^2 \end{aligned}$$

Surface area

$$\begin{aligned} A_{\text{surf}} &= 3\frac{ab}{2} \\ \sin 65.3 &= \frac{z}{b} \\ z &= \frac{a}{2} \tan 30 \\ &= \frac{a}{2\sqrt{3}} \\ b &= \frac{a}{2\sqrt{3} \sin 65.3} \\ A_{\text{surf}} &= 3\frac{a^2}{4\sqrt{3} \sin 65.3} \\ &= 0.477a^2 \\ a &= 2\sqrt{3}h \tan 65.3 \\ A_{\text{surf}} &= 27.05h^2 \end{aligned}$$

Equivalent
cone angle:
70.32°

Figure 12. Geometry and relationships associated with Berkovich indenters

As a matter of convenience, indentation tests conducted with pyramidal indenters are often treated as though they were conducted with a conical indenter defined by an effective conical semi-angle α [35]. Table 3 [35] summarizes the projected area relations, semi angles, effective cone angles, and other factors for various indenter geometries.

Table 3. Area and other relationships for indenters of various geometries

Indenter type	Projected area	Semi-angle θ (deg)	Effective cone angle α (deg)	Intercept factor	Geometry correction factor β
Sphere	$A \approx \pi 2Rh_p$	N/A	N/A	0.75	1
Berkovich	$A = 3\sqrt{3}h_p^2 \tan^2 \theta$	65.3°	70.2996°	0.75	1.034
Vickers	$A = 4h_p^2 \tan^2 \theta$	68°	70.32°	0.75	1.012
Knoop	$A = 2h_p^2 \tan \theta_1 \tan \theta_2$	$\theta_1 = 86.25^\circ$, $\theta_2 = 65^\circ$	77.64°	0.75	1.012
Cube Corner	$A = 3\sqrt{3}h_p^2 \tan^2 \theta$	35.26°	42.28°	0.75	1.034
Cone	$A = \pi h_p^2 \tan^2 \alpha$	α	α	0.72	1

The projected area relations in Table 3 are only directly applicable for ideal indenters. Real indenters have imperfect geometry that must be accounted for to minimize errors during subsequent calculation of material properties. Typically, data for the projected area of an actual indenter is fit as a function of contact depth to a polynomial of sufficiently high order so that best fit coefficients may be determined. The general indenter area function then takes the form

$$A = C_1 h_c^2 + C_2 h_c + C_3 h_c^{1/2} + C_4 h_c^{1/4} + C_5 h_c^{1/8}, \quad \text{Eqn. 20}$$

where C_i ($i=1, 2, \dots, 5$) are the fit parameters and h_c is the distance from the tip of the indenter along the loading axis. The leading term best describes the behavior of an ideal indenter, while the remaining terms account for geometric imperfections. Data at low indentation depths is often weighted in the fitting procedure to yield more accurate fitting at the indenter tip where rounding effects are important.

No matter the indenter geometry, tip cleanliness is essential for obtaining quality nanoindentation data. Common practice to maintain diamond indenter tips includes performing deep indentations in samples of dense polystyrene [35] or soft aluminum.

2.3.5 Pile-up and Sink-in During Nanoindentation

During plastic deformation in a nanoindentation test, sample material can sink-in or pile-up around the indenter as it drives into the surface. The term mounding is sometimes used instead of pile-up so as to avoid any potential confusion with dislocation pile-up. Both of these situations are depicted schematically in Figure 13 [35]. Pile up seems to occur most strongly in non-strain hardening materials with a high ratio of elastic modulus to flow stress, E/Y [35]. Sink in appears more likely in strain hardening materials or even non-strain hardening materials with low E/Y ratios where elastic deformation can accommodate the small plastic zone [35]. Pile-up and sink-in affect nanoindentation data by causing inaccuracies in the indenter area-depth function. As illustrated in Figure 13, pile-up leads to an underestimation in actual contact area and sink-in results in over-estimation of the actual contact area. Standard nanoindentation analysis, such as that described above, does not take pile-up and sink-in effects into account. Despite a great deal of effort over the years, issues regarding the treatment of indentation data involving pile-up or sink-in still appear unresolved. A.C. Fischer-Cripps [44] notes that barring tedious direct measurements of the contact area following the indentation procedure,

There are two ways to approach the problem: (i) perform an area function calibration on a reference specimen which has a similar ratio of E/H as the test specimen (such that piling-up is accommodated within the area function correction) or (ii) ignore the effect and treat the resulting values of E and H as comparative values.

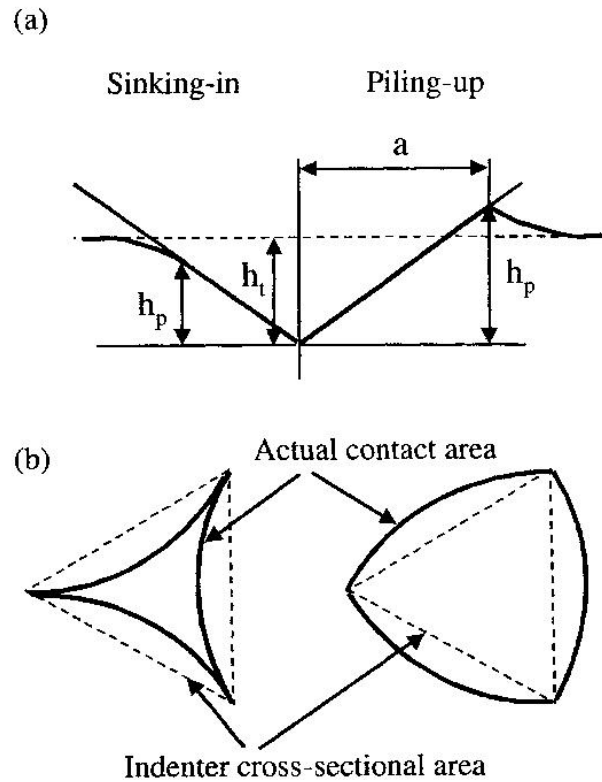


Figure 13. Effects of pile-up (mounding) and sink-in during nanoindentation

2.3.6 Pop-In Phenomenon

Brief displacement excursions accompanied by essentially no change in applied load encountered in nanoindentation testing are usually referred to as pop-ins. A pop-in event is shown schematically in Figure 14 [35]. Pop-ins have been observed in a variety

of crystalline materials including metals, ceramics, and semiconductors, and are most generally associated the onset of plasticity. Mechanisms explaining the pop-in phenomenon can vary with material and sample preparation technique but include homogeneous dislocation nucleation, dislocation source activation, fracture of a surface film, and interactions between surface films and underlying dislocation structures [45]. Initial loading prior to pop-in events has often been shown to be purely elastic, with no residual indentation impression or hysteresis in the load vs. displacement plots unloading [45-47]. In carefully prepared samples where dislocation density is minimized, stresses under the indenter just before the occurrence of a pop-in can approach the theoretical shear stress [46,47], hence the arguments for homogeneous dislocation nucleation. Pop-ins may also be observed in non-elastic loading regimes [45].

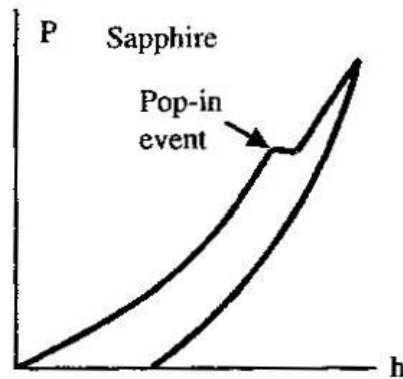


Figure 14. Appearance of a pop-in on a nanoindentation load-displacement curve

2.4 The Indentation Size Effect

Indentation size effect (ISE) refers to size dependency of a material property during an indentation test. Most often the term is associated with hardness values that decrease as indentation depth or contact radius increases. Early notable investigations

concerning the indentation size effect mostly dealt with metals and include works by Stelmashenko et al. [48], De Guzman et al. [49], Ma and Clarke [50], and Poole et al. [51]. Sometimes size dependency is due to something other than a true material response. Such factors may include oxide films, friction between the indenter and sample material, residual stresses at the sample surface arising from polishing procedures, and inaccuracies in the indenter-area function [35]. Despite the potential for such artifacts, the ISE is indeed a true and observable material response and has been observed in a variety of relatively simple materials as well as electromechanically coupled crystals.

2.4.1 General Mechanisms of the Indentation Size Effect

Nix and Gao [52] developed perhaps the most famous foundational model accounting for the indentation size effect using the concept of geometrically necessary dislocations (GNDs). As seen in Figure 15 [52] they worked under the assumption that plasticity during indentation by a conical indenter is accommodated by circular GND loops with Burgers vectors normal to the plane of the surface. All of the GND are contained within a hemispherical volume defined by the contact radius of the indenter.

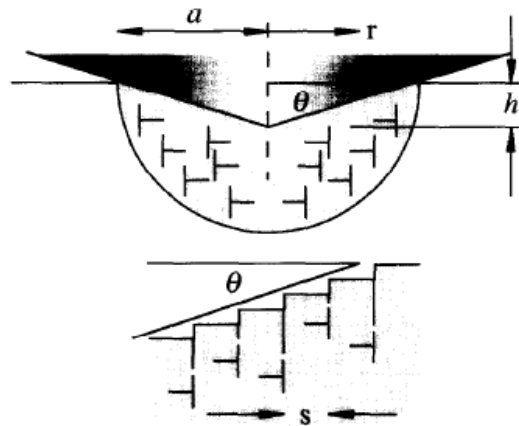


Figure 15. GND configuration in Nix and Gao's account of the indentation size effect

Based on these assumptions Nix and Gao [52] developed the following relationship for hardness and indentation depth:

$$\frac{H}{H_0} = \sqrt{1 + \frac{h^*}{h}} . \quad \text{Eqn. 21}$$

In this equation, the hardness that would arise due to statistically stored (pre-existing) dislocations in the material with no GND present is given by

$$H_0 = 3\sqrt{3}\alpha\mu b\sqrt{\rho_s} . \quad \text{Eqn. 22}$$

The term α is a constant, μ is the shear modulus, b is the burgers vector, and ρ_s is the density of statistically stored dislocations (SSDs). The density of SSDs and GNDs are assumed to be related through Taylor's hardening law,

$$\tau = \alpha\mu b\sqrt{\rho_s + \rho_g} , \quad \text{Eqn. 23}$$

in which τ is shear stress and ρ_g is the density of GNDs. The length parameter,

$$h^* = \frac{81}{2} b\alpha^2 \tan^2 \theta \left(\frac{\mu}{H_0} \right)^2 , \quad \text{Eqn. 24}$$

characterizes the depth dependence of hardness, where θ is the angle between the surface of the indenter and the surface of the sample material.

As the indentation depth h becomes significantly greater than h^* , the quantity under the radical tends to unity and the ratio of measured hardness to H_0 tend to unity as well, i.e., there is no size dependency in the hardness. For small indentation depths and/or relatively high values of h^* , the ratio of measured hardness to H_0 is greater than unity,

representing the indentation size effect. Nix and Gao [52] were able to demonstrate excellent agreement between their model and results from actual nanoindentation hardness tests conducted on single crystal copper and silver as well as polycrystalline cold worked copper. Note that the model suggests the indentation size effect should become smaller for materials of relatively high intrinsic hardness [52]. For increasingly large values of H_0 , h^* becomes smaller and H/H_0 is more likely to tend towards unity. Nix and Gao confirmed the model prediction by testing fused quartz, which exhibits no size dependency for indentation depths between 200nm and 600nm with Berkovich indenters and is more than ten times harder (about 9GPa) than copper or silver [52].

Swadener et al. [53] developed a correlation between the Nix and Gao model for conical indenters and the indentation size effect observed during indentation with spherical indenters. They determined that size dependent behavior with spherical indenters depends on the radius of the sphere rather than simply indentation depth, and they confirmed most of their analytical work with indentation results from tests performed on copper samples. They also noted that model predictions deviate (by overestimation) significantly from experimental results for very small contact radii and indentation depths when using spherical and pyramidal indenters, respectively. This deviation was presumed to be due to inaccurate estimation of the volume of material containing GNDs at the smaller length scales.

Subsequent research [47,54-58] has shown that while the models of Nix and Gao [52] as well Swadener et al. [53] are adequate for describing ISE at moderately small length scales, overestimation of hardness is an issue in the truly nano-scale regime. There have been many attempts (summarized nicely by [55] and [59]) to modify the

aforementioned models to enhance their accuracy with varying degrees of success. Such attempts have included compensating for friction [60], tip rounding [61], non-uniform distribution of GNDs [62], and underestimation of the volume of the plastic zone [47]. Abu Al-Rub and Voyiadjis [56] have suggested that the linear coupling between GNDs and SSDs assumed in Taylor's hardening law, utilized by Nix and Gao, is the major source of discrepancy between predictions and experimental results in the small scale. By coupling GNDs and SSDs in a nonlinear fashion, they were able to more accurately predict material behavior over a wider range of scale lengths.

Pharr et al. [59] draw attention to recent experimental and theoretical studies that highlight the need for a better understanding of how dislocation structures and processes vary with indentation size. Some studies that have focused on evaluating dislocation structure development during indentation through X-ray diffraction [63], electron backscattered diffraction [64], and scanning transmission electron microscopy [65]. Other groups [66,67] have investigated dislocation dynamics in nanoindentation by simulation in order to investigate the ISE. Results from these studies generally agree and indicate that GNDs do not develop homogeneously within a hemispherical volume under the indenter, as assumed by Nix and Gao [52], to any significant degree. Figure 16 [59] shows the manner in which lattice rotations develop during indentation experiments on (110) tungsten and (111) copper single crystals. These maps enable the deduction of local GND structures; the presence of distinct regions of lattice rotation suggests a highly non-uniform dislocation distribution under the indenter [59]. Similar lattice rotation maps indicate that dislocation structures do not grow self similarly as indentation proceeds, even with self similar indenters [59]. In light of such observations, it seems several

aspects of the Nix and Gao [52] model, including the use of Taylor's hardening law, may deserve reevaluation [59].

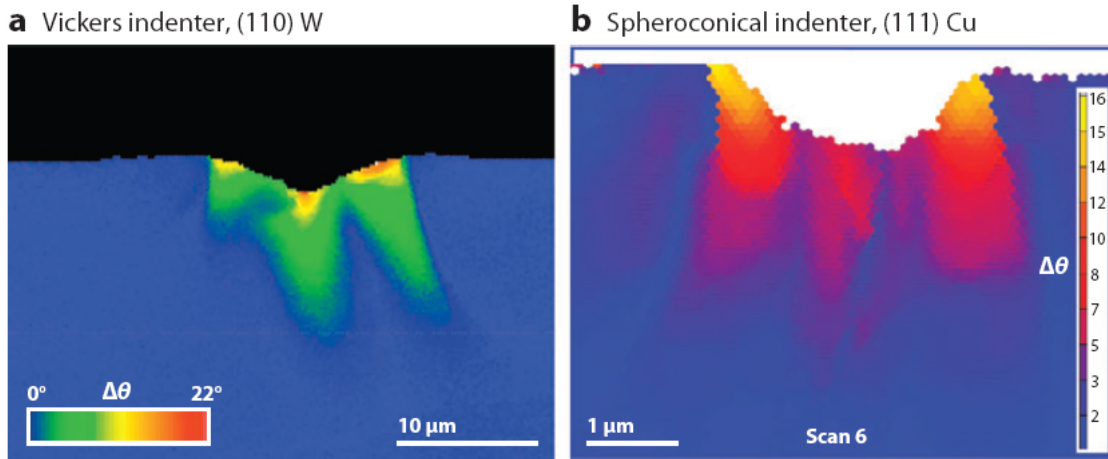


Figure 16. Lattice rotation maps of indentations in W and Cu crystals

Finally, it has also been noted [59] that in some studies [68,69], dislocation source limitation has been emphasized as a potential mechanism of the ISE at shallow indentation depths. For very small indentation volumes, it is expected that there will be a lack of available dislocation sources to activate to accommodate the plastic deformation [69]. In these cases the assumption in the Nix and Gao [52] model really become questionable since dislocations emitted from discrete sources may be very short and could travel long distances before entanglement, pileup, etc. [69]. Such behavior necessitates high stresses under the indenter to move the dislocations, hence an ISE [59,69].

2.4.2 Indentation Size Effects in Electromechanically Coupled Materials

Although much attention has been given to understanding the ISE in metals and some other nonmetals such as MgO, there has been increasing interest in explaining size

effects observed in ferroelectric and piezoelectric materials. The ISE has now been reported in electromechanically coupled materials including barium titanate [1,2,70,71], lead zirconate titanate (PZT) [72], and lithium niobate [73]. The nature of the ISE in these materials varies, as do the explanations.

Hurtado-Macias et al. [72] observed ISE when performing cube corner, Berkovich, and sphero-conical indentations on tetragonal PZT ceramics (polycrystalline) doped with 0.8 mol% of La_2O_3 at compositions close to the morphotropic phase boundary. The term morphotropic phase boundary (MPB) indicates a composition dependent rather than temperature dependent phase boundary [22], and in PZT and many ferroelectrics it refers to a metastable tetragonal-rhombohedral phase boundary [74]. Piezoelectric, dielectric, and other properties are typically enhanced in materials with compositions close to the MPB [24,74]. Hurtado-Macias et al. [72] found that while measurements of reduced elastic modulus for each PZT composition did not vary appreciably with indenter geometry, hardness measurements clearly depended on the tip radius. Applying the model developed by Swadener et al. [53] for spherical tipped indenters and based on Nix and Gao's [52] GND analysis, they determined that there was good agreement between the model and the experimental data for indents leaving small residual contact radii (less than $\sim 1500\text{nm}$) [72]. For larger residual contact radii, the model predicted higher hardness values than were actually measured. To explain the discrepancy between the model and experimental data, Hurtado-Macias et al. [72] believed that the volume dependent phenomenon of ferroelastic domain switching, for which the stresses required are easily surpassed during indentation, make the material behave more softly. Ferroelasticity is the elastic analogue to ferroelectricity; it describes a

material's ability to exhibit two or more spontaneous strain orientation states in the absence of mechanical stress and can be shifted from one state to another by mechanical stress [75]. Hurtado-Macias et al. [72] reasoned that at some critical volume of plastic deformation, ferroelastic domain switching in domains neighboring the plastic region occurs in response to the mechanical loading constraint and contributed to lower hardness values.

Size effects in BaTiO₃ have been the subject of several investigations. It appears Scholz et al. [70] were the first to directly draw attention to the ISE in BaTiO₃. They conducted indentation experiments on “giant” (~500μm) grains of self supplied (001) oriented BaTiO₃ and found that hardness values increased from 9GPa to 19GPa with decreases in indenter radius and with no dependence on the type of domain being indented. Scholz et al. [70] showed that their results fit Swadener et al.'s [53] model for all but the sharpest indenter (~61nm radius cube corner), indicating support for GND arguments. They did consider domain effects, stating that domain wall motion may result in some loading hysteresis but with no severe effect. Based on energetic arguments, they concluded that while some domain nucleation probably takes place during indentation, it is not expected to be a dominant effect, particularly before any pop-in activity.

Buchs et al. [71] studied Vickers indentation and nanoindentation with spherical indenters in (001) and (110) oriented BaTiO₃ and observed a type of ISE when comparing plots of stress versus indentation strain (R/a , where R is tip radius and a is contact radius). These plots revealed that for spherical indenters of decreasing radii, higher stresses are encountered at the onset of plasticity, i.e. stochastically occurring pop-ins. Buchs et al. [71] explained these results in terms of dislocation and domain behavior,

arguing on the basis of previous work with lithium niobate [76] that when pop-ins occur, the size of new domains nucleated under the indenter scale with the indenter tip radius; sharper tips result in smaller domains. Also thought to be associated with the nucleation of new domains are dislocation loops comprising incipient kink bands (IKBs) which would spontaneously annihilate if mechanical loading were to be removed. Decreasing domain size in conjunction with IKB activity was declared responsible for the size dependency in the indentation stress versus indentation strain plots. The nature of the size effect observed by Buchs et al. [71], that is, stress-strain size dependency that does not appear to present itself until the occurrence of a pop-in event, limits direct comparison with the work of Scholz et al. [70].

Gharbi et al. [1,2] have proposed that the flexoelectric effect, as opposed to dislocation or domain activity, is the most probable source of some size dependent behavior in BaTiO₃. To support this argument they analytically derived an expression inter-relating contact stiffness and contact radius for piezoelectric materials incorporating flexoelectricity and fit this model to data from nanoindentations performed on (001) oriented BaTiO₃ with a Berkovich indenter. The flexoelectric constant, deduced from fit parameters used to match the model to the experimental data, was found to be in surprisingly good agreement with the same constant determined by other research groups testing bulk samples. Gharbi et al. [1,2] pose two major implications: (i) size effects in electromechanically coupled materials, particularly ferroelectrics, may depend on several complicated and inter-related processes, and (ii) flexoelectric properties of crystals may be estimated from nanoindentation testing if other material properties are sufficiently

known. Details relating to the manner in which flexoelectricity affects mechanical properties during indentation are provided in the following section.

2.5 Modeling of Electromechanical Materials during Indentation

The procedure developed by Gharbi et al. [1,2] for estimating flexoelectric properties of crystals based on nanoindentation data relies on an analytical model of indentation of a transversely isotropic material by a flat circular indenter of radius a as shown schematically in Figure 17 [2]. The flexoelectric indentation model expands on the work of Karapetian et al. [77], who developed closed form solutions for indentation of a piezoelectric half space for several indenter geometries. Sections 2.5.1 and 2.5.2 summarize the work of Karapetian et al. [77] and Gharbi et al. [2] which led to expressions inter-relating applied concentrated force P , concentrated charge Q , indentation depth w and tip potential ψ_0 . Section 2.5.3 addresses utilization of the model results in conjunction with nanoindentation data to estimate flexoelectric properties. Assumptions and limitations associated with the model will be highlighted.

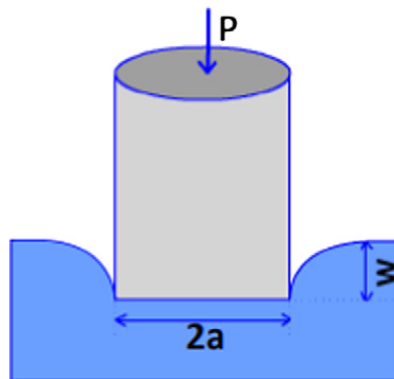


Figure 17. Indentation of an elastic half space by a rigid flat punch

2.5.1 Indentation of a Transversely Isotropic Piezoelectric Half Space

Karapetian et al.'s [77] solution for indentation of a purely piezoelectric, elastic, transversely isotropic half space, as summarized by Gharbi et al. [2], is provided here, and their notation is retained for clarity. Please note that the d_{ij} are in fact piezoelectric stress constants (inter-relating stress and electric field, traditionally denoted by e_{ij}), not piezoelectric strain constants. The unit scheme is as follows: N/m^2 for elastic constants, C/m^2 for piezoelectric coupling, and F/m for dielectric permeability. Table 4 provides a description of nomenclature.

Table 4. Nomenclature for development of the piezoelectric indentation model

Symbol	Description	Symbol	Description
σ_{ij}	Stresses	a_{ij}	Dielectric constants
C_{ij}	Stiffness constants	a	Indenter contact radius
u_i	Displacements	P	Concentrated load
ψ	Electric (tip) potential	Q	Concentrated charge
d_{ij}	Piezoelectric stress constants	w	Indentation depth
D_i	Electric displacements		

The linear constitutive equations take the form

$$\sigma_{xx} = C_{11} \frac{\partial u_x}{\partial x} + (C_{11} - 2C_{66}) \frac{\partial u_y}{\partial y} + C_{13} \frac{\partial u_z}{\partial z} + d_{31} \frac{\partial \psi}{\partial z},$$

Eqn. 25

$$\sigma_{yy} = (C_{11} - 2C_{66}) \frac{\partial u_x}{\partial x} + C_{11} \frac{\partial u_y}{\partial y} + C_{13} \frac{\partial u_z}{\partial z} + d_{31} \frac{\partial \psi}{\partial z},$$

$$\sigma_{zz} = C_{13} \frac{\partial u_x}{\partial x} + C_{13} \frac{\partial u_y}{\partial y} + C_{33} \frac{\partial u_z}{\partial z} + d_{33} \frac{\partial \psi}{\partial z},$$

$$\sigma_{xy} = C_{66} \left(\frac{\partial u_x}{\partial y} + \frac{\partial u_y}{\partial x} \right),$$

$$\sigma_{yz} = C_{44} \left(\frac{\partial u_y}{\partial z} + \frac{\partial u_z}{\partial y} \right) + d_{15} \frac{\partial \psi}{\partial y},$$

$$\sigma_{zx} = C_{44} \left(\frac{\partial u_x}{\partial z} + \frac{\partial u_z}{\partial x} \right) + d_{15} \frac{\partial \psi}{\partial x},$$

and

$$D_x = d_{15} \left(\frac{\partial u_x}{\partial z} + \frac{\partial u_z}{\partial x} \right) - a_{11} \frac{\partial \psi}{\partial x},$$

$$D_y = d_{15} \left(\frac{\partial u_y}{\partial z} + \frac{\partial u_z}{\partial y} \right) - a_{11} \frac{\partial \psi}{\partial y},$$

Eqn. 26

$$D_z = d_{31} \left(\frac{\partial u_x}{\partial x} + \frac{\partial u_y}{\partial y} \right) + d_{33} \frac{\partial u_z}{\partial z} - a_{33} \frac{\partial \psi}{\partial z}.$$

The equilibrium equations $\partial \sigma_{ij} / \partial x_i = 0$ and equations of electrostatics $\partial D_i / \partial x_i = 0$ are

$$\begin{aligned} & C_{11} \frac{\partial^2 u_x}{\partial x^2} + C_{66} \frac{\partial^2 u_x}{\partial y^2} + C_{44} \frac{\partial^2 u_x}{\partial z^2} + (C_{11} - C_{66}) \frac{\partial^2 u_y}{\partial x \partial y} + (C_{13} + C_{44}) \frac{\partial^2 u_z}{\partial x \partial z}, \\ & + (d_{31} + d_{15}) \frac{\partial^2 \psi}{\partial x \partial z} = 0 \end{aligned}$$

Eqn. 27

$$C_{66} \frac{\partial^2 u_y}{\partial x^2} + C_{11} \frac{\partial^2 u_y}{\partial y^2} + C_{44} \frac{\partial^2 u_y}{\partial z^2} + (C_{11} - C_{66}) \frac{\partial^2 u_x}{\partial x \partial y} + (C_{13} + C_{44}) \frac{\partial^2 u_z}{\partial y \partial z},$$

$$+ (d_{31} + d_{15}) \frac{\partial^2 \psi}{\partial y \partial z} = 0$$

$$C_{44} \left(\frac{\partial^2 u_z}{\partial x^2} + \frac{\partial^2 u_z}{\partial y^2} \right) + C_{33} \frac{\partial^2 u_z}{\partial z^2} + (C_{44} + C_{13}) \left(\frac{\partial^2 u_x}{\partial x \partial z} + \frac{\partial^2 u_y}{\partial y \partial z} \right) + d_{15} \left(\frac{\partial^2 \psi}{\partial x^2} + \frac{\partial^2 \psi}{\partial y^2} \right),$$

$$+ d_{33} \frac{\partial^2 \psi}{\partial z^2} = 0$$

$$d_{15} \left(\frac{\partial^2 u_z}{\partial x^2} + \frac{\partial^2 u_z}{\partial y^2} \right) + d_{33} \frac{\partial^2 u_z}{\partial z^2} + (d_{15} + d_{31}) \left(\frac{\partial^2 u_x}{\partial x \partial z} + \frac{\partial^2 u_y}{\partial y \partial z} \right) - a_{11} \left(\frac{\partial^2 \psi}{\partial x^2} + \frac{\partial^2 \psi}{\partial y^2} \right)$$

$$- a_{33} \frac{\partial^2 \psi}{\partial z^2} = 0$$

The following complex notations are used for displacements, u_i , stresses, σ_{ij} , electric potential ψ , and electric displacements D_i :

$$u \equiv u_x + iu_y, u_z, \psi, D \equiv D_x + iD_y, D_z,$$

Eqn. 28

$$\sigma_1 \equiv \sigma_{xx} + \sigma_{yy}, \sigma_2 \equiv \sigma_{xx} - \sigma_{yy} + 2i\sigma_{xy}, \sigma_{zz}, \tau_z \equiv \sigma_{zx} + i\sigma_{yz}.$$

The expressions

$$\alpha_j^* = C_{44} (1 + m_j^*) + d_{15} k_j^* \quad (j = 1, 2, 3),$$

Eqn. 29

and

$$\beta_j^* = d_{15} (1 + m_j^*) - a_{11} k_j^* \quad (j = 1, 2, 3),$$

Eqn. 30

in which m_j^* and k_j^* ($j = 1, 2, 3$) are defined by

$$m_j^* = \frac{(C_{11}\gamma_j^{*2} - C_{44})(a_{33} - \gamma_j^{*2} a_{11}) + \gamma_j^{*2} (d_{15} + d_{31})^2}{(d_{33} - \gamma_j^{*2} d_{15})(d_{15} + d_{31}) + (C_{13} + C_{44})(a_{33} - \gamma_j^{*2} a_{11})}, \quad \text{Eqn. 31}$$

and

$$k_j^* = \frac{(C_{11}\gamma_j^{*2} - C_{44})(d_{33} - \gamma_j^{*2} d_{15}) - \gamma_j^{*2} (d_{15} + d_{31})(C_{13} + C_{44})}{(d_{33} - \gamma_j^{*2} d_{15})(d_{15} + d_{31}) + (C_{13} + C_{44})(a_{33} - \gamma_j^{*2} a_{11})}, \quad \text{Eqn. 32}$$

are introduced to reduce clutter. In these relations $\gamma_j^{*2} = \lambda_j$ are roots of the cubic equation

$$A\lambda_j^3 - B\lambda_j^2 + C\lambda_j - D = 0, \quad \text{Eqn. 33}$$

where A, B, C, and D are defined as

$$A = C_{11}(C_{44}a_{11} + d_{15}^2),$$

$$B = C_{44}[C_{11}a_{33} + (d_{15} + d_{31})^2] + a_{11}[C_{11}C_{33} + C_{44}^2 - (C_{13} + C_{44})^2],$$

$$+ 2d_{15}[C_{11}d_{33} - (C_{13} + C_{44})(d_{15} + d_{31})] + C_{44}d_{15}^2$$

Eqn. 34

$$C = C_{33}[C_{44}a_{11} + (d_{15} + d_{31})^2] + a_{33}[C_{11}C_{33} + C_{44}^2 - (C_{13} + C_{44})^2],$$

$$+ 2d_{33}[C_{44}d_{15} - (C_{13} + C_{44})(d_{15} + d_{31})] + C_{11}d_{33}^2$$

$$D = C_{44}(C_{33}a_{33} + d_{33}^2).$$

The cubic equation above follows from

$$\begin{aligned} \frac{C_{44} + m_j^*(C_{13} + C_{44}) + k_j^*(d_{15} + d_{31})}{C_{11}} &= \frac{m_j^*C_{33} + k_j^*d_{33}}{m_j^*C_{44} + (C_{13} + C_{44}) + k_j^*d_{15}}. \\ &= \frac{m_j^*d_{33} - k_j^*a_{33}}{m_j^*d_{15} + (d_{15} + d_{31}) - k_j^*a_{11}} = \gamma_j^{*2} \equiv \lambda_j, \gamma_4^* = \sqrt{\frac{C_{44}}{C_{66}}} \end{aligned} \quad \text{Eqn. 35}$$

Combinations of piezoelectric constants to be used are defined as

$$H^* = \frac{1}{2\pi(d_{15}^2 + c_{44}a_{11}) \sum_{j=1}^3 (\alpha_j^* a_j^* / \gamma_j^{*2})} = -\frac{1}{2\pi \sum_{j=1}^3 \alpha_j^* N_j^*},$$

$$N_1^* = \frac{\alpha_3^* \beta_2^*}{\gamma_3^*} - \frac{\alpha_2^* \beta_3^*}{\gamma_2^*}, \quad L_1^* = \frac{\alpha_3^* \alpha_2^*}{\gamma_3^*} - \frac{\alpha_2^* \alpha_3^*}{\gamma_2^*},$$

$$a_1^* = \gamma_1^* \left[(1 + m_2^*) k_3^* - (1 + m_3^*) k_2^* \right], \quad 1 \rightarrow 2 \rightarrow 3 \rightarrow 1$$

Eqn. 36

$$C_1^* = -\frac{1}{B^*} \sum_{j=1}^3 \frac{k_j^*}{\gamma_j^*} L_j^*, \quad C_2^* = \frac{1}{B^*} \sum_{j=1}^3 \frac{k_j^*}{\gamma_j^*} N_j^*,$$

$$C_3^* = \frac{1}{B^*} \sum_{j=1}^3 \frac{m_j^*}{\gamma_j^*} L_j^*, \quad C_4^* = -\frac{1}{B^*} \sum_{j=1}^3 \frac{m_j^*}{\gamma_j^*} N_j^*,$$

$$B^* = H^* \left[\sum_{j=1}^3 \frac{m_j^*}{\gamma_j^*} N_j^* \sum_{i=1}^3 \frac{k_i^*}{\gamma_i^*} L_i^* - \sum_{j=1}^3 \frac{m_j^*}{\gamma_j^*} L_j^* \sum_{i=1}^3 \frac{k_i^*}{\gamma_i^*} N_i^* \right].$$

Geometric parameters to be used are defined as

$$2l_{1j}(z) = \sqrt{(a + \rho)^2 + z_j^2} - \sqrt{(a - \rho)^2 + z_j^2},$$

$$2l_{2j}(z) = \sqrt{(a + \rho)^2 + z_j^2} + \sqrt{(a - \rho)^2 + z_j^2},$$

Eqn. 37

$$z_j = z / \gamma_j^*$$

Solving the equilibrium and electrostatics equations involves superposition of two fields in sub-problems with purely mechanical then purely electrical boundary conditions. For the purely mechanical problem (zero electric conditions, $\psi = 0$ for $0 \leq \rho < \infty$) the boundary conditions are:

$$u_z = w \text{ for } 0 \leq \rho < a,$$

$$\sigma_{zz} = 0 \text{ for } \rho > a, \quad \text{Eqn. 38}$$

$$\tau_z = 0 \text{ for } 0 \leq \rho < \infty.$$

So, we have

$$u = -\frac{2wH^*}{\pi} \sum_{j=1}^3 [N_j^* C_1^* + L_j^* C_2^*] \frac{ae^{i\phi}}{\rho} \left[1 - \frac{(a^2 - l_{1j}^2)^{1/2}}{a} \right],$$

$$u_z = -\frac{2wH^*}{\pi} \sum_{j=1}^3 \frac{m_j^*}{\gamma_j^*} [N_j^* C_1^* + L_j^* C_2^*] \arcsin\left(\frac{a}{l_{2j}}\right), \quad \text{Eqn. 39}$$

$$\psi = -\frac{2wH^*}{\pi} \sum_{j=1}^3 \frac{k_j^*}{\gamma_j^*} [N_j^* C_1^* + L_j^* C_2^*] \arcsin\left(\frac{a}{l_{2j}}\right).$$

For $z = 0$ and $\rho < a$ it can be shown for normal stresses that

$$\sigma_{zz}(\rho, 0) = -\frac{C_1^* w}{\pi^2 (a^2 - \rho^2)^{1/2}}, \quad \text{Eqn. 40}$$

$$D_z(\rho, 0) = \frac{C_2^* w}{\pi^2 (a^2 - \rho^2)^{1/2}}.$$

For the purely electrical problem (zero mechanical conditions, $u_z = 0$ for $0 \leq \rho < \infty$), the boundary conditions are

$$\psi = \psi_0 \text{ for } 0 \leq \rho < a,$$

Eqn. 41

$$D_z = 0 \text{ for } \rho > a.$$

So, we have

$$u = -\frac{2\psi_0 H^*}{\pi} \sum_{j=1}^3 [N_j^* C_3^* + L_j^* C_4^*] \frac{a e^{i\phi}}{\rho} \left[1 - \frac{(a^2 - l_{1j}^2)^{1/2}}{a} \right],$$

$$u_z = -\frac{2\psi_0 H^*}{\pi} \sum_{j=1}^3 \frac{m_j^*}{\gamma_j^*} [N_j^* C_3^* + L_j^* C_4^*] \arcsin\left(\frac{a}{l_{2j}}\right),$$

Eqn. 42

$$\psi = -\frac{2\psi_0 H^*}{\pi} \sum_{j=1}^3 \frac{k_j^*}{\gamma_j^*} [N_j^* C_3^* + L_j^* C_4^*] \arcsin\left(\frac{a}{l_{2j}}\right).$$

For $z = 0$ and $\rho < a$ it can be shown for normal stresses that

$$\sigma_{zz}(\rho, 0) = -\frac{C_3^* \psi_0}{\pi^2 (a^2 - \rho^2)^{1/2}},$$

Eqn. 43

$$D_z(\rho, 0) = \frac{C_4^* \psi_0}{\pi^2 (a^2 - \rho^2)^{1/2}}.$$

We integrate the normal stress and electric displacement at $z = 0$ over the contact area,

$$P = -2\pi \int_0^a \sigma_{zz}(\rho, 0) \rho d\rho ,$$

Eqn. 44

$$Q = 2\pi \int_0^a D_z(\rho, 0) \rho d\rho ,$$

to finally obtain the following relationships:

$$P = \frac{2aC_1^* w}{\pi} + \frac{2aC_3^* \psi_0}{\pi} ,$$

Eqn. 45

$$Q = \frac{2aC_2^* w}{\pi} + \frac{2aC_4^* \psi_0}{\pi} .$$

These expressions provide the desired relationships between applied concentrated force P , concentrated charge Q , indentation depth w and tip potential ψ_0 for a piezoelectric, elastic, transversely isotropic half space loaded by a flat punch indenter.

2.5.2 Incorporation of Flexoelectric Behavior into the Piezoelectric Model

The analytical work of Gharbi et al. [2] in the development of stiffness relations incorporating flexoelectricity begins with the setup of a boundary value problem. Equations governing a piezoelectric flexoelectric continuum dielectric of volume V bounded by a surface S in a vacuum V' are

$$\nabla \cdot \sigma + f = \rho \ddot{u} \text{ where } \sigma = c : S + d \cdot P + (e - f) : \nabla P \text{ in } V ,$$

$$\bar{E} + \nabla \cdot \tilde{E} - \nabla \varphi + E^0 = 0 \text{ in } V ,$$

Eqn. 46

$$-\varepsilon_0 \Delta \varphi + \nabla \cdot P = 0 \text{ in } V , \text{ and}$$

$\Delta\varphi = 0$ in V' , where

$$-\bar{E} = a \cdot P + g : \nabla P + f : \nabla \nabla u + d : S, \text{ and}$$

$$\tilde{E} = b : \nabla P + e : S + g \cdot P.$$

The second order reciprocal dielectric susceptibility tensor where is a , c is the fourth order elastic tensor, d is the third order piezoelectric tensor, f is the fourth order flexoelectric tensor, b is the fourth order polarization gradient–polarization gradient coupling tensor, fourth order tensor e corresponds to polarization gradient and strain coupling, and g is the polarization-polarization gradient coupling tensor. Effects of b and e are neglected in the indentation model. Boundary conditions are

$$\sigma \cdot n = t,$$

$$\tilde{E} \cdot n = 0,$$

Eqn. 47

$$(-\varepsilon_0 \|\varphi\| + P) \cdot n = 0.$$

For conciseness, the term $\varepsilon = \frac{\varepsilon_1}{a} = \frac{f_{ij}}{ad^*}$ for all $i, j = 1, 2, 3$, where

$d^* = \frac{|d_{15}| + |d_{31}| + |d_{33}|}{3}$, is introduced to represent the ratio of the flexoelectric component

f_{ij} to the product of contact radius a and effective piezoelectric constant d^* . The constitutive equations for the piezoelectric transversely isotropic material are then

$$\frac{\sigma_{ij}}{ad^*} = \frac{C_{ijkl}}{ad^*} S_{kl} + \varepsilon_0^{-1} \frac{d_{kij}}{ad^*} P_k - q \varepsilon_0^{-1} P_{l,k}, \quad \text{Eqn. 48}$$

$$\frac{D_i}{ad^*} = \frac{d_{ikl}}{ad^*} S_{kl} - \varepsilon_0^{-1} \frac{a_{ik}}{ad^*} P_k + qS_{kl,j}.$$

Rewriting the equilibrium and electrostatics equations $\partial\sigma_{ij}/\partial x_i = 0$ and $\partial D_i/\partial x_i = 0$ yield a system of four equations for displacements u_x, u_y, u_z and polarizations P_x, P_y and P_z :

$$\frac{C_{ijkl}}{ad^*} S_{kl,i} + \varepsilon_0^{-1} \frac{d_{kij}}{ad^*} P_{k,i} - q\varepsilon_0^{-1} P_{l,ki} = 0,$$

Eqn. 49

$$\frac{d_{ikl}}{ad^*} S_{kl,i} - \varepsilon_0^{-1} \frac{a_{ik}}{ad^*} P_{k,i} + qS_{kl,ji} = 0.$$

The final required equation is

$$P_{i,i} - \varepsilon_0 \psi_{,ii} = 0.$$

Eqn. 50

Gharbi et al. [2] note that the problem stated above is too complex for an exact solution, so it is approached as a singular perturbation problem where “inner” and “outer” problem solutions are developed separately then combined as an entire solution. Details of derivations for the inner and outer solutions need not be discussed here. The entire solution for displacements u_x, u_y, u_z and potential ψ is determined as follows. For the purely mechanical problem,

$$u_x = -\cos(\phi) \frac{2wH^*}{\pi} \sum_{j=1}^3 [N_j^* C_1^* + L_j^* C_2^*] \frac{a}{\rho} \left[1 - \frac{(a^2 - l_{1j}^2)^{1/2}}{a} \right] \\ + \text{sign}(a - \rho) \frac{w}{\pi^2 a} F_1(z) \cos(\phi) \sqrt{\frac{(C_{44} a_{11} + d_{15}^2)}{C_{11} C_{44}}} e^{-A^i \left| \frac{\rho - a}{\varepsilon_1} \right|},$$

Eqn. 51

$$\begin{aligned}
u_y &= -\sin(\phi) \frac{2wH^*}{\pi} \sum_{j=1}^3 [N_j^* C_1^* + L_j^* C_2^*] \frac{a}{\rho} \left[1 - \frac{(a^2 - l_{1j}^2)^{1/2}}{a}\right] \\
&\quad + \text{sign}(a - \rho) \frac{w}{\pi^2 a} F_1(z) \sin(\phi) \sqrt{\frac{(C_{44} a_{11} + d_{15}^2)}{C_{11} C_{44}}} e^{-A^i \left| \frac{\rho - a}{\varepsilon_1} \right|}, \\
u_z &= -\frac{2wH^*}{\pi} \sum_{j=1}^3 \frac{m_j^*}{\gamma_j^*} [N_j^* C_1^* + L_j^* C_2^*] \arcsin\left(\frac{a}{l_{2j}}\right) - \frac{w}{\pi^2 a} \frac{d_{15}}{C_{44}} F_1(z) e^{-A^i \left| \frac{\rho - a}{\varepsilon_1} \right|}, \\
\psi &= -\frac{2wH^*}{\pi} \sum_{j=1}^3 \frac{k_j^*}{\gamma_j^*} [N_j^* C_1^* + L_j^* C_2^*] \arcsin\left(\frac{a}{l_{2j}}\right) + \frac{w}{\pi^2 a} F_1(z) e^{-A^i \left| \frac{\rho - a}{\varepsilon_1} \right|}.
\end{aligned}$$

For the purely electrical problem,

$$\begin{aligned}
u_x &= -\cos(\phi) \frac{2\psi_0 H^*}{\pi} \sum_{j=1}^3 [N_j^* C_3^* + L_j^* C_4^*] \frac{a}{\rho} \left[1 - \frac{(a^2 - l_{1j}^2)^{1/2}}{a}\right] \\
&\quad + \text{sign}(a - \rho) \cos(\phi) \frac{\psi_0}{\pi^2 a} F_6(z) \sqrt{\frac{(C_{44} a_{11} + d_{15}^2)}{C_{11} C_{44}}} e^{-A^i \left| \frac{\rho - a}{\varepsilon_1} \right|}, \\
u_y &= -\sin(\phi) \frac{2\psi_0 H^*}{\pi} \sum_{j=1}^3 [N_j^* C_3^* + L_j^* C_4^*] \frac{a}{\rho} \left[1 - \frac{(a^2 - l_{1j}^2)^{1/2}}{a}\right] \\
&\quad + \text{sign}(a - \rho) \sin(\phi) \frac{\psi_0}{\pi^2 a} F_6(z) \sqrt{\frac{(C_{44} a_{11} + d_{15}^2)}{C_{11} C_{44}}} e^{-A^i \left| \frac{\rho - a}{\varepsilon_1} \right|}, \\
u_z &= -\frac{2\psi_0 H^*}{\pi} \sum_{j=1}^3 \frac{m_j^*}{\gamma_j^*} [N_j^* C_3^* + L_j^* C_4^*] \arcsin\left(\frac{a}{l_{2j}}\right) - \frac{\psi_0}{\pi^2 a} \frac{d_{15}}{C_{44}} F_6(z) e^{-A^i \left| \frac{\rho - a}{\varepsilon_1} \right|}, \\
\psi &= -\frac{2\psi_0 H^*}{\pi} \sum_{j=1}^3 \frac{k_j^*}{\gamma_j^*} [N_j^* C_3^* + L_j^* C_4^*] \arcsin\left(\frac{a}{l_{2j}}\right) + \frac{\psi_0}{\pi^2 a} F_6(z) e^{-A^i \left| \frac{\rho - a}{\varepsilon_1} \right|}.
\end{aligned} \tag{Eqn. 52}$$

Gharbi et al. [2] were not able to express the functions $F_1(z)$ and $F_6(z)$ explicitly, but they satisfy the normal displacement and potential boundary conditions of $F_1(0)=0$, $F_6(0)=0$ of the outer solution. A^i is defined as

$$A^i = \frac{1}{d^*} \sqrt{\frac{C_{11}(d_{15}^2 + C_{44}a_{11})}{C_{44}}} . \quad \text{Eqn. 53}$$

From the entire solution above, the stiffness relations linking applied force, P , and concentrated charge, Q to indentation depth w and ψ_0 may be determined. Normal stresses and normal electric displacements for $\rho < a$ (the contact zone) for the purely mechanical problem are

$$\sigma_{zz}^m = -\frac{C_1^* w}{\pi^2 (a^2 - \rho^2)^{1/2}} + \frac{f_1^* w}{\pi^2 a} e^{A^i \left(\frac{\rho-a}{\varepsilon_1}\right)} ,$$

Eqn. 54

$$\text{and } D_z^m = \frac{C_2^* w}{\pi^2 (a^2 - \rho^2)^{1/2}} - \frac{f_2^* w}{\pi^2 a} e^{A^i \left(\frac{\rho-a}{\varepsilon_1}\right)} ,$$

and for the purely electrical problem are

$$\sigma_{zz}^e = -\frac{C_3^* \psi_0}{\pi^2 (a^2 - \rho^2)^{1/2}} + \frac{f_3^* \psi_0}{\pi^2 a} e^{A^i \left(\frac{\rho-a}{\varepsilon_1}\right)} ,$$

Eqn. 55

$$\text{and } D_z^e = \frac{C_4^* \psi_0}{\pi^2 (a^2 - \rho^2)^{1/2}} - \frac{f_4^* w}{\pi^2 a} e^{A^i \left(\frac{\rho-a}{\varepsilon_1}\right)} ,$$

where f_1^* , f_2^* , f_3^* , and f_4^* are defined as

$$f_1^* = \alpha^{flex} \frac{(C_{44}d_{33} - C_{33}d_{15})}{C_{44}},$$

$$f_2^* = \alpha^{flex} \frac{(d_{15}d_{33} + C_{44}a_{33})}{C_{44}},$$

$$f_3^* = \beta^{flex} \frac{(C_{44}d_{33} - C_{33}d_{15})}{C_{44}},$$

$$f_4^* = \beta^{flex} \frac{(d_{15}d_{33} + C_{44}a_{33})}{C_{44}}.$$

Eqn. 56

The terms α^{flex} and β^{flex} are basically integration constants that must be estimated by fitting a theoretical normal polarization versus ρ curve to a set of data points determined by numerical FEM modeling for a given material.

Finally, by integrating the normal stress and normal electric displacement relations, we obtain the stiffness relations with the flexoelectric effect taken into account:

$$P = \frac{2a}{\pi} (C_1^* w + C_3^* \psi_0) - \frac{2}{\pi a} (f_1^* w + f_3^* \psi_0) f_{\varepsilon_1}(a),$$

Eqn. 57

$$Q = \frac{2a}{\pi} (C_1^* w + C_3^* \psi_0) - \frac{2}{\pi a} (f_2^* w + f_4^* \psi_0) f_{\varepsilon_1}(a),$$

where

$$f_{\varepsilon_1}(a) = \frac{\varepsilon_1}{(A^i)^2} \left(\varepsilon_1 e^{-\frac{A^i}{\varepsilon_1} a} - \varepsilon_1 + A^i a \right).$$

Eqn. 58

Notice that setting $f_{ij} = 0$ makes $\varepsilon_1 = 0$, so $f_{\varepsilon_1}(a) = 0$ and the above relations for P and Q match those of a purely piezoelectric indentation model as determined by Karapetian et al. [77].

2.5.3 Usage of the Model in Conjunction with Nanoindentation Data

For the purposes of comparing the analytical model with nanoindentation data, we consider purely mechanical loading and set $\psi_0 = 0$ [2]. This reduces the mechanical loading equation to

$$P = \frac{2a}{\pi} C_1^* w - \frac{2}{\pi a} f_1^* w f_{\varepsilon_1}(a). \quad \text{Eqn. 59}$$

If we consider the case without flexoelectricity, we simply have

$$P = \frac{2a}{\pi} C_1^* w. \quad \text{Eqn. 60}$$

Noting that the contact stiffness is given by

$$s = \frac{\partial P}{\partial w}, \quad \text{Eqn. 61}$$

it is apparent that the ratios of contact stiffness to contact radius for the piezoelectric-flexoelectric and piezoelectric-only cases are

$$\frac{s}{a} = \frac{2}{\pi} C_1^* - \frac{2}{\pi a^2} f_1^* f_{\varepsilon_1}(a) \quad \text{Eqn. 62}$$

and

$$\frac{s}{a} = \frac{2}{\pi} C_1^*, \quad \text{Eqn. 63}$$

respectively. Comparing the two relations, the contact stiffness normalized with respect to contact radius in the case of a purely piezoelectric material should be constant and depends only on the composite material property C_1^* (recall C_1^* only depends on dielectric, stiffness, and piezoelectric tensor components of the material). In the case of a simultaneously piezoelectric and flexoelectric material, however, the normalized contact stiffness still varies with contact radius with the flexoelectric term becoming more influential for smaller contact radii. This size-dependent behavior is expected with flexoelectric behavior due to strain gradient scaling phenomenon previously discussed.

Normalized contact stiffness and contact radius may easily be calculated from nanoindentation systems capable of CSM. From plots of normalized contact stiffness as a function of contact radius, the magnitude of the flexoelectric coefficient for a given material and orientation may be estimated by fitting the flexoelectric model equation to the data. Gharbi et al. [2] used these facts to verify their model. Nanoindentation experiments using a Berkovich indenter and the CSM technique were conducted on Z-cut quartz and (001) oriented BaTiO₃ single crystals. The resulting normalized contact stiffness versus contact radius plots as well as the analytical model for both materials are shown in Figure 18 [1].

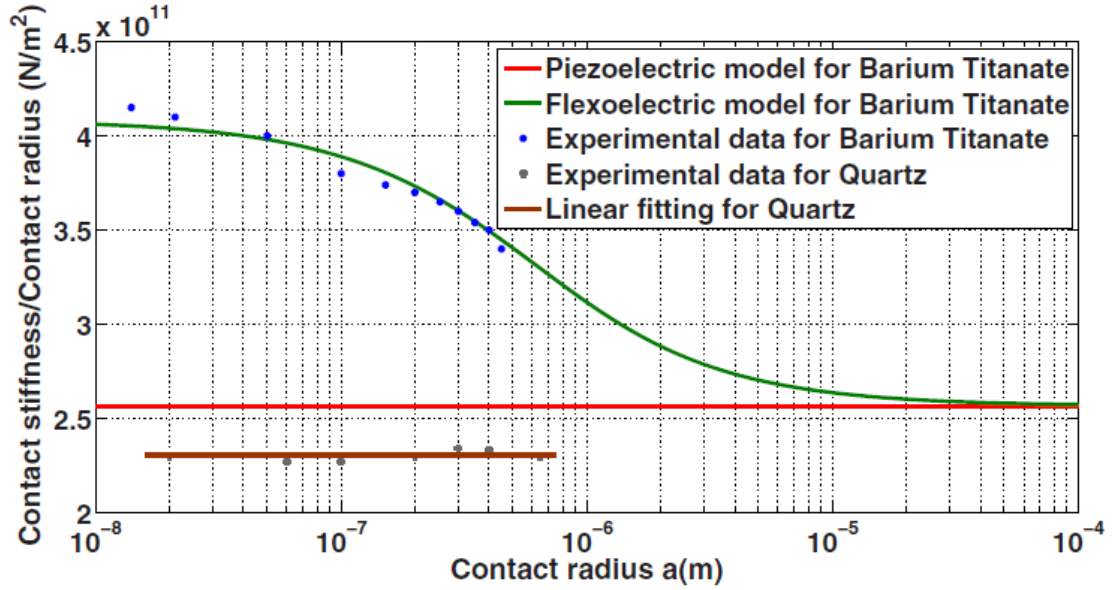


Figure 18. Indentation results for quartz and BaTiO₃ compared with model predictions

Results indicate that a linear fit of zero slope adequately describes the stiffness behavior of the quartz over the range of reported contact radii; there is no observed size dependency. This result indicates, as expected, quartz is not a strongly flexoelectric material. A linear fit does not, however, adequately describe the size dependent stiffness in the BaTiO₃, which Cross et al. [13] had already demonstrated as being relatively strongly flexoelectric. By adjusting the ε_1 term Eqn. 62 to correspond to the flexoelectric properties for BaTiO₃ determined by bending, the flexoelectric model curve in Figure 18 is made to fit neatly over the experimental data [1]. For materials where the flexoelectric properties are unknown, once a suitable value for ε_1 is determined, the flexoelectric coefficient f_{ij} for the material may be estimated from

$$\varepsilon_1 = \frac{f_{ij}}{d^*}. \quad \text{Eqn. 64}$$

Gharbi et al. [2] estimated that $f_{12}^{BaTiO_3} \approx 4 \times 10^{-6} C/m$, which agrees fairly well with results of flexure experiments by Cross et al. [13] ($f_{12}^{BaTiO_3} \approx 10 \times 10^{-6} C/m$). Note that while the designation $f_{12}^{BaTiO_3}$ is used in [2] for the final BaTiO₃ flexoelectric property estimate, the model in fact makes no distinction in the subscripts. The subscripts 1 and 2 in $f_{12}^{BaTiO_3}$ are meaningless as the model currently stands because f_{ij} is defined the exact same way for any combination of $i, j = 1, 2, 3$. So while the final results of Gharbi et al. [2] agree well with Cross et al. [13] it must be understood that they are not directly comparable. To emphasize this point the notation f_{ij} will be used when referring to flexoelectric estimates determined with the indentation based approach.

There are basically three concerns discussed by Gharbi et al. [2] regarding the use of the analytical flexoelectric indentation model in conjunction with nanoindentation data to estimate flexoelectric properties. First, there is the issue of indenter geometry. The model is developed for the case of a flat punch indenter, but they are essentially never used in practice. The Berkovich indenter used to produce the data to estimate $f_{ij}^{BaTiO_3}$ is not only a departure from a flat punch in its variable contact area, but it is not even axisymmetric. The non-circular projected contact area of the Berkovich indenter was taken into consideration by calculating an effective contact radius from the indenter area function through $\pi a^2 = f(h_c)$. This treatment seems to be reasonable based on the agreement between the flexure and indentation estimates for $f_{ij}^{BaTiO_3}$, but no other estimates exist for BaTiO₃ using different indenter geometries for comparison.

The second issue concerns general limitations of the model and perturbation theory. Specifically, for contact radii smaller than 100nm, various higher order terms that were neglected in the model may affect the quality of the model fit to the experimental data. Additionally, for values of $\varepsilon_1 > 1$ utilization of the perturbation theory becomes questionable. Since the experimental data and model results reported by Gharbi et al. [2] for BaTiO₃ match up nicely, and their final estimate $f_{ij}^{BaTiO_3} \approx 4 \times 10^{-6} \text{ C/m}$ corresponds with flexure experiments, these matters were tentatively dismissed as having any significant influence on the estimate of f_{ij} . They reference Holmes [78], noting that in perturbation theory, results to certain types of problems often turn out to be more accurate than would generally be expected.

Finally, Gharbi et al. [2] address the possibility that phenomenon other than flexoelectricity, e.g., dislocation or domain activity, may be the source of the observed size effect. While dislocation activity is addressed in terms of BaTiO₃'s relatively high intrinsic hardness (Nix and Gao's GND model is not really applicable) and the lack of any significant size effect in quartz (in which dislocation activity is thought to not be drastically different than that of BaTiO₃), domain activity has not been considered in great detail. Aside from acknowledging that f_{ij} estimates could include both intrinsic and extrinsic parts due to domain wall motion (an acceptable concession in context of the other assumptions made in using the model), domains are not thought to significantly affect the final analysis

One important issue not directly addressed by Gharbi et al. [2] is that some investigators [59,79,80] have reported trouble in using the CSM technique for observing

size effects. Durst et al. [79], in particular, found that when using both Berkovich and cube corner indenters in conjunction with the CSM technique to test Ni single crystals, measured hardness values were significantly lower than when measured using a standard load-unload analysis. Pharr et al. [80] investigated utilization of the CSM technique for observation of indentation size effect in copper crystals and found that the magnitude of underestimation of hardness increased with increasing root-mean-square (RMS) displacement amplitude Δh_{rms} . They discovered that the major source of error during CSM was due to the effects of dynamic unloading, resulting in inaccurate load, displacement, and stiffness calculations. Pharr et al. [80] were able to show that the dynamic unloading effects are drastically enhanced in materials with large ratios of reduced modulus to hardness, E_r/H , such as metals, even for small RMS displacement amplitudes. The ratio E_r/H is about 225 in copper, and ranges from about 10 to 300 for most ceramics and metals [80]. Pharr et al. [80] estimated that in materials with low E_r/H ratios, such as fused quartz ($E_r/H \sim 8$), and for small RMS displacement amplitudes of about 2nm, significant errors may be expected only for very small indentation depths, e.g., 20nm or so with a Berkovich indenter. The E_r/H ratios for quartz and BaTiO₃ are about 20 or less. Assuming the experimental data in [2] were obtained by CSM using a small RMS displacement amplitude, and recognizing that the size effect in BaTiO₃ persists even out to relatively large contact radii (and therefore indentation depths), there is little reason to suspect that dynamic unloading effects significantly impacted the final analysis. Moreover, if dynamic unloading effects were to affect the results, they should have underestimated the ISE [79,80], in which case it could be argued that the estimated $f_{12}^{BaTiO_3}$ value is a conservative one.

2.6 Materials in this Study

Five materials were selected for this study based on their degree of “fit” within the assumptions of the analytical model (e.g., piezoelectric, good rotational symmetry along the loading axis), availability of material constants required for utilization of the model, and the degree of anticipated flexoelectric effect. For Berkovich indentation, quartz and barium titanate will serve as benchmarks for materials exhibiting apparently negligible and strong flexoelectric size effects, respectively.

2.6.1 Quartz (SiO_2)

The term “quartz” almost always refers to α -phase SiO_2 (α -quartz or sometimes “low quartz”) [74]. Quartz is probably the most well known piezoelectric material for a variety of reasons: it is among the earliest known piezoelectrics, it is naturally abundant but rather easy to grow in large quantities and at high quality, and over the past hundred years it has been used in a wide range of military, aerospace, metrology, industrial, and consumer goods applications [74]. Quartz is a member of the trigonal crystal system with point group symmetry 32 [74]. It possesses a z-axis with threefold symmetry and three equivalent x-axes perpendicular to the z-axis and with twofold symmetry [74]. Indentation performed on α -quartz with loading parallel to the z-axis provides a reasonable degree of transverse isotropy for application of the analytical indentation model. The results of Gharbi et al. [2] indicate that the flexoelectric properties of α -quartz are insufficient for the production of an observable indentation size effect for Berkovich indenters and effective contact radii as low as about 20nm. There does not appear to be any other mention of flexoelectric properties of α -quartz in the literature.

2.6.2 Barium Titanate (BaTiO₃)

Barium titanate was the first ferroelectric perovskite to be discovered and has been used and studied extensively since the 1950's [75]. Favorable properties of BaTiO₃ include high electromechanical coupling factors, good chemical stability, and ease of manufacture [22]. As illustrated in Figure 19 [24], BaTiO₃ has paraelectric cubic perovskite structure (point group $m\bar{3}m$) above its curie temperature of 393K and is ferroelectric tetragonal (point group $4mm$) at room temperature [24]. This phase transformation involves elongation of one edge of the original cubic structure with shortening in the other two directions, resulting in $\langle 100 \rangle$ polar axes [24]. The polar axes arise due to homopolar contributions in the Ti-O bonds which favor an angled valency configuration and promote parallel orientation of polarization in neighboring lattice cells [74]. Phase changes to orthorhombic and rhombohedral phases also occur in BaTiO₃ when cooling through 278K and 183K, respectively [24].

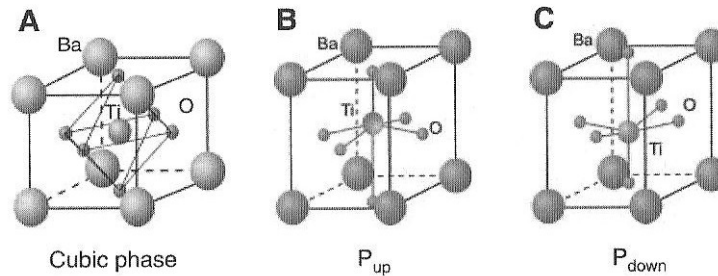


Figure 19. The perovskite structure of BaTiO₃ in its cubic and tetragonal phases

Regarding domains and dislocations, there are two forms of domains present in BaTiO₃ crystals: 90° domains (*a*-domains, where the polar axis is parallel to the crystal surface) and 180° domains (*c*-domains, where the polar axis is normal to the crystal surface). The most favorable room temperature slip system in BaTiO₃ is generally well

accepted as $\{110\} \langle 1\bar{1}0 \rangle$. Bradt and Ansell [81] have determined that dislocations may serve as nucleation sites for 90° domains and subsequently prevent their motion through strain interactions. Recent work [82] was unable to confirm any significant effects resulting from domain nucleation and/or switching due to dislocations initiated by pop-ins during indentation. Indentation size effects in BaTiO_3 [1,2,70,71] have been reviewed in Section 2.4.2. BaTiO_3 is known to exhibit a significant flexoelectric effect [1,2,13,83].

2.6.3 Lithium Niobate (LiNbO_3) and Lithium Tantalate (LiTaO_3)

Lithium niobate and lithium tantalate are both room temperature ferroelectrics most well known for their favorable nonlinear optical and electro-optic properties, making them useful in modulators, harmonic generators, and surface acoustic wave devices [74]. They may be readily manufactured as large optical quality single crystals by the Czochralski process [74]. As shown in Figure 20 [74], these materials have ABO_3 -type trigonal lattice structure (point group $R3m$) rather than the perovskite structure of BaTiO_3 [74].

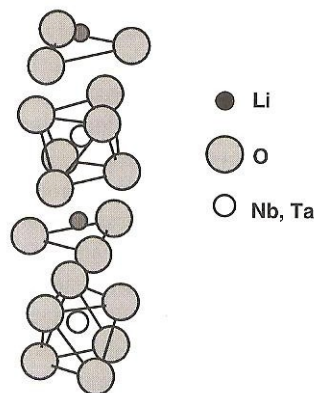


Figure 20. Trigonal structure of LiTaO_3 and LiNbO_3

There have been relatively few nanoindentation studies focusing on LiNbO₃ and LiTaO₃. Bhagavat and Kao [73] appear to have been the first to report on nanoindentation of LiNbO₃. They observed an indentation size effect, pop-ins, and hardness anisotropy (differing hardness values for the same indentation depth and displacement on opposing sides of the same crystal) in nanoindentation of X and Z-cut LiNbO₃ single crystals using a Berkovich indenter and loads up to 8000μN. Some pileup was observed but no cracking. Hardness reported for low loads (500μN) was significantly higher than for the highest loads for both crystal orientations, but hardness anisotropy was only significant in the X-cut crystal. Bhagavat and Kao [73] did not speculate on the mechanism behind this size effect. It is noteworthy that prior to the work of Bhagavat and Kao [73], Subhadra et al. [84] and references therein had observed load dependent hardness in LiNbO₃ by macro indentation tests, however these effects were thought to be artifacts of the analysis or test methods. Basu et al. [76] conducted spherical nanoindentation on LiNbO₃ and concluded that $(10\bar{1}2)[\bar{1}011]$ twins, the sizes of which depend on indenter radius, form during indentations after pop-ins. They argued that fully reversible incipient kink bands (IKBs, see Section 2.4.2) form within these twins and potentially interact with domains for enhanced energy dissipation. Anasori et al. [85] studied spherical nanoindentation of [0001] (Z-cut) LiTaO₃ single crystal to investigate ion irradiation effects. No change in material response was observed due to irradiation, and deformation involving twinning and IKB formation proved to behave similarly as seen in LiNbO₃ by Basu et al. [76].

It does not appear that there have been any experimental or theoretical investigations concerning flexoelectric properties of LiNbO₃ or LiTaO₃, however, they make good candidates for this study due to the availability of high quality crystals,

availability of information regarding their elastic, piezoelectric, and dielectric properties, and the observation of size effects in previous study.

2.6.4 Lead Magnesium Niobate – Lead Titanate $(1-x)(\text{Pb}(\text{Mg}_{1/3}\text{Nb}_{2/3})\text{O}_3)-x(\text{PbTiO}_3)$

Lead magnesium niobate – lead titanate, or PMN- x PT, crystals are solid solution relaxor based ferroelectrics with a morphotropic phase boundary (MPB) around $x \approx 34\%$ [86,87]. Below the MPB, PMN- x PT is rhombohedral (point group $3m$), while compositions above the MPB are tetragonal (point group $4mm$) [87]. The rhombohedral phase is sometimes treated as pseudo-cubic in the literature, with no apparent major consequences [87,88]. In both phases close to the MPB, dielectric and piezoelectric properties are highly enhanced. PMN- x PT crystals are seen as a potential replacement for piezoelectric ceramics in upcoming generations of ultrasonic devices and are the subject of much ongoing research to improve production methods and durability [87].

Some indentation testing of PMN- x PT has been reported. Microindentation has been used to investigate photoelastic effects [88], anisotropy of mechanical properties [89], and domain switching [90] in bulk samples, and it appears nanoindentation has been used mostly to evaluate PMN- x PT thin films [91,92]. Zhong et al. used nanoindentation with a Berkovich indenter to study mechanical properties of highly (100) orientated PMN-35PT films grown by pulsed laser deposition and compared the results to those for a commercially available PMN-PT single crystal. They found that elastic modulus and hardness of preferentially oriented films were comparable to those of the single crystal at about 126GPa and 6.5GPa, respectively, while polycrystalline and amorphous films suffered a reduction in both properties. No indentation size effects were reported, nor

were loads or displacements corresponding to the hardness and modulus measurements. Delobelle et al. [92] investigated mechanical property dependence on grain size in strongly (111) oriented sputtered PMN-30PT thin films with an average surface roughness of about 6nm using Berkovich nanoindentation and the CSM technique. A noticeable decrease in hardness was observed in the region of depths from initial penetration to 10-20% of film thickness, where substrate effects become significant. This behavior was not explicitly discussed in terms of being an indentation size effect.

In two studies [20,93] Hana et al. studied flexoelectric properties of ceramic PMN-10PT. In the earlier study [93], the inverse flexoelectric effect was utilized by inducing electric field gradients in conical bulk unpoled samples and measuring the resultant displacements. Around 298K, the flexoelectric coefficient μ_{33} was determined to be about $1000\mu\text{C}/\text{m}$, and $f_{33} \approx 4750\mu\text{C}/\text{m}$ was observed at approximately 257.5K, indicating an enormous flexoelectric effect in PMN-10PT. In the second study [20], Hana again studied conical bulk unpoled samples of PMT-10PT using the inverse flexoelectric effect as well as the direct effect. The results for flexoelectric coefficient f_{11} determined from the direct effect measurements were about two orders of magnitude smaller than those based on the inverse flexoelectric measurements, indicating that the huge flexoelectric behavior previously reported was most likely an artifact possibly due to surface effects or piezoelectric behavior induced by the high applied electric fields. Direct flexoelectric effect measurements yielded estimates of $f_{11} \approx 6$ to $12\mu\text{C}/\text{m}$.

Chapter 3 Experimental Methods

3.1 Materials and Sample Preparation

All crystal samples in this study were obtained commercially from two separate sources. Unpoled PMNT single crystals were purchased from TRS Technologies, Inc. (State College, PA) under the brand TRS-X2B with a stated nominal composition of 30% lead titanate. These crystals are cut with pseudo-cubic $\langle 001 \rangle$ orientation and dimensions of $5 \times 5 \times 0.345 \text{ mm}^3$ with one side background.

The background surface has an arithmetic average roughness (Ra) value greater than $1 \mu\text{m}$ and requires polishing prior to nanoindentation. A vibratory polisher (VibroMet I, Buehler Ltd., Lake Bluff, IL) with a custom free floating cylinder-in-sleeve type sample holder was used for this purpose. A schematic of the sample holder is provided in Figure 21. A series of progressively finer colloidal silica and diamond suspensions (down to 0.05 micron), in conjunction with low vibration intensity and a relatively light normal load (about 90g) applied to the sample, yields a surface of reasonably good quality for nanoindentation testing ($< 8 \text{ nm Ra}$). After final polishing, the crystal surface quality is confirmed by AFM.

All other single crystals were purchased from MTI Corporation (Richmond, CA). These materials include z-cut $\langle 0001 \rangle$ quartz ($10 \times 10 \times 0.5 \text{ mm}^3$), z-cut $\langle 0001 \rangle$ LiTaO_3 ($10 \times 10 \times 0.5 \text{ mm}^3$), z-cut $\langle 0001 \rangle$ LiNbO_3 ($5 \times 5 \times 0.5 \text{ mm}^3$), and poled $\langle 001 \rangle$ BaTiO_3 ($5 \times 5 \times 0.5 \text{ mm}^3$). All of these crystals were supplied with one or both sides polished and a surface roughness less than 1 nm Ra . Stiffness, piezoelectric, and dielectric properties listed in Table 5 were used in the present analysis.

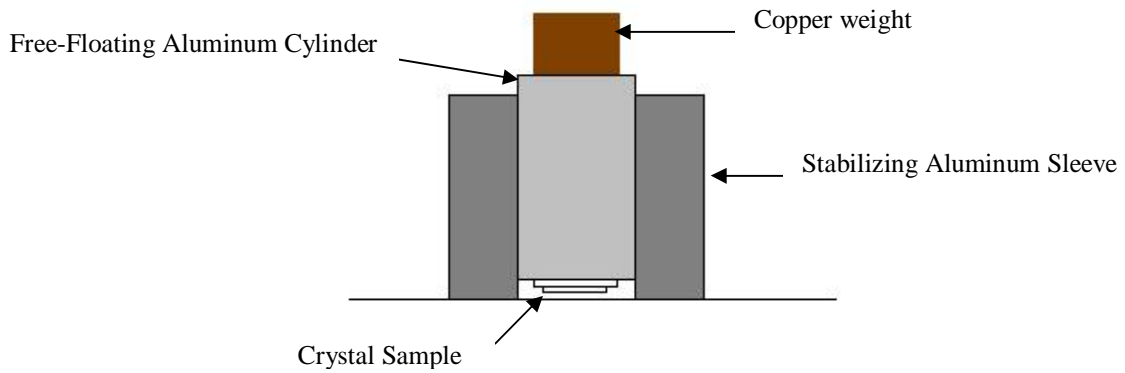


Figure 21. Cylinder-in-sleeve sample holder for crystals requiring vibratory polishing

Table 5. Material properties for use with the flexoelectric indentation model

Material	Stiffness Components (Gpa)					Piezoelectric Stress Constants (C/m ²)			Dielectric Constants (10 ⁻⁹ F/m)		Reference
	C ^E ₁₁	C ^E ₃₃	C ^E ₄₄	C ^E ₁₂	C ^E ₁₃	e ₃₁	e ₃₃	e ₁₅	a ^S ₁₁	a ^S ₃₃	
BaTiO₃	166	162	42.9	76.6	77.5	-4.4	18.6	11.6	11.1	12.5	2
PMN-29%PT crystal	124	108	63	111	104	-3.9	22.3	10.3	11.9	8.1	Manufacturer Datasheet
PMN-30%PT crystal	117	108	71	103	101	-2.4	27.1	13.6	29.3	11	94
LiNbO₃ crystal	203	242	59.5	57.3	75.2	0.23	1.33	3.76	0.392	0.247	95
LiTaO₃ crystal	230	280	96.8	44	81.2	-0.38	1.09	2.72	0.377	0.379	95
LiNbO₃ crystal	203	245	60	53	75	0.2	1.3	3.7	0.39	0.257	Warner in 95
LiTaO₃ crystal	233	275	94	47	80	0	1.9	2.6	0.368	0.38	Warner in 95

3.2 Instruments

3.2.1 Nanoindentation System

A Nano Indenter XP (MTS Nano Instruments, Oak Ridge, TN) CSM-capable nanoindentation system was used to characterize the piezoelectric single crystals. This system employs an electromagnetic coil for load control and a three plate capacitive displacement sensor in the manner illustrated schematically in Figure 22 [96]. Specifications for the system's (primary) XP head are provided in Figure 23. The Nano Indenter XP rests atop an air actuated vibration damping table within a padded isolation cabinet to minimize the influence of environmental factors that could negatively affect the operation of transducer components. The Nano Indenter XP is controlled by MTS TestWorks 4 software.

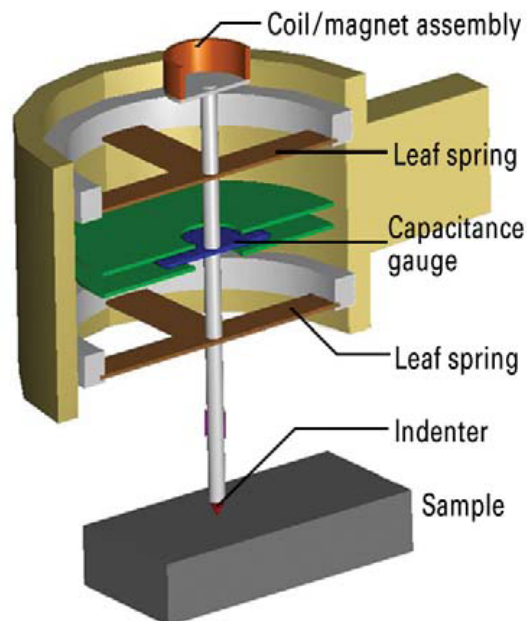


Figure 22. Schematic cross section of the Nano Indenter XP load-displacement head

Indentation Head Assembly	
Displacement resolution	<0.01 nm
Total indenter travel	2 mm
Maximum indentation depth	>500 μm
Load application	Coil / magnet assembly
Displacement measurement	Capacitance gauge
Loading capability	
Maximum load	500 mN (50.8 gm)
Maximum load with high-load option	1 kg
Load resolution	50 nN (5.1 μgm)
Load resolution with high-load option	50 nN (5.1 μgm)
Contact force	<1.0 μN
Load frame stiffness	$\approx 1 \times 10^7 \text{ N/m}$

Figure 23. Nano Indenter XP system specifications

Three diamond indenters with Berkovich, cone (45° centerline to face angle), and cube corner geometry were utilized with the Nano Indenter XP. The indenter area function coefficients for these tips, provided in Table 6, were carefully determined from a minimum of 25 indentations each into a standard fused silica sample ($E=72\text{GPa}$, $H=9\text{GPa}$, $\nu=0.18$). For convenience, a plot illustrating the relationship between indentation depth and effective contact radius for the three indenters has been provided in Figure 24.

Table 6. Indenter area coefficients determined for the three indenters in this study

Indenter	C₁	C₂	C₃	C₄	C₅
Berkovich	25.3016	699.429	-1171.67	1.32732	710.586
Cone	3.22183	2393.05	-8673.78	12476	-5316.41
Cube Corner	3.52409	106.198	793.374	596.906	-1334.69

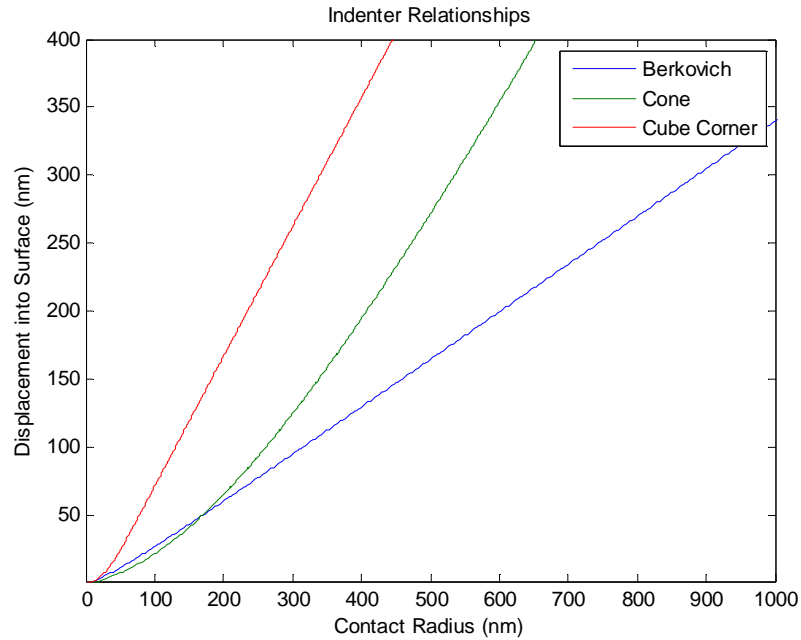


Figure 24. Contact radius-displacement relationships for the three indenters

3.2.2 Atomic Force Microscope

A commercial atomic force microscope (Dimension 3100-Nanoscope IV, Veeco Instruments, CA) was used to characterize the as-received and as-tested crystals. MikroMasch NSC15 aluminum backside cantilevers were used with the AFM in tapping mode to capture height and deflection data, which may be plotted for topographic analysis of the crystal surface. Deflection data essentially represents the derivative of the height data and tends to produce finer images due to enhanced surface edge sensitivity.

3.3 Procedures

To facilitate handling and minimize the risk of crystal damage between batches of tests, all crystal samples were affixed to stainless steel AFM sample disks using a very thin layer of epoxy (PMN-30PT only) or colloidal silver paste (all other samples). A small amount of colloidal silver paste was used to attach each sample disk to the standard

aluminum puck that connects to the nanoindenter stage for each batch of tests. This approach yields results that do not differ noticeably from those obtained when crystals are attached directly to the aluminum sample puck.

Tests were performed with each of the three indenters on the five subject crystals, yielding 15 batches of data with a minimum of 36 tests per batch. An individual test encompasses a surface find segment, loading at constant indentation strain rate (0.05s^{-1}) to an indentation depth of 400nm, partial unloading, and a constant load hold segment used for determining any thermal drift correction. Values for effective contact radius and harmonic contact stiffness normalized with respect to contact radius are determined continuously during the test. Following the batch testing, data was reviewed for accurate surface detection and exported to a spreadsheet. Representative residual indentations were imaged by tapping mode atomic force microscopy.

The above crystal data were used to determine the necessary piezoelectric and flexoelectric model parameters. Data from the first 34 tests in each Excel file was imported to a MATLAB workspace for analysis and plotting. Finally, a nonlinear least squares regression was used to fit the model Eqn. 62 to the Berkovich indentation data to estimate f_1^* , q_1 , and when necessary C_1^* . The end result is a total of five plots, one for each material, which show discretized data sets for the three indenters as well as the behavior of the piezoelectric and flexoelectric models.

Chapter 4 Experimental Results and Discussion

In this chapter results of the nanoindentation experiments and calculations leading to the estimation of flexoelectric properties for each material are presented and discussed. Advantages and disadvantages of the nanoindentation based flexoelectric property estimation methodology will be noted and explained throughout the chapter.

4.1 Quartz

Note again that quartz serves in this study as a benchmark material because it exhibits no obvious indentation size effects for contact radii as low as about 20nm, and its ratio of contact stiffness to contact radius during indentation is thus adequately described as a linear (constant) function of contact radius [1,2]. One significant point which was not emphasized in previous work is that the piezoelectric indentation model developed by Karapetian et al. [77] does not appear applicable to quartz. Specifically, the composite material property C_1^* (Refer to Section 2.5.1, Eqn. 36) may not be computed for quartz because the three piezoelectric stress constants involved (d_{15} , d_{31} , d_{33}) are identically zero for point group 32 [21]. The null values result in division and multiplication by zero at various steps throughout the calculation for C_1^* , and thus C_1^* turns out undefined. The current quartz data will be comparable only to the previous data and not an analytically predicted value.

Atomic force micrographs of the residual Berkovich, cone, and cube corner indentations in the z-cut quartz crystal are shown in Figure 25. These micrographs depict deflection data which effectively represents the derivative of height as the AFM probe

scans over the sample, resulting in finer image detail. There is no apparent or significant cracking that has occurred during indentation. Cracking is undesirable since it complicates the stress field surrounding the indentation and violates many of the assumptions involved in the piezoelectric and flexoelectric models.

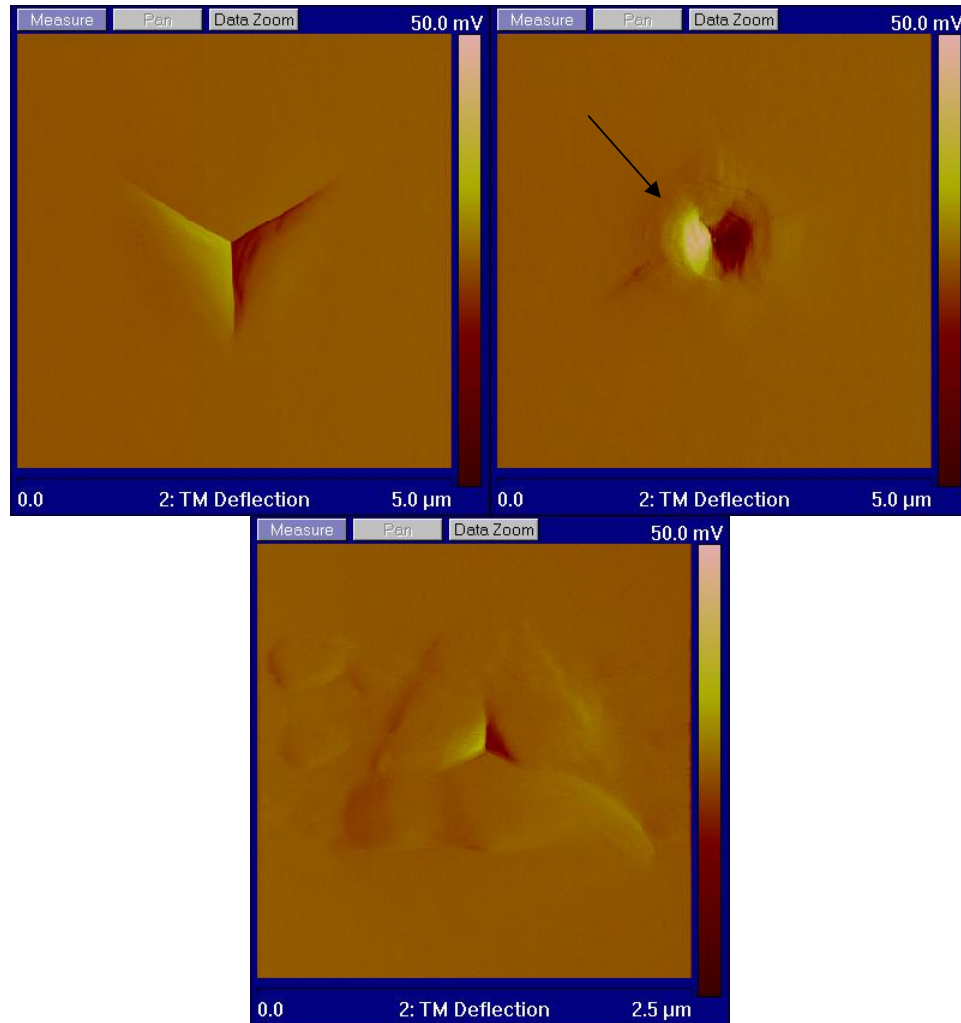


Figure 25. AFM micrographs for quartz indentations

Quartz exhibits a small degree of mounding around the indenters. This effect is very slight for the case of the Berkovich indenter, more obvious with the cone indenter (as evidenced by the dark semicircular band on the left side of the indentation and indicated by an arrow), and obvious for the cube corner indenter. Based on AFM height

data shown in Figure 26, the mounding height for the Berkovich impression is about 12nm, and the residual indentation depth is about 110nm. The cross section in this figure was taken along one of the lines in the micrograph corresponding to the intersection of two of the Berkovich indenter faces. Height data cross sections for the remaining crystals also have this orientation. The scope of this study limits analysis of the effects of mounding during indentation to mostly qualitative assessments, but Appendix B includes some quantitative discussion regarding the Berkovich indenter here. Mounding issues will be addressed primarily in terms of the stiffness plots in the following sections.



Figure 26. Cross section view of a Berkovich indentation in quartz

The results of the nanoindentation experiments for z-cut quartz are shown in Figure 27. Three separate data sets are shown for the three indenters, and the error bars represent one standard deviation for each data point. For all indenters, the error bars shrink with increasing contact radius, and hence indentation depth, as expected. Measurements in the extremely small scale where contact radii are in the tens of nanometers are relatively noisy compared to those at deeper contact radii when using the CSM technique due to the oscillatory loading. For a given target harmonic displacement, two nanometers in the present case, the oscillatory displacements are a smaller fraction of

the total indentation depth for deeper indentations. The result is less sensitivity in the calculations involving the indenter area function and leading to the determination of stiffness, contact radius, etc., and so measurements tend to have less variation as the indentation proceeds.

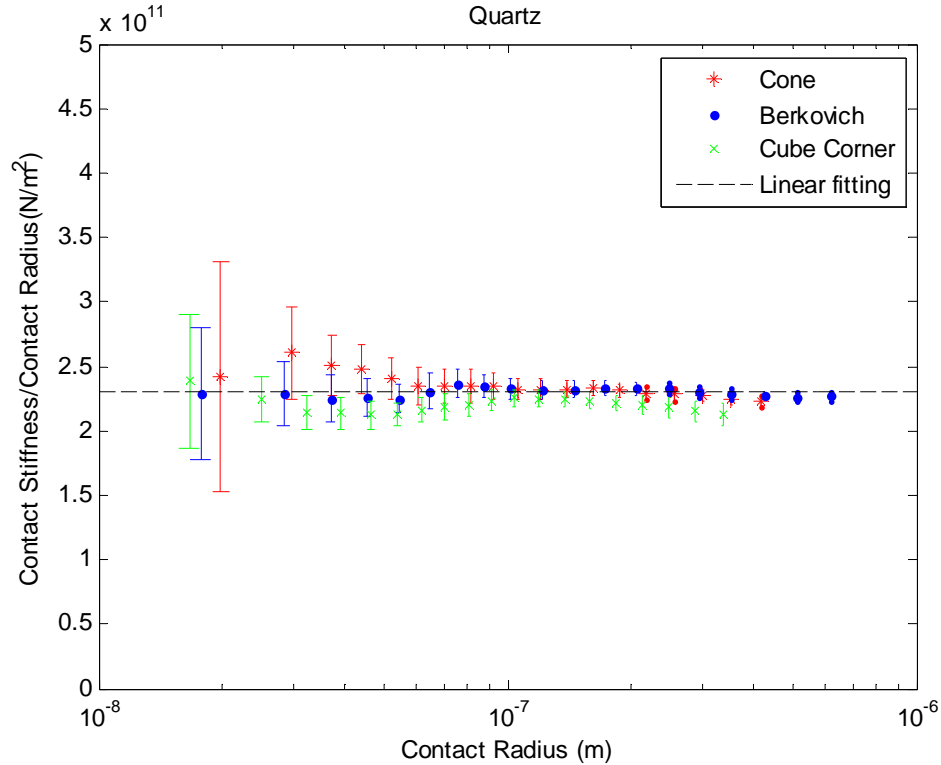


Figure 27. Indentation results for quartz

The response of the material to the three indenters will be examined in turn beginning with the Berkovich indenter. The data for the Berkovich indenter is quite well behaved and clearly suggests no real size dependency in the stiffness. There is some waviness in the data points that is inconsequential with regard to size dependency of the stiffness but could be recognized as a potential effect of mounding. As the indentation proceeds and mounding occurs, the contact area is slightly underestimated [35]. That is, the load is in fact distributed over a larger contact area than the indenter area function

would indicate for a given indentation depth. This underestimation of actual contact area leads to overestimation of the normalized stiffness in the plot and could explain why stiffness appears to increase for contact radii in the range of about 50nm to 70nm. It is noteworthy that this behavior seems a little more pronounced in the data for the cube corner indentation. Indentations by sharp indenters such as the cube corner tend to follow the slip line harness model where the displaced volume of plastically deformed material often flows upward around the indenter [35]. The slight recurve in the middle of the cube corner data seems understandable in terms of the expectation of enhanced mounding with sharp indenters.

The cone indentation data is the only data set that indicates any possibility of size dependent stiffness, however, this is likely an artifact. In the range of contact radii from about 20nm to 60nm it appears that the average normalized stiffness increases sharply and tends back downward. The first data point agrees with those for the Berkovich and cube corner indenters, albeit with much larger error bars which may be attributed to the increased sensitivity of the indenter area function for the cone at extremely small depths. The following several data points indicate some downward trend in the stiffness, but this trend is not observed with the other indenters. Given the size of the error bars for all the indenters at these contact radii (about 30nm to 50nm), the cone data is not unreasonable, but the downward trend potentially indicates of some inaccuracy in the area indenter function. Cone indenters are notoriously difficult to manufacture, maintain, and calibrate for small scale measurements [43,97], so this is not a particularly alarming result, and it does not affect the overall conclusions about the behavior of quartz during indentation.

The two most important observations regarding the quartz indentation data are that (i.) there is no appreciable indentation size effect within the range of contact radii tested, and (ii.) the ratio of contact stiffness to contact radius measured here matches that determined by Gharbi et al. [1] (about $2.35 \times 10^{11} \text{N/m}^2$). Both of these results are in excellent agreement with the previous work, particularly for the Berkovich indentation, and demonstrate that the experimental approach and methods are valid.

4.2 Lithium Niobate (LiNbO₃)

Representative atomic force micrographs of the residual Berkovich, cone, and cube corner indentations in the z-cut LiNbO₃ crystal are shown in Figure 28. For the Berkovich case, the residual indentation closely resembles that seen for z-cut quartz with a higher degree of mounding. Based on AMF height data shown in Figure 29, the Berkovich impression has a mounding height of about 37nm and a residual indentation depth of about 150nm. The Berkovich indentation micrograph here compares well with one produced by Bhagavat and Kao [73]. The conical and cube corner indentations are a bit peculiar compared to those observed in quartz. For the cone indenter, while there does not appear to be gross fracture at the surface, the center of the impression lacks some of the expected rotational symmetry. For the cube corner indenter, it appears that the residual impression does not sit below the surface of the rest of the crystal. A possible explanation could be that during unloading the indenter has pulled out some of the plastically deformed material. This would seem possible though only if some sub surface cracking had occurred beneath the indenter. No AFM micrographs of cone or cube corner nanoindentation of LiNbO₃ appear to be available in the literature for comparison. Given the scope of the present work and the relatively small body of literature concerning

indentation of LiNbO_3 , there is little that can confidently be said to explain the physical origins of the topography of the residual cone and cube corner impressions. These results highlight a need for increased study of LiNbO_3 mechanical behavior.

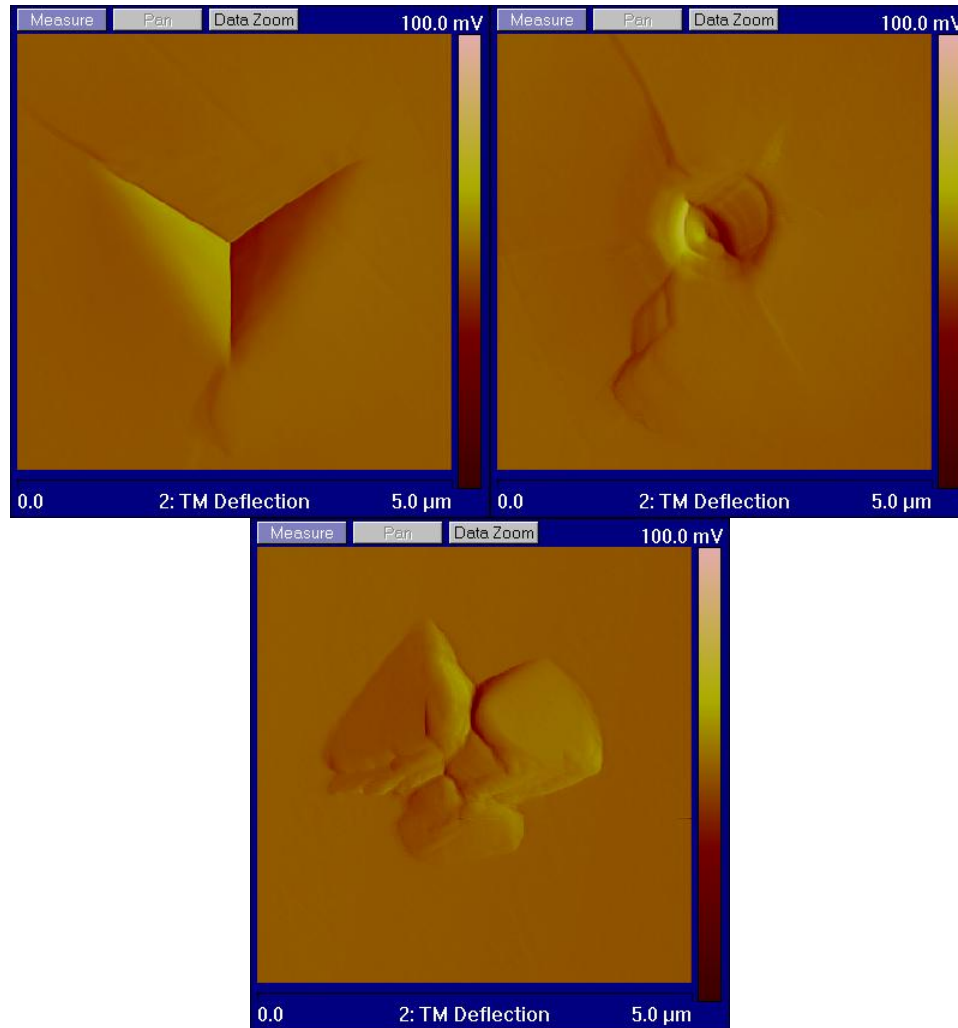


Figure 28. AFM micrographs for LiNbO_3 indentations

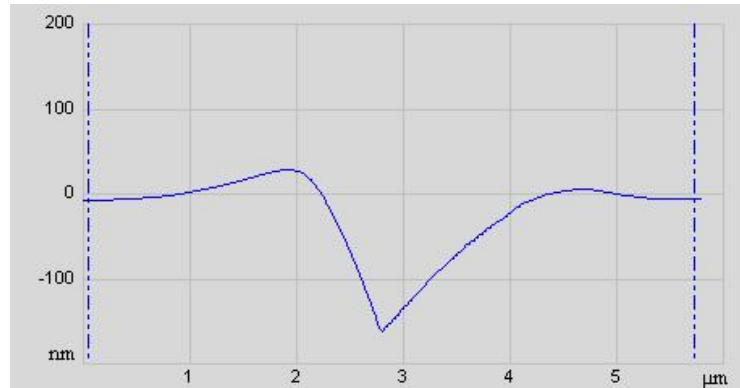


Figure 29. Cross section view of a Berkovich indentation in LiNbO₃

The results of the nanoindentation experiments for z-cut LiNbO₃ are shown in Figure 30. Again, three separate data sets are shown for the three indenters, and the error bars represent one standard deviation for each data point. Comments regarding the error bar behavior and slight fluctuations observed in the data sets that were presented for quartz are applicable here as well. In general, these observations are thought to hold for all remaining crystals unless otherwise stated. The experimental data itself will be taken into consideration first, followed by discussion of the piezoelectric and flexoelectric models.

It is immediately obvious from Figure 30 that LiNbO₃ exhibits a size effect during nanoindentation. The ratio of contact stiffness to contact radius increases with decreasing contact radius for all three indenters. With the Berkovich indenter, size dependency is evident for contact radii less than about 60nm. The cone data shows decreasing normalized stiffness values out to slightly larger contact radii, and again the second data point is higher than the first. This anomaly is still thought to indicate a problematic area function in the extreme small scale. For the case of cube corner indentation, the size effect is still present but less pronounced; only the first data point appears to indicate

greater stiffness than the others. This is noteworthy when taking into consideration again that the cube corner indenter is the sharpest of the three in this study and tends to “cut” into the sample during testing. With this cutting action there is less of a compressive stress field under the indenter than for Berkovich or cone geometries, and so upward material deformation is less constrained. With less constraint on the upward flow of material, the strain gradients ought to be somewhat lower and thus less of a size effect may be observed due to flexoelectricity.

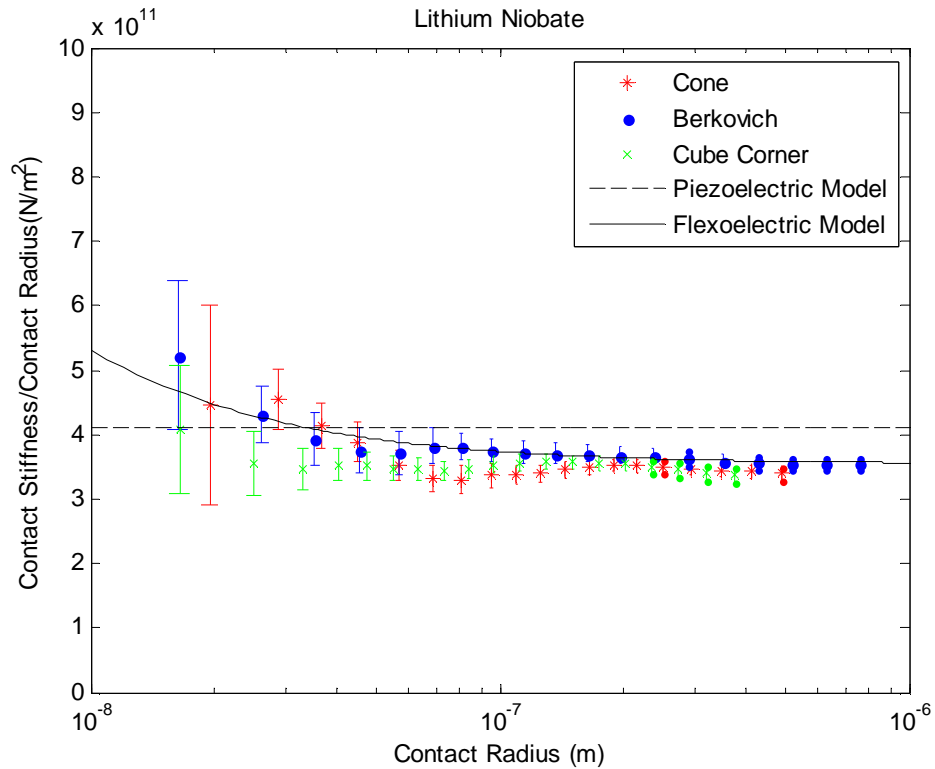


Figure 30. Indentation results for LiNbO_3

It is important to recall the reasoning behind the shape of the observed size effect seen in BaTiO_3 (Section 2.5.3), here with LiNbO_3 , and in the crystals to come. For very shallow indentations, and hence smaller contact radii, the strain gradients present beneath the indenter are quite high. For materials possessing sufficiently large flexoelectric

properties, there is a flexoelectric contribution to the overall material stiffness that presents itself in an obvious manner only in the presence of very high strain gradients. As the indenter is driven deeper into the surface of the material, elastic strain gradients tend to diminish as a relative part of the total deformation and flexoelectric effects therefore diminish as a portion of the overall stiffness. Once contact radii are large enough, the flexoelectric contribution to the total stiffness becomes small compared to the contributions due to elastic and piezoelectric effects. At this point the stiffness no longer depends strongly on the contact radius and the slope of the normalized stiffness versus contact radius plot approaches zero. Keeping these principles in mind, the differences between the stiffness plots for quartz and those here for LiNbO₃ may be attributed to flexoelectricity. For the same indenters and range of contact radii, quartz shows no size dependent stiffening while LiNbO₃ does, implying that the flexoelectric properties of LiNbO₃ are greater than those of quartz. The indentation models now come into the picture as tools to help determine the magnitude of the flexoelectric properties.

The piezoelectric-only indentation model must first be considered alone. Karapetian et al. [77] report a piezoelectric indentation coupling constant C_1^* of $6.47 \times 10^{11} N/m^2$ for LiNbO₃. For piezoelectric only indentation (ignoring any flexoelectric effects) the ratio of contact stiffness to contact radius is given simply by

$$\frac{s}{a} = \frac{2}{\pi} C_1^* = 4.12 \times 10^{11} N/m^2.$$

This is the value indicated by the dashed line plotted in Figure 30 for the piezoelectric model. For the larger contact radii where flexoelectric stiffness contributions are anticipated to be small, the piezoelectric model is expected to accurately describe the

stiffness of the contact, but this is clearly not the case in the plot. The actual stiffness response of the LiNbO_3 crystal is less than the piezoelectric model predicts. The reason for this discrepancy is unknown, but there is no reason to believe it is an artifact of the testing methods. In the literature review for the present work, no investigations could be located in which Karapetian et al.'s [77] piezoelectric indentation model was compared directly with experimentally obtained stiffness data for any piezoelectric crystal.

Some consideration was given to the idea that C_1^* calculated with different sets of material constants may offer a better fit between the model and experimental data. Elastic, piezoelectric, and dielectric constants for LiNbO_3 as determined by Warner et al. and Smith and Welsh in Ref. [95] were used to calculate new values of $C_1^* = 6.67 \times 10^{11} \text{ N/m}^2$ and $C_1^* = 6.61 \times 10^{11} \text{ N/m}^2$, respectively. Both of these values however are larger than the C_1^* reported for LiNbO_3 by Karapetian et al. [77], and so they predict a ratio of contact stiffness to contact radius even higher than that shown in Figure 30. With no apparent previous confirmation between the model and experimental data available in the literature, and with no basis for critique of the derivation of the analytical indentation model, it is difficult to assess the full meaning of the discrepancy between observed and predicted normalized stiffness for large contact radii. For now, it is tentatively concluded that the origin of the discrepancy lies within the determination of the very complicated piezoelectric indentation coupling constant C_1^* .

Recall that for piezoelectric indentation incorporating flexoelectricity, the model predicts that the ratio of contact stiffness to contact radius may be expressed by

$$\frac{s}{a} = \frac{2}{\pi} C_1^* - \frac{2f_1^*}{\pi a^2} \frac{\varepsilon_1}{(A^i)^2} (\varepsilon_1 e^{-\frac{A^i}{\varepsilon_1} a} - \varepsilon_1 + A^i a) \quad \text{Eqn. 65}$$

where A^i is a constant dependent upon material properties and ε_1 is the ratio of the order of magnitude of the flexoelectric properties f_{ij} to the average of the piezoelectric properties d^* . Based on Warner et al.'s data for LiNbO₃ in Ref. [95], $A^i = 6.4628$ and $d^* = 1.7333C/m^2$. Gharbi et al. estimated f_1^* based on numerical calculations in their work, and ε_1 allows for curve fitting. In the present work however, f_1^* is used as an additional fit parameter. While the numerical route is more formal, it greatly compromises the simplicity in estimating flexoelectric properties via nanoindentation while offering apparently little in the way of enhanced accuracy. Consider the effect of f_1^* based on its location in Eqn. 65 and its approximate magnitude of $-1 \times 10^{12} N/m^2$. The term f_1^* determines essentially how stiff the crystal may behave when flexoelectricity is taken into consideration, but based on its definition (see Eqn. 56), it does not affect the outcome of the flexoelectric estimate f_{ij} , which depends entirely on ε_1 . Graphically, increasing or decreasing the magnitude of f_1^* raises and lowers the ordinate values on the normalized stiffness plots at very small contact radii. Increasing or decreasing ε_1 on the other hand pushes the size effect out to larger contact radii or causes the size dependency to diminish at smaller contact radii, respectively. So, every set of (f_1^*, ε_1) produces a unique stiffness plot based on Eqn. 65 where the flexoelectric property estimation depends essentially on ε_1 alone. Based on these observations there

do not appear to be any sufficiently compelling arguments against the use of f_1^* as a fit parameter.

Before presenting the flexoelectric estimate f_{ij} for LiNbO₃, it must be noted that for the present case C_1^* must also be used as a fitting parameter. As previously mentioned, Eqn. 65 drives the stiffness to a constant value depending only on C_1^* for large contact radii. If C_1^* were fixed during the fitting procedure to one of the three values in the proceeding paragraphs, which predict higher stiffness than is actually observed for the larger contact radii, the overall fit would be very poor and the resultant f_{ij} would be practically meaningless. Relaxing the constraint on C_1^* enhances convergence and the quality of the fit. Considering that the preciseness of C_1^* for predicting size independent stiffness has not been fully established, this approach is reasonable.

The results of the fitting of Eqn. 65 to the Berkovich indentation data for LiNbO₃ are provided in Table 7. Note that ε_1 , f_1^* , and C_1^* are all determined by fitting and f_{ij} is subsequently determined from ε_1 . Flexoelectric estimates for LiNbO₃ and all remaining materials are based on the Berkovich indentation data alone for two primary reasons. First, although it lacks a well defined contact radius, the Berkovich indenter most closely approximates the flat punch assumed in the model. The cone indenter here has a 45° face to centerline angle and is therefore somewhat sharp compared to the Berkovich indenter with an effective cone angle of about 70.3°. The cube corner indenter is the greatest departure from a flat punch. The second reason for basing the flexoelectric estimations on the Berkovich data alone is that unfortunately the data obtained with the cone indenter is

not well behaved in the small extremely small scale. This raises some questions as to the accuracy of the indenter area function and makes fitting more difficult.

Table 7. Flexoelectric estimation results for LiNbO₃

C_1^*	f_1^*	ε_1	f_{ij}
$5.57 \times 10^{11} \text{ N/m}^2$	$-3.35 \times 10^{12} \text{ N/m}^2$	$5.891 \times 10^{-9} \text{ m}$	$1.0 \times 10^{-8} \text{ C/m}$

The quantities provided in Table 7 are precisely those which yield the flexoelectric model plot for LiNbO₃ shown in Figure 30. As seen in the figure, the model fits the Berkovich data points quite well overall. Note that each that each data point is weighted by one over the square of its standard deviation for the fitting, so data points with smaller error bars are weighted higher than those with large error bars. This weighing scheme is utilized for all other fitting in this work as well. All of the fitting results for LiNbO₃ are reasonable. The value for C_1^* , as expected, is just somewhat smaller than predicted by the analytical piezoelectric model. The magnitude of f_1^* is within the range of values one may expect based on the value reported [2] for BaTiO₃ ($-9 \times 10^{11} \text{ N/m}^2$). Finally, the grand prize of the fitting procedure is ε_1 , which allows for the estimation of the strength of the flexoelectric properties of LiNbO₃: $f_{ij}^{\text{LiNbO}_3} \approx 1.0 \times 10^{-8} \text{ C/m}$. At the time of this writing there do not appear to be any prior experimental or first-principles derived estimations of flexoelectric properties for LiNbO₃ to which this estimate may be compared.

There are, however, several ways that the result for $f_{ij}^{\text{LiNbO}_3}$ may be qualitatively assessed. First consider whether the value lies within reasonable upper and lower bounds.

Kogan's [31] phenomenological estimation $f \approx e/a$ puts a lower limit on the flexoelectric properties for LiNbO_3 around $3 \times 10^{-10} \text{ C/m}$. On the other hand, it is safe to assume that LiNbO_3 is less strongly flexoelectric than BaTiO_3 , for which bending experiments indicate $f_{12}^{\text{BaTiO}_3} \approx 10^{-5} \text{ C/m}$. The present estimate for LiNbO_3 fits neatly between these bounds numerically as well as graphically. Consider the normalized stiffness versus contact radius plots for quartz, LiNbO_3 , and BaTiO_3 . The size effect observed in the data for LiNbO_3 is less severe than with BaTiO_3 (see Figure 18), a material considered strongly flexoelectric, but obviously presents itself, which is not the case for presumably weakly flexoelectric quartz. Kogan's [31] phenomenological estimation $f \approx e/a$ predicts $f \approx 3 \times 10^{-10} \text{ C/m}$ for quartz.

Another interesting way to assess $f_{ij}^{\text{LiNbO}_3}$ is to compare the behavior of the data for LiNbO_3 in Figure 30 with data obtained from another material already known to possess flexoelectric properties on the order of $1.0 \times 10^{-8} \text{ C/m}$. It turns out that SrTiO_3 makes a great candidate for this purpose. Zubko et al. [14] have completely characterized the flexoelectric tensor for paraelectric (cubic point group $m3m$) SrTiO_3 by bending experiments and determined that all components are on the order of $10^{-9} - 10^{-8} \text{ C/m}$. The exact same nanoindentation procedure employed to obtain the Berkovich data in Figure 30 for LiNbO_3 was used to perform tests on a (001) oriented SrTiO_3 single crystal, yielding the data presented in Figure 31.

by derivation (265GPa). The SrTiO₃ (001) orientation was confirmed by X-ray diffraction, and these results are in Appendix C.

At this juncture an important matter of discussion arises. Even with no possibility of applying the flexoelectric indentation model as it currently stands to the data for SrTiO₃, the behavior of the data alone implies moderate flexoelectric behavior. So, while producing a quantitative estimate of f_{ij} based on indentation data necessitates some analytical investment, experimental data alone can provide some idea as to the potential magnitude of f_{ij} for a given material, e.g., SrTiO₃ is more flexoelectric than quartz but less flexoelectric than BaTiO₃. In this sense, nanoindentation could be used rather simply as a means to select candidate materials for more in-depth flexoelectric investigations involving flexure tests, inverse effects, and so on.

4.3 Lithium Tantalate (LiTaO₃)

Given the structural and electronic similarities between LiTaO₃ and LiNbO₃, it comes as little surprise that much of the results and discussion for LiNbO₃ in the previous section apply quite well for LiTaO₃. There are some interesting differences however which will be presented and discussed here.

Representative atomic force micrographs of the residual Berkovich, cone, and cube corner indentations in the z-cut LiTaO₃ crystal are shown in Figure 32. For the Berkovich case, the residual indentation closely resembles that seen for z-cut LiNbO₃ but with an obvious and higher degree of mounding. Based on AMF height data shown in Figure 33, the Berkovich impression has a mounding height of about 54nm and a residual indentation depth of about 50nm.

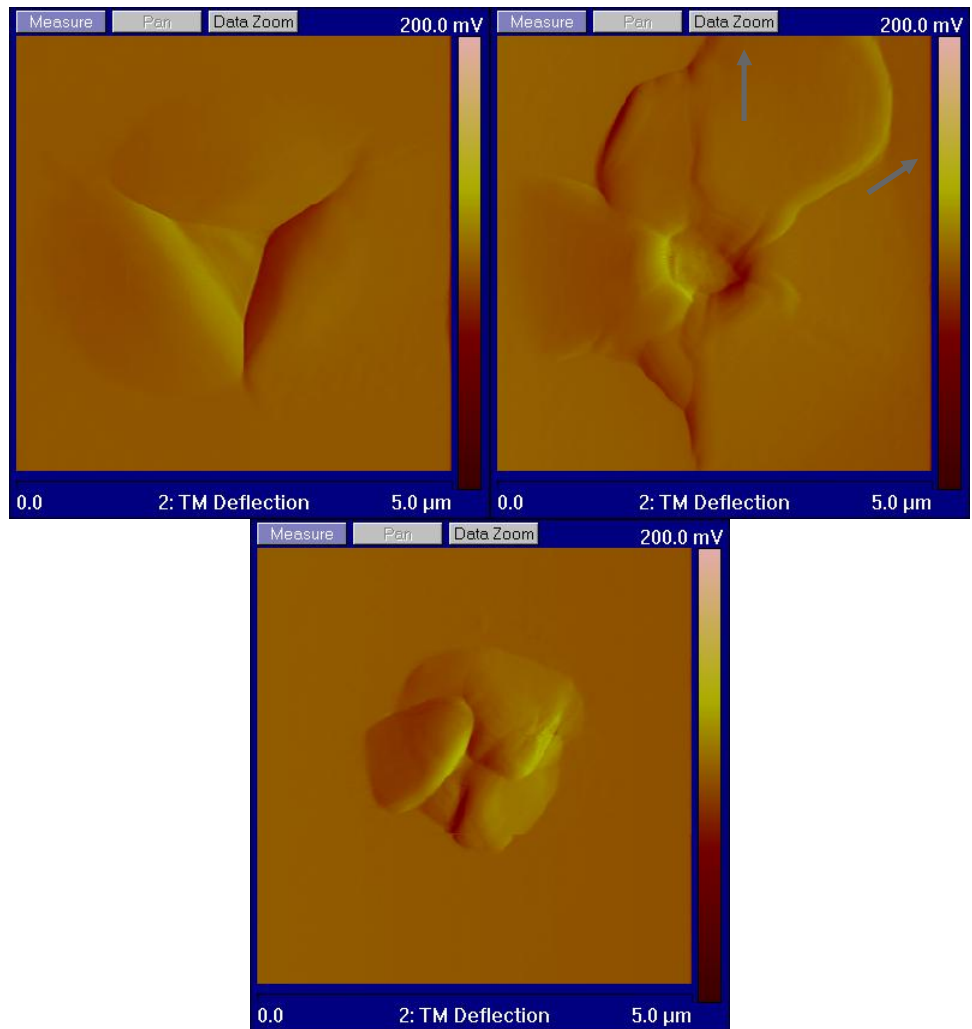


Figure 32. AFM micrographs for LiTaO₃

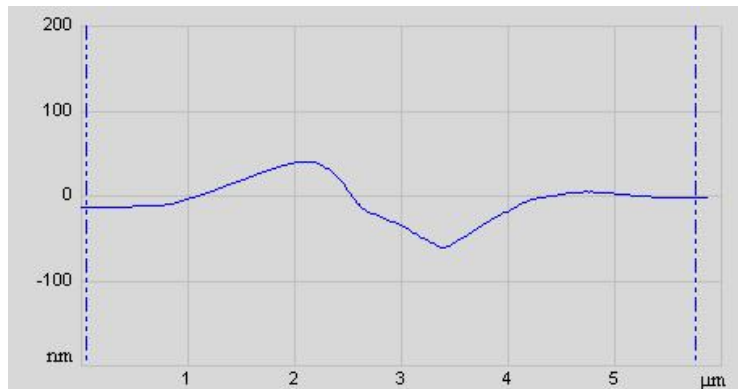


Figure 33. Cross section view of a Berkovich indentation in LiTaO₃

The micrograph for the conical indenter is quite a departure from those seen with quartz and LiNbO_3 . Again, fracture is not obvious, but it does not seem as though the blistered appearance of the surface around the residual impression could be due to simple mounding. Dislocation activity is an obvious matter of interest, and it is interesting to see that the elevated region in the top right corner of the micrograph has well defined borders which coincide with projections of the trigonal lattice vectors. Light grey arrows have been added in the micrograph to draw attention to this feature. Anasori et al. [85] have produced scanning electron micrographs of residual indents in LiTaO_3 produced by a spherical (radius = $1.4\mu\text{m}$) indenter loaded to 20mN, but it is not obvious whether their crystal has a blistered appearance as seen here. The cube corner indentation micrograph resembles that seen with LiNbO_3 , and the same discussion applies. As with LiNbO_3 , the scope of the present work along with the relatively small body of literature concerning fracture, indentation, and dislocation behavior in LiTaO_3 limits detailed discussion of the indentation micrographs while highlighting the need for further investigation.

The results of the nanoindentation experiments for z-cut LiTaO_3 are shown in Figure 34. Looking at the Berkovich data alone, there is a great resemblance to the results of both LiNbO_3 and SrTiO_3 . For all indenters the size effect is obviously present, and the general behavior of all the data sets follows the same observations as with LiNbO_3 . The degree of fluctuation in the data for contact radii greater than about 70nm appears slightly more pronounced than with LiNbO_3 , but it is also commensurate with the greater degree of mounding observed in the LiTaO_3 AFM micrographs.

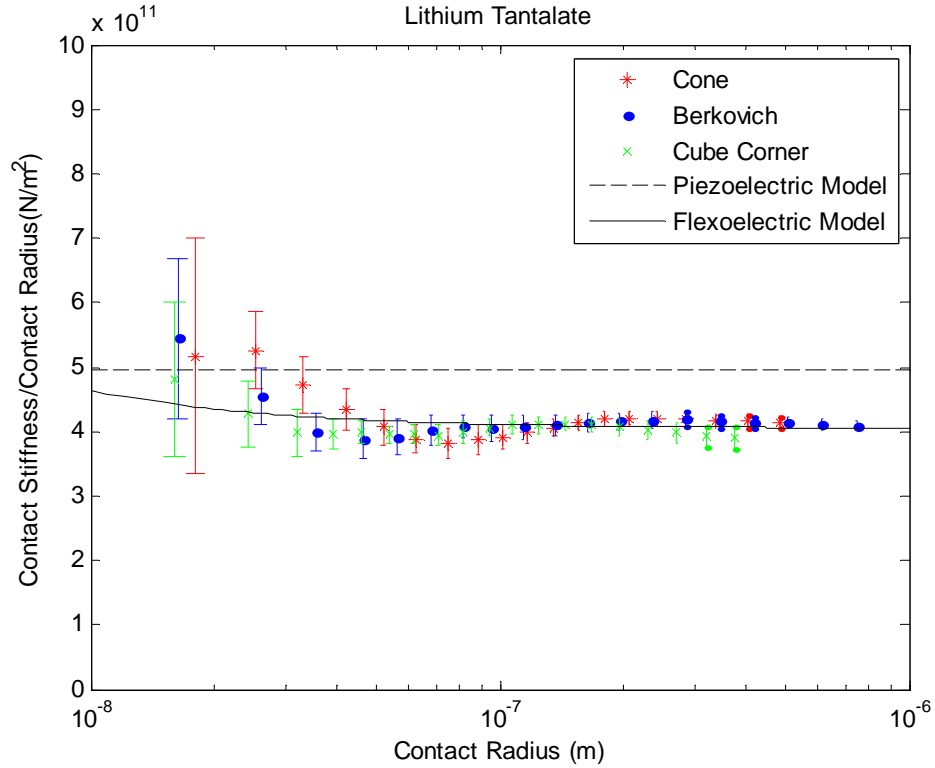


Figure 34. Indentation results for LiTaO_3

Karapetian et al. [77] report a piezoelectric indentation coupling constant C_1^* of $7.80 \times 10^{11} \text{ N/m}^2$ for LiTaO_3 . This yields a predicted constant ratio of contact stiffness to contact radius of $4.97 \times 10^{11} \text{ N/m}^2$ as indicated by the dashed line plotted in Figure 34 for the piezoelectric model. Exactly as with LiNbO_3 , the actual stiffness response of the LiTaO_3 crystal is less than the piezoelectric model predicts. Elastic, piezoelectric, and dielectric constants for LiTaO_3 as determined by Warner et al. and Smith and Welsh in Ref. [95] were used to calculate new values of $C_1^* = 7.83 \times 10^{11} \text{ N/m}^2$ and $C_1^* = 8.04 \times 10^{11} \text{ N/m}^2$, respectively, but again these overestimate the predicted stiffness response. For the same reasons and in the same manner discussed with LiNbO_3 , C_1^* must be used as a fitting parameter for the flexoelectric model.

Based on Warner et al.'s data for LiTaO₃ in Ref. [95], the required constant terms for application of the flexoelectric model are $A^i = 6.7495$ and $d^* = 1.5C/m^2$. The results of the fitting of Eqn. 65 to the Berkovich indentation data for LiTaO₃ are provided in Table 8. These fit parameters yield the flexoelectric model plot for LiTaO₃ shown in Figure 34.

Table 8. Flexoelectric estimation results for LiTaO₃

C_1^*	f_1^*	ϵ_1	f_{ij}
$6.36 \times 10^{11} N/m^2$	$-4.16 \times 10^{12} N/m^2$	$1.54 \times 10^{-9} m$	$2.3 \times 10^{-9} C/m$

The final result $f_{ij}^{LiTaO_3} \approx 2.3 \times 10^{-9} C/m$ is perfectly reasonable taking into consideration the similarity between the data for LiTaO₃, LiNbO₃, and SrTiO₃ and the underlying assumptions and limitations of the flexoelectric model. However, the fit between the model and the Berkovich data for LiTaO₃ in Figure 34 is clearly not as favorable as was achieved for LiNbO₃. There are two major contributing factors to this issue. The first of these lies in the data itself. As the effective contact radius increases during indentation from about 50nm to 300nm, the ratio of contact stiffness to contact radius appears to increase or recurve slightly. Due to the manner in which mounding leads to some underestimation of true contact area (and hence overestimation of stiffness and underestimation of effective contact radius as discussed in Sections 2.3.5 and 4.1), and given the degree of mounding visible in the LiTaO₃ AFM micrographs, it is most likely that the recurve is an artifact. The nature of the flexoelectric model is such that regardless of whether the recurve is an artifact or true material response, it is not predictable. Under no circumstances would the model predict increases in normalized

stiffness with increases in contact radius. Since the recurve in the LiTaO₃ Berkovich data is more pronounced than with LiTaO₃ and the flexoelectric model cannot account for such behavior, the three parameter curve fit has more difficulty converging.

A second, but likely less influential issue regarding the quality of the curve fit concerns the ability of the flexoelectric model to accurately capture the shape of the data in the extremely small scale. Gharbi et al. [2] note that for contact radii smaller than about 100nm ignoring higher order terms as was done in the derivation of Eqn. 65 can affect the results and assumptions regarding perturbation theory may become questionable. In its present form, the flexoelectric indentation model may not be capable of exactly replicating the trend in the LiTaO₃ data for the contact radii where the size effect is observed (less than about 40nm).

Despite these concerns, it is noteworthy that the flexoelectric model generally falls within the error bars (one standard deviation) for both the LiNbO₃ and LiTaO₃ Berkovich data sets. Additionally, the f_{ij} estimates in both cases are reasonable within the expected limits. To demonstrate that a better apparent fit of the flexoelectric model to the data does not necessarily result in a better estimate of f_{ij} , consider Figure 35. The only difference between this plot and Figure 34 is that the model parameters f_1^* and ε_1 have been intentionally chosen with less restriction so that the flexoelectric model curve better matches the two leftmost data points. The fit values here are $f_1^* \approx -5.1 \times 10^{16} \text{ N/m}^2$ and $\varepsilon_1 \approx 4.2 \times 10^{-13} \text{ m}$ which yield the clearly erroneous flexoelectric estimate $f_{ij}^{LiTaO_3} \approx 6.3 \times 10^{-13} \text{ C/m}$. This value is more than two orders of magnitude smaller than predicted by the rudimentary phenomenological estimation

$f \approx e/a$. The fit parameters necessary to achieve the flexoelectric model curve in Figure 35 highlight the need for appropriate bounds and initial guesses during the fit procedure. At first glance the flexoelectric plot may look acceptable, but the overall fit is poor and the resultant f_{ij} is unreasonably small.

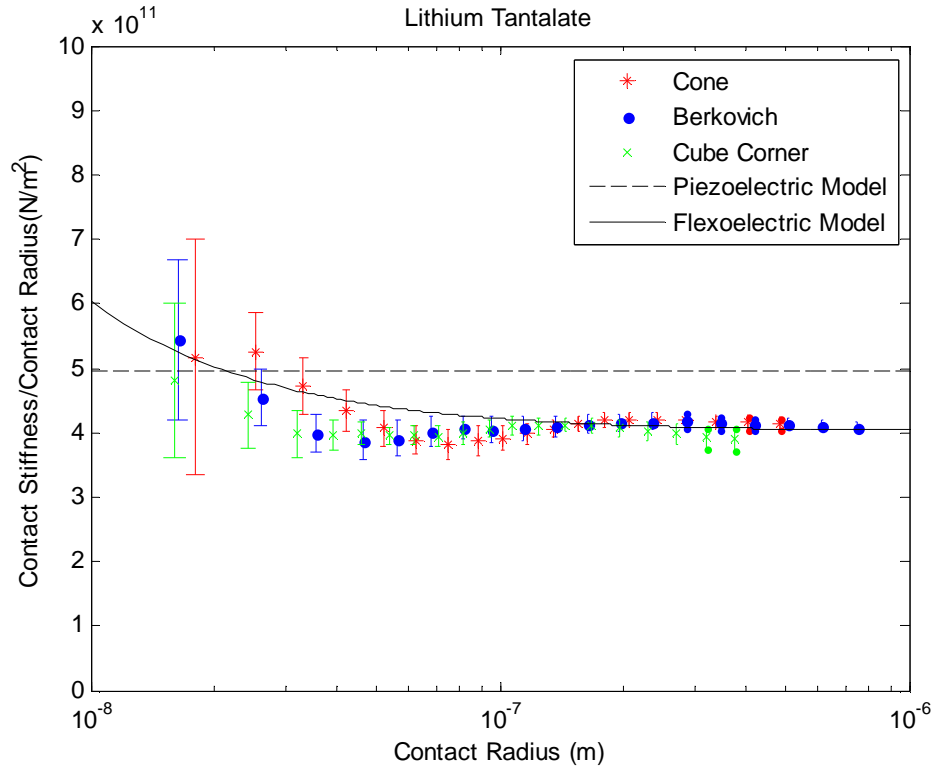


Figure 35. Demonstration of the influence of erroneous flexoelectric model parameters

4.4 Lead Magnesium Niobate – Lead Titanate (PMN-PT)

The lead magnesium niobate – lead titanate crystal discussed here has a nominal 30% lead titanate composition and will be referred to as PMN-30%PT. The analysis to follow uses both material properties for 29%PT (measured by the supplier) and 30%PT (available in the open literature [94]) compositions to demonstrate sensitivity of the results.

Representative atomic force micrographs of the residual Berkovich, cone, and cube corner indentations in the (001) PMN-30%PT crystal are shown in Figure 36. None of these seem to indicate any major issues with the indentations, but a significant degree of mounding is readily observed. Based on AMF height data shown in Figure 37, the Berkovich impression has a mounding height of about 37nm and a residual indentation depth of about 54nm. The geometry of the mounding with edges apparently parallel to the $\langle 100 \rangle$ directions confirms the (001) crystal orientation. Comparable micrographs of nanoindentation impressions for PMN-30%PT were not located in the literature.

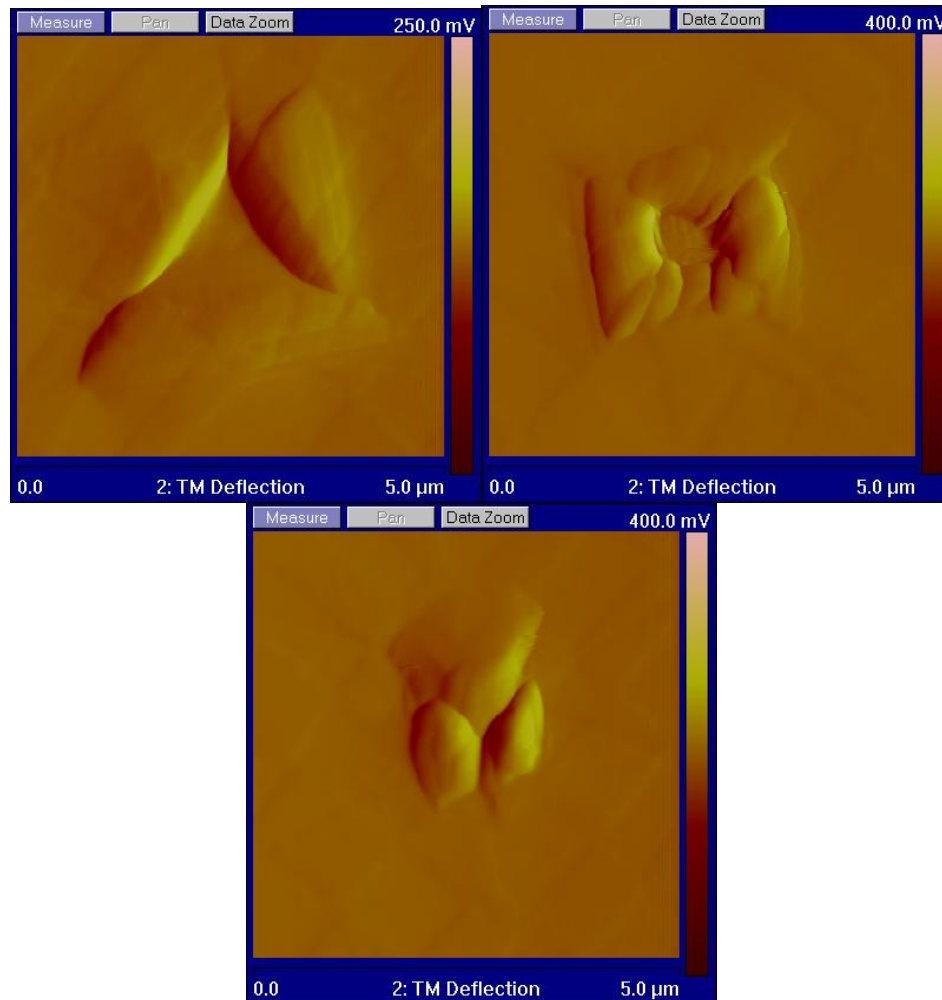


Figure 36. AFM micrographs for PMN-30%PT

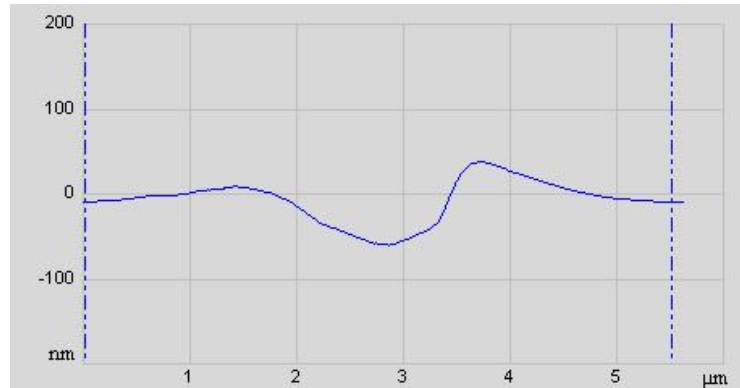


Figure 37. Cross section view of a Berkovich indentation in PMN-30%PT

The results of the nanoindentation experiments for (001) PMN-30%PT are shown in Figure 38. Considering only the data itself for now, there are several important observations. The Berkovich and cube corner indentation data sets are in very good agreement with each other over the entire range of contact radii tested. The cone data set behaves the same for the first three data points as it has for all materials tested, but it begins to deviate from the Berkovich and cube corner data for contact radii greater than about 200nm. The cause of this behavior is uncertain, as it is not observed in the other materials and mounding would not be expected to cause such a severe deviation. There is still some overlap in the error bars of one standard deviation between all the indenters for the PMN-30%PT, so while unexpected, the cone data is not excessively troublesome.

All indenters show a clear size effect, but not exactly in the manner observed for LiNbO_3 and LiTaO_3 . The piezoelectric indentation coupling constant C_1^* was calculated as either $2.17 \times 10^{11} \text{ N/m}^2$ or $2.15 \times 10^{11} \text{ N/m}^2$ based on data for 29% and 30% lead titanate crystals, respectively. There is essentially no difference between these values and both estimate a constant ratio of contact stiffness to contact radius for purely piezoelectric

indentation of about $1.38 \times 10^{11} \text{ N/m}^2$ as plotted in Figure 38. This value clearly underestimates the observed ratio of contact stiffness to contact radius by about one half.

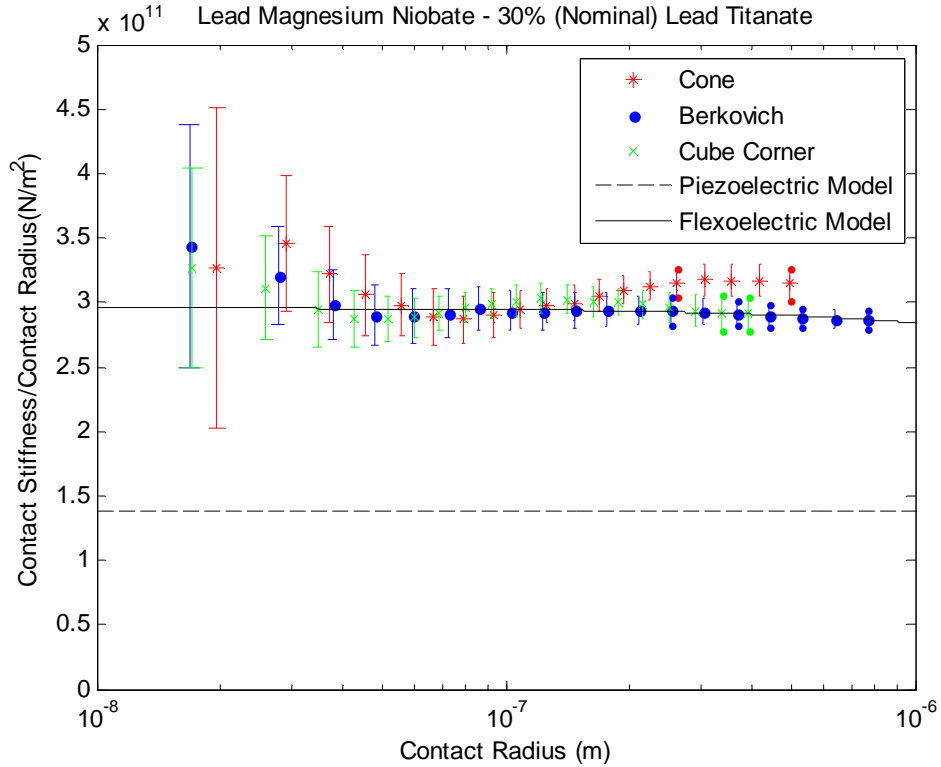


Figure 38. Indentation results for PMN-30%PT

In preparation for application of the flexoelectric model, the constants $A^i = 3.3733$ and $d^* = 12.1667 \text{ C/m}^2$ are calculated for PMN-29%PT, and $A^i = 4.2527$ and $d^* = 14.3667 \text{ C/m}^2$ are calculated for PMN-30%PT. These inputs combined with the Berkovich indentation data yield the fit parameters and flexoelectric estimates given in Table 9. Note that C_1^* is not a fitting parameter here since it already predicts a lower ratio of contact stiffness to contact radius than is actually observed in the data.

Table 9. Flexoelectric estimation results for PMN-30%PT

Composition	f_1^*	ε_1	f_{ij}
PMN-29%PT	$-4.96 \times 10^{11} N/m^2$	$1.44 \times 10^{-5} m$	$1.8 \times 10^{-4} C/m$
PMN-30%PT	$-4.96 \times 10^{11} N/m^2$	$2.13 \times 10^{-5} m$	$3.1 \times 10^{-4} C/m$

The f_1^* values are essentially identical, but the ε_1 and thus the flexoelectric estimates vary somewhat in their values depending on which set of material constants is used. The 29%PT case is plotted in Figure 38. Considering the capabilities of the flexoelectric model itself, the two estimates using constants for 29%PT and 30%PT are in good agreement with one another. To assess the quality of these estimates, first consider the magnitude of other strongly flexoelectric materials. Ceramic $Ba_{0.67}Sr_{0.33}TiO_3$ appears to possess the strongest flexoelectric properties of any material reported in the literature. At room temperature, where its relative dielectric permittivity nears its peak, most estimates indicate $f_{ij}^{BST} \approx 1.2 \times 10^{-4} C/m$ [15-17]. The estimates for f_{ij}^{PMNT30} presented here correspond well with this figure and indicate that PMN-30%PT is likely comparable to $Ba_{0.67}Sr_{0.33}TiO_3$ in terms of the magnitude of its flexoelectric constants at room temperature. This is an exciting observation considering the growing interest in manufacturing PMN-PT crystals for the next generation of high performance piezoelectrics. A second way to assess the f_{ij}^{PMNT30} estimate here is to consider how it compares with another composition of the same material. The flexoelectric properties of PMN-10%PT have been determined to be on the order of $f_{ij}^{PMNT10} \approx 10^{-5} C/m$. While this value is an order of magnitude smaller than the estimate here for PMN-10%PT, such a difference is not farfetched. Compositions of PMN-PT close to the morphotropic phase

boundary of about 34%PT (see section 2.6.4) can exhibit greatly enhanced dielectric, piezoelectric, and electromechanical coupling constants [94]. Such a pattern may very well apply to flexoelectric properties as well.

A reasonable concern in basing the flexoelectric estimate for PMN-30%PT on the Berkovich data in Figure 38 is that the ratio of contact stiffness to contact radius does not appear to drop appreciably at the larger contact radii. To determine whether more data points at larger contact radii would affect the estimation of f_{ij} , a batch of Berkovich indentations was conducted on the PMN-30%PT crystal with a maximum indentation depth of 2500nm. This increase in indentation depth offers data for effective contact radii up to about 4000nm as shown in Figure 39. The flexoelectric model plotted in the figure is fit to the deep Berkovich indentation data using material constants for PMN-29%PT and yields $f_{ij}^{PMN30} \approx 1.9 \times 10^{-4} C/m$, which is remarkably close the estimate based on the 400nm deep indentations. Figure 39 shows excellent agreement between the experimental data and the fitted analytical model for all but the first two data points, which raises an interesting issue. The data points representing contact radii less than about 50nm trend upward with decreasing contact radii much in the same manner as was observed in LiNbO_3 , LiTaO_3 , and SrTiO_3 . It seems reasonable that these data points could represent a material response not readily predictable by the model due to the neglect of higher order terms in the derivation of Eqn. 65. If this were the case, it would explain why the model excellently fits the deep indentation data for strongly flexoelectric PMN-30%PT but only adequately describes the behavior of LiNbO_3 and LiTaO_3 .

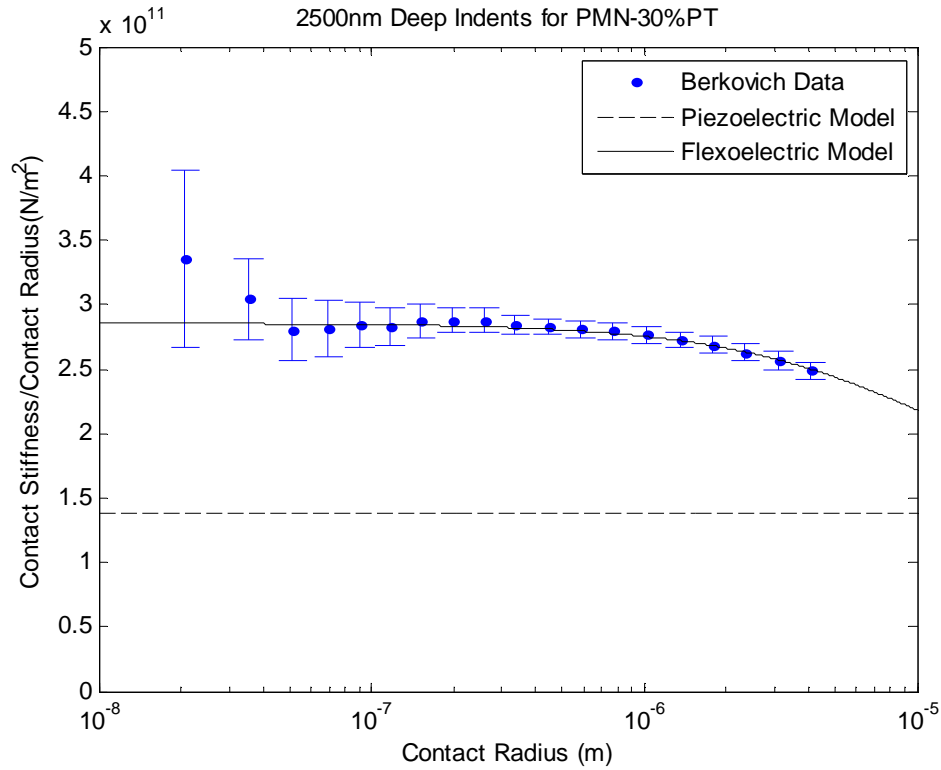


Figure 39. Results of deep Berkovich indentation tests for PMN-30%PT

4.5 Barium Titanate (BaTiO₃)

Representative atomic force micrographs of the residual Berkovich, cone, and cube corner indentations in the (001) BaTiO₃ crystal are shown in Figure 40. None of these seem to indicate any major issues with the indentations, and the anisotropic geometry of the mounding with edges parallel to the <100> directions is agrees with the (001) crystal orientation. Note however that the degree of mounding is greater than with all previous crystals. Based on AMF height data shown in Figure 41, the Berkovich impression has a mounding height of about 66nm and a residual indentation depth of about 130nm.

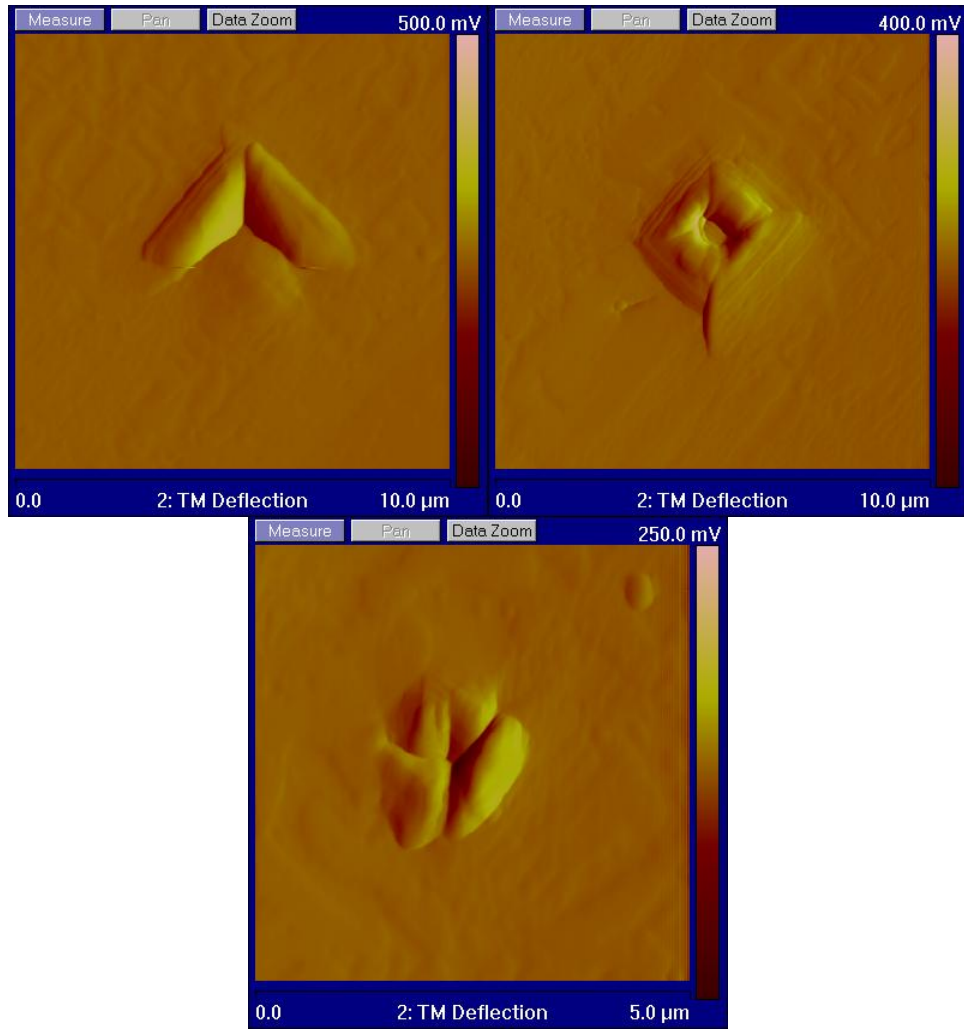


Figure 40. AFM micrographs for BaTiO₃

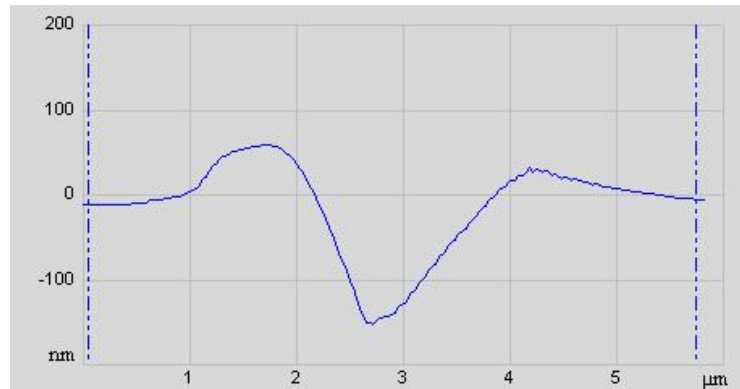


Figure 41. Cross section view of a Berkovich indentation in BaTiO₃

The results of the nanoindentation experiments for (001) BaTiO₃ are shown in Figure 42. All of the data sets indicate a higher ratio of contact stiffness to contact radius than predicted by the piezoelectric indentation model. Based on the material constants for BaTiO₃ in Table 5, the piezoelectric coupling constant is $C_1^* = 4.03 \times 10^{11} \text{ N/m}^2$. This value agrees with that reported by Karapetian et al. [77] for BaTiO₃. In the absence of flexoelectricity it is anticipated that

$$\frac{s}{a} = \frac{2}{\pi} C_1^* = 2.57 \times 10^{11} \text{ N/m}^2.$$

This is the value plotted for the piezoelectric model in Figure 42, and it clearly does not describe the observed indentation response.

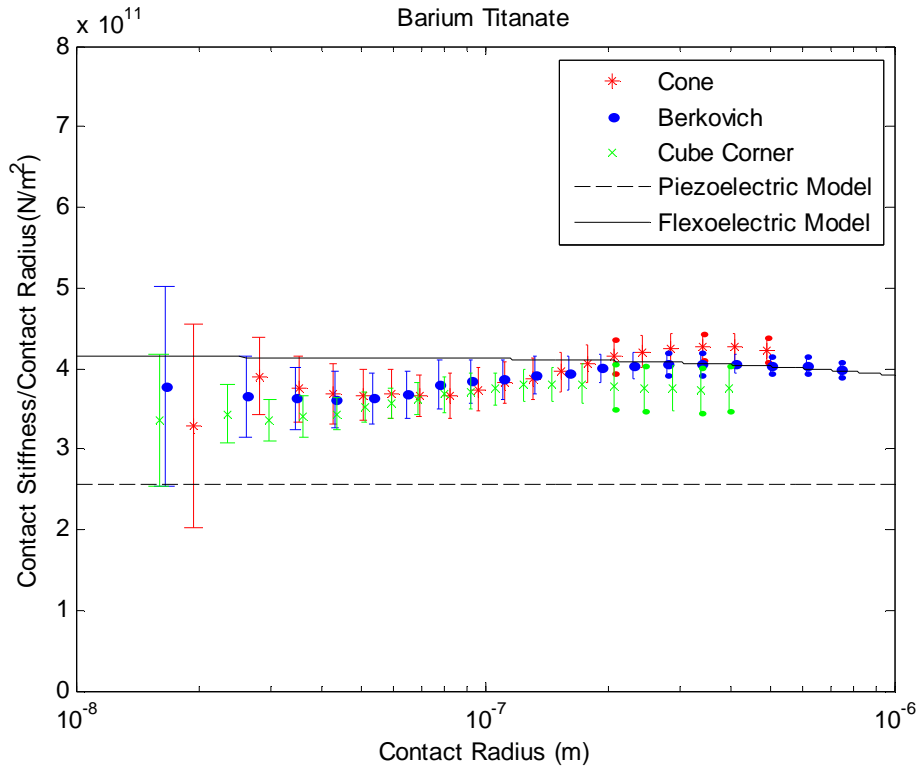


Figure 42. Indentation results for BaTiO₃

Another interesting feature of all the BaTiO₃ data sets is that the ratio of contact stiffness to contact radius for each indenter remains essentially constant for contact radii less than about 60nm, but then increases slightly with contact radius briefly before beginning the downward trend. Mounding around the indenter is a likely contributing factor to this behavior, given the observations from the AFM micrographs.

Direct comparison between the present data and that previously reported by Gharbi et al. [1] (see Figure 18) is somewhat problematic but reveals some discrepancies. The normalized stiffness data points in the present study extend to much larger contact radii before declining in their value than the data points in Ref. [1]. After a great deal of contemplation, the source of this disagreement is uncertain. There no known extraordinary differences between the test methods in the previous and current work, and it is noteworthy that the crystal samples for both studies were obtained from the same source, albeit several years apart. The excellent agreement between the indentation results for quartz in the current and previously reported work also seems to help quell any concern regarding the validity of the present testing setup and methods. Having no satisfactory explanation for the disagreement between the previous and current data, the flexoelectric estimation here has been performed with the concession that the final result is inconsistent with those previously reported.

The constants $A^i = 4.2150$ and $d^* = 11.5333C/m^2$ are calculated in preparation for application of the flexoelectric model for BaTiO₃. These inputs combined with the Berkovich indentation data yield the fit parameters and flexoelectric estimate given in Table 10. The result for f_1^* is on the order of that previously reported [2] and is perfectly reasonable if the initial sections of the current and previous flexoelectric model plots are

compared. Corresponding to the discrepancy between the present and previously reported data at contact radii greater than about 100nm, the current flexoelectric estimate $f_{ij}^{BaTiO_3}$ is about an order of magnitude greater than that found by Gharbi et al. [2] and those determined by bending experiments [13].

Table 10. Flexoelectric estimation results for BaTiO₃

f_1^*	ϵ_1	f_{ij}
$-4.96 \times 10^{11} N/m^2$	$8.51 \times 10^{-6} m$	$9.8 \times 10^{-5} C/m$

As was done with the PMN-30%PT crystal, to ensure that the data points at larger contact radii drop toward the predicted ratio of contact stiffness to contact radius, 2500nm deep Berkovich indentations were performed on another BaTiO₃ crystal as well as another quartz crystal. These results are shown in Figure 43. The ratio of contact stiffness to contact radius for quartz is again essentially constant, but BaTiO₃ clearly exhibits size dependency. While the data between the BaTiO₃ crystals in Figures 42 and 43 behave somewhat differently for contact radii less than about 100nm, for the larger contact radii they are essentially the same. It is also noteworthy that the BaTiO₃ crystal used for the deeper indentations exhibits the decreasing trend in the first few data points as was observed for the PMN-30%PT crystal.

It must be noted here that although the deep indentations were not imaged by AFM, some fracture is almost certainly taking place in the crystal for indentations greater than several hundred nanometers in depth. Liu et al. [99] have demonstrated that indentation of (001) BaTiO₃ with a conical (~1μm tip radius, 45° face to centerline angle) indenter may result in microcracks at indentation depths as low as 100nm. Fracture is of

course not taken into account by the flexoelectric indentation model, but the results in Ref. [1] seem to indicate that for effective contact radii up to about 500nm during Berkovich indentation (likely corresponding to an indentation depth of roughly 150nm), microcracks should present no obvious problems. For larger contact radii the manner and degree that microcracking affects application of the flexoelectric model is uncertain.

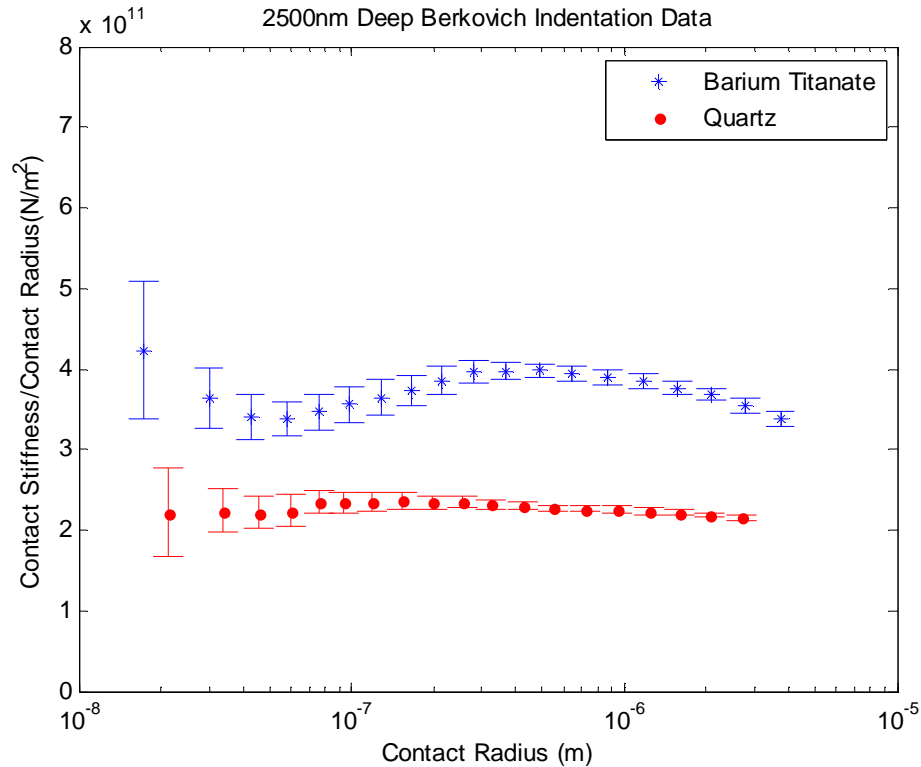


Figure 43. Comparison of deep Berkovich indentation results for quartz and BaTiO₃

While it is unfortunate that the experimental data and hence the flexoelectric estimate here for BaTiO₃ do not agree better with previous work, the big picture remains unchanged. All data sets indicate that the actual ratio of contact stiffness to contact radius is greater than would be expected if flexoelectric effects are completely neglected. The flexoelectric indentation model accounts for this behavior and provides the best explanation for the indentation size effect in the piezoelectric crystals examined here.

Chapter 5 Summary and Conclusions

A combined experimental-analytical approach based on nanoindentation techniques has been used to characterize flexoelectric properties of five piezoelectric crystals. Nanoindentation tests were performed using indenters of Berkovich, cone, and cube corner geometry on single crystal samples of z-cut quartz, z-cut LiTaO₃, z-cut LiNbO₃, <001> 0.7Pb(Mg_{1/3}Nb_{2/3})O₃-0.3(PbTiO₃), and poled <001> BaTiO₃. By applying an analytical indentation model incorporating flexoelectric effects the experimental data for these materials, it is possible to estimate the magnitude of their flexoelectric properties. The major conclusions of this work are as follows:

1. Quartz does not exhibit any significant indentation size effect attributable to flexoelectricity for effective contact radii as low as about 20nm. This result is consistent with previously reported data for quartz and indicates that quartz is very weakly flexoelectric. The indentation behavior of quartz precludes numerical estimation of its flexoelectric properties by application of the indentation model.
2. Lithium niobate exhibits an indentation size effect for effective contact radii less than about 70nm. Fitting the flexoelectric indentation model to the Berkovich data yields an estimate of the flexoelectric properties $f_{ij}^{LiNbO_3} \approx 1.0 \times 10^{-8} C/m$. This estimate is reasonable considering the magnitude of LiNbO₃'s dielectric properties (which are accepted to scale with flexoelectric properties) and using the phenomenological estimate $e/a \approx 3 \times 10^{-10} C/m$ and estimates for BaTiO₃ ($f_{ij}^{BaTiO_3} \approx 4 \times 10^{-6} C/m$) as justifiable upper and lower bounds.

3. Lithium tantalate also exhibits an indentation size effect for effective contact radii less than about 70nm. Fitting the flexoelectric indentation model to the Berkovich data yields an estimate of the flexoelectric properties $f_{ij}^{LiTaO_3} \approx 2.3 \times 10^{-9} C/m$. This estimate is reasonable considering the structural similarities between $LiTaO_3$ and $LiNbO_3$ as well as the similarities between the indentation data for these two materials. However, the flexoelectric model fits the data for $LiNbO_3$ better than the data for $LiTaO_3$, possibly indicating a somewhat higher degree of accuracy for the former estimate.

4. Nanoindentation data for paraelectric (non-piezoelectric) $SrTiO_3$, obtained in the same manner as with the other crystals, exhibits a size effect remarkably similar to those observed in $LiNbO_3$ and $LiTaO_3$. Flexoelectric tensor components for $SrTiO_3$ are known from bending experiments to be on the order of $10^{-9} - 10^{-8} C/m$. These indentation results for $SrTiO_3$ greatly support the argument that the type of indentation size effect discussed here is due to flexoelectricity as well as the notion that the aforementioned flexoelectric estimates for $LiNbO_3$ and $LiTaO_3$ are quite reasonable. The flexoelectric indentation model cannot be applied to $SrTiO_3$ because it is non-piezoelectric.

5. Based on the findings with $SrTiO_3$, even in the absence of a suitable electromechanically coupled indentation model, the perception of a flexoelectric size effect alone may provide some idea as to the potential magnitude of f_{ij} for a given material. Nanoindentation data may be used as a litmus test to select

materials as candidates for flexoelectric characterization by less convenient but more precise methods, e.g., flexure tests.

6. The PMN-30%PT (nominal composition) crystal exhibits an indentation size effect for effective contact radii up to and greater than 1000nm. Using material constants for 29%PT and fitting the flexoelectric indentation model to the Berkovich data yields an estimate of the flexoelectric properties $f_{ij}^{PMNT30} \approx 1.8 \times 10^{-4} C/m$. This estimate does not change dramatically if based on material properties for exactly 30%PT or when using data for deeper indentations. The estimate indicates PMN-30%PT could be up to an order of magnitude more flexoelectric than PMN-10%PT and about as strongly flexoelectric as $Ba_{0.67}Sr_{0.33}TiO_3$ ceramic. Currently, $Ba_{0.67}Sr_{0.33}TiO_3$ appears to possess the largest known room temperature flexoelectric constants of any crystalline dielectric, and so PMN-30%PT should make an excellent candidate for more precise flexoelectric characterization methods such as flexure experiments.
7. Barium titanate also exhibits an indentation size effect for effective contact radii up to and greater than 1000nm. However, the indentation data here, and hence the flexoelectric estimate for $BaTiO_3$, do not agree completely with previously reported behavior [2,13]. The estimate $f_{ij}^{BaTiO_3} \approx 9.8 \times 10^{-5} C/m$ based on the current data is about an order of magnitude greater than anticipated. After much contemplation, the source of the discrepancy between the previous and present data could not be determined. The excellent agreement between the present and previously reported data for Z-cut quartz implies the issue is not likely related to

the experimental setup and methods employed in this study. It is not thought that the results here for BaTiO₃ greatly implicate the flexoelectric estimates for the other crystals.

8. The piezoelectric-only indentation model [77] does not accurately predict the stiffness behavior exhibited by LiTaO₃, LiNbO₃, PMN-30%PT, or BaTiO₃. For LiTaO₃ and LiNbO₃ the piezoelectric model anticipates a larger ratio of contact stiffness to contact radius than is actually observed at larger contact radii. PMN-30%PT, or BaTiO₃ the piezoelectric model anticipates a smaller ratio of contact stiffness to contact radius than is actually observed for all contact radii investigated, presumably due to the enhanced flexoelectric properties in these materials. In all cases the piezoelectric model cannot predict the flexoelectric indentation size effect. The piezoelectric indentation model is not directly applicable to quartz due to its piezoelectric tensor.
9. In all AFM micrographs of residual indentations as well as the indentation data sets there is evidence of mounding occurring as the indentation proceeds. Mounding leads to some underestimation of actual contact area and hence overestimation of the ratio of contact stiffness to effective contact radius. It likely causes the appearance of a brief upward trend in plots of the ratio of contact stiffness to contact radius versus contact radius. The severity of the mounding effect varies by material with quartz exhibiting the least mounding and BaTiO₃ exhibiting the most.

10. In general, differences between indentation data sets obtained with different indenters for the same sample are explicable in terms of the observed mounding and anticipated stress fields and hardness models associated with the indenter geometries.
11. There do not appear to be any major problems associated with using f_1^* in addition to ε_1 as a fit parameter when applying the flexoelectric indentation model to the nanoindentation data since the value of f_1^* does not directly impact the flexoelectric estimate f_{ij} . For cases where the piezoelectric-only indentation model predicts a greater ratio of contact radius to contact radius than is actually observed, it appears acceptable to employ C_1^* as an additional fitting parameter to help ensure convergence. As the number of fit parameters increases from one to three, bounds and initial estimates selected during the fitting procedure become critically important.
12. The nanoindentation based analytical-experimental approach used here is a useful tool for estimating flexoelectric properties of piezoelectric crystals belonging to classes where the required piezoelectric stress constants are nonzero and where the required piezoelectric, dielectric, and elastic stiffness constants are known. Obviously these criteria somewhat limit the versatility of the approach. Some steps to extract f_{ij} from the raw indentation data can be somewhat tedious, e.g., the calculations required to determine C_1^* for a given material are quite cumbersome. Despite these perceived shortcomings, the approach here is

straightforward and requires relatively little in terms of experimental setup and sample preparation aside from access to a serviceable nanoindentation system.

The present work indicates there is great opportunity for future work dealing with both the experimental and analytical facets of flexoelectric estimates based on nanoindentation. Issues which may be of interest to investigate in future works include the following:

1. Further study of BaTiO₃ is required to understand the source of discrepancy between the data obtained in this study and the data previously reported.
2. In the present work only one crystal orientation has been considered for each material. Even though the flexoelectric indentation model currently makes no distinction regarding crystal orientation in the resultant flexoelectric estimate f_{ij} , comparing the stiffness behavior and size effects between different orientations of the same crystal could be insightful. For example, in LiNbO₃, where conflicting hardness values from opposing faces of the same crystal have been documented, flexoelectric size effects may vary with the direction of loading during indentation.
3. The manner in which microcracking and dislocation activity complicate the electromechanically coupled stress field around an indenter during nanoindentation is still not well understood. These effects must clearly be taking place at large indentation depths (several hundred nanometers or more), and in strongly flexoelectric materials where size effects need be observed at large contact radii the significance of their impact is uncertain.

4. Some reworking of the flexoelectric indentation model to include higher order terms may improve the ability to fit the model to data where indentation size effects only occur at extremely small contact radii. Whether the effort to include these terms in the analysis would be justified by significant improvements in accuracy of the flexoelectric estimations, however, is questionable.
5. The potential for error in nanoindentation-based estimations of flexoelectric properties stemming from the flexoelectric indentation model's assumption of a flat punch indenter has not been quantified. Berkovich indenters and pyramidal indenters in general generate relatively complicated stress fields during indentation due to the presence of edges which act as stress concentrators. The manner in which indentation-based flexoelectric property estimates could be affected by the differences between strain gradients associated with flat punches and Berkovich indenters does not appear to be readily discernable from works currently available in the literature. While the previous work seems to indicate that there are no major issues associated with the flat punch assumption, the work here is less conclusive.
6. An overhaul of the flexoelectric indentation model so that it may be applied to non-piezoelectric dielectric materials would provide a greatly enhanced degree of practicality and versatility to the nanoindentation based flexoelectric estimation approach. Such advancement would allow for comparison between indentation-based flexoelectric estimates and estimates from other methods for a wider variety of materials, e.g. non-piezoelectric SrTiO_3 and $\text{Ba}_{0.67}\text{Sr}_{0.33}\text{TiO}_3$. Additionally, the new model could be useful with high temperature nanoindentation (a growing

research area, see Appendix A) to characterize temperature dependency of flexoelectric properties near phase transitions such as above and below the Curie temperature for BaTiO₃.

References

1. M. Gharbi, Z.H. Sun, P. Sharma, and K. White, "The origins of electromechanical indentation size effect in ferroelectrics," *Applied Physics Letters* 95 (2009) 142901.
2. M. Gharbi, Z.H. Sun, P. Sharma, K. White, and S. El-Borgi, "Flexoelectric properties of ferroelectrics and the nanoindentation size-effect," *International Journal of Solids and Structures* 48 (2011) 249–256.
3. M. S. Majdoub, P. Sharma, and T. Çagin, "Dramatic enhancement in energy harvesting for a narrow range of dimensions in piezoelectric nanostructures," *Physical Review B* 78 (2008) 121407R.
4. M. S. Majdoub, P. Sharma, and T. Cagin, "Enhanced size-dependent piezoelectricity and elasticity in nanostructures due to the flexoelectric effect," *Physical Review B* 77 (2008) 125424.
5. J. Y. Fu, W. Zhu, N. Li, N. B. Smith, and L. E. Cross, "Gradient scaling phenomenon in microsize flexoelectric piezoelectric composites," *Applied Physics Letters* 91 (2007) 182910.
6. N.D. Sharma, R. Maranganti, and P. Sharma, "On the possibility of piezoelectric nanocomposites without using piezoelectric materials," *Journal of the Mechanics and Physics of Solids* 55 (2007) 2328–2350.
7. M. S. Majdoub, R. Maranganti, and P. Sharma, "Understanding the origins of the

- intrinsic dead layer effect in nanocapacitors," *Physical Review B* 79 (2009) 115412.
8. G. Catalan, L. J. Sinnamon, and J. M. Gregg, "The effect of flexoelectricity on the dielectric properties of inhomogeneously strained ferroelectric thin films," *Journal of Physics: Condensed Matter* 16 (2004) 2253–2264.
 9. X. Wang, "Piezoelectric nanogenerators - harvesting ambient mechanical energy at the nanometer scale," *Nano Energy* 1 (2012) 13–24.
 10. J. Fousek, L.E. Cross, and D.B. Litvin, "Possible piezoelectric composites based on the flexoelectric effect," *Materials Letters* 39 (1999) 287–291.
 11. B. Chu, W. Zhu, N. Li, and E. L. Cross, "Flexure mode flexoelectric piezoelectric composites," *Journal of Applied Physics* 106 (2009) 104109.
 12. B. Chu, W. Zhu, N. Li, and E. L. Cross, "Flexoelectric Composite – A new Prospect for Lead-free Piezoelectrics," *Functional Material Letters* 3 (2010) 79-81.
 13. W. Ma and E. Cross, "Flexoelectricity of barium titanate," *Applied Physics Letters* 88 (2006) 232902.
 14. P. Zubko, G. Catalan, A. Buckley, P. R. L. Welche, and J. F. Scott, "Strain Gradient Induced Polarization in SrTiO₃ Single Crystals," *Physical Review Letters* 99 (2007) 167601.
 15. W. Ma and L. E. Cross, "Flexoelectric polarization of barium strontium titanate

in the paraelectric state," *Applied Physics Letters* 81 (2002) 3440-3442.

16. L. E. Cross, "Flexoelectric effects: Charge separation in insulating solids subjected to elastic strain gradients," *Journal of Materials Science* 41 (2006) 53–63.
17. J. Y. Fu, W. Zhu, N. Li, and L. E. Cross, "Experimental studies of the converse flexoelectric effect induced by inhomogeneous electric field in a barium strontium titanate composition," *Journal of Applied Physics* 100 (2006) 024112.
18. W. Ma and L. E. Cross, "Observation of the flexoelectric effect in relaxor $\text{Pb}(\text{Mg}_{1/3}\text{Nb}_{2/3})\text{O}_3$ ceramics," *Applied Physics Letters* 78 (2001) 2920-2921.
19. W. Ma and L. E. Cross, "Strain-gradient-induced electric polarization in lead zirconate titanate ceramics," *Applied Physics Letters* 82 (2003) 3293-3295.
20. P. Hana, "Study of Flexoelectric Phenomenon from Direct and from Inverse Flexoelectric Behavior of PMNT Ceramic," *Ferroelectrics* 351 (2007) 196–203.
21. F. J. Nye, Physical Properties of Crystals, Oxford University Press Inc., New York (1985).
22. B. Jaffe, W. Cook, Jr., and H Jaffe, Piezoelectric Ceramics, Academic Press Limited, Reprinted by R. A. N. Publishers, Marietta, OH (1971).
23. D. Damjanovic, "Ferroelectric, dielectric and piezoelectric properties of ferroelectric thin films and ceramics," *Reports on Progress in Physics* 61 (1998) 1267–1324.

24. Physics of Ferroelectrics: A Modern Perspective, Eds. K. Rabe, C. H. Ahn, and J.-M. Triscone, Springer-Verlag Berlin Heidelberg (2007).
25. G. H. Haertling, "Ferroelectric Ceramics: History and Technology," *Journal of the American Ceramic Society* 82 (1999) 797–818.
26. J. W. Waanders, Piezoelectric Ceramics – Properties and Applications, Philips Components, Eindhoven, The Netherlands (1991).
27. A. K. Tagantsev, V. Meunier, and P. Sharma, "Novel Electromechanical Phenomena at the Nanoscale: Phenomenological Theory and Atomistic Modeling," *MRS Bulletin* 34 (2009) 643-647.
28. K. B. Tolpygo, "Long Wavelength Oscillations of Diamond Type Crystals Including Long Range Forces," *Soviet Physics - Solid State* 4 (1963) 1297-1305.
29. V.S. Mashkevich and K. B. Tolpygo, "Electrical, Optical and Elastic Properties of Diamond Type Crystals," *Soviet Physics - JETP* 5 (1957) 435-439.
30. A. K. Tagantsev, "Piezoelectricity and flexoelectricity in crystalline dielectrics," *Physical Review B* 34 (1986) 5883-5889.
31. S. M. Kogan, "Piezoelectric Effect During Inhomogeneous Deformation and Acoustic Scattering of Carriers in Crystals," *Soviet Physics – Solid State* 5 (1964) 2069-2070.
32. W. Ma and L. E. Cross, "Large flexoelectric polarization in ceramic lead magnesium niobate," *Applied Physics Letters* 79 (2001) 4420-4422.

33. A. K. Tagantsev, "Electric polarization in crystals and its response to thermal and elastic perturbations," *Phase Transitions* 35 (1991) 119-203.
34. W. Ma and L. E. Cross, "Flexoelectric effect in ceramic lead zirconate titanate," *Applied Physics Letters* 86 (2005) 072905.
35. A.C. Fischer-Cripps, Nanoindentation, Springer-Verlag New York, Inc., New York (2002).
36. W.C. Oliver and G. M Pharr, "An improved technique for determining hardness and elastic modulus using load and displacement sensing indentation experiments," *Journal of Materials Research* 7 (1992) 1564-1583.
37. I. N. Sneddon, "The relation between load and penetration in the axisymmetric Boussinesq problem for a punch of arbitrary profile," *International Journal of Engineering Science* 3 (1965) 47-57.
38. M. F. Doerner and W.D. Nix, "A method for interpreting the data from depth-sensing indentation instruments," *Journal of Materials Research* 1 (1986) 601-609.
39. W. C. Oliver and J.B Pethica, "Methods for continuous determination of the elastic stiffness of contact between two bodies," U.S. Patent NO. 4,848,141, July 18th, 1989.
40. J. B. Pethica, R. Hutchings, and W.C. Oliver, "Hardness measurements at penetration depths as small as 20nm," *Philosophical Magazine A* 48 (1983) 593-

606.

41. X. Li and B. Bhushan, "A review of nanoindentation continuous stiffness measurement technique and its applications," *Materials Characterization* 48 (2002) 11-36.
42. Handbook of Micro/Nano Tribology, Ed. B. Bhushan, CRC Press, Inc., Boca Raton, FL (1995).
43. "How to select the correct indenter tip," Agilent Technologies, Inc., Application Note (2009).
44. A. C. Fischer-Cripps, "Critical review of analysis and interpretation of nanoindentation test data," *Surface and Coatings Technology* 200 (2006) 4153-4165.
45. D.F. Bahr, S.L. Jennerjohn, and D.J. Morris, "Dislocation nucleation and multiplication in small volumes: the onset of plasticity during indentation testing," *Journal of Materials Science* 61 (2009) 56-60.
46. D. Lorenz, A. Zeckzer, U. Hilpert, P. Grau, H. Johansen, and H. S. Leipner, "Pop-in effect as homogeneous nucleation of dislocations during nanoindentation," *Physical Review B* 67, (2003) 172101.
47. K. Durst, B. Backes, O. Franke, and M. Göken, "Indentation size effect in metallic materials: modeling strength from pop-in to macroscopic hardness using geometrically necessary dislocations," *Acta Materialia* 54 (2006) 2547–2555.

48. N. Stelmashenko, M. Walls, L. Brown and Y. Milman, "Microindentations on W and Mo oriented single crystals: an STM study," *Acta Metallurgica et Materialia* 41, (1993) 2855-2865.
49. M. De Guzman, G. Neubauer, P. Flinn, W. Nix, "The role of indentation depth on the measured hardness of materials," *Materials Research Society Symposium Proceedings* 308, (1993) 613–618.
50. Q. Ma and D. Clarke, "Size dependent hardness of silver single crystals," *Journal of Materials Research* Vol. 10 (1995) 853-863.
51. W. Poole, M. Ashby, and N. Fleck, "Micro-hardness of annealed and work-hardened copper polycrystals," *Scripta Materialia* 34 (1996) 559–564.
52. W. Nix and H. Gao, "Indentation size effects in crystalline materials: A law for strain gradient plasticity," *Journal of the Mechanics and Physics of Solids* Vol 46 NO. 3 (1998) 411-425.
53. J. Swadener, E. George, and G. Pharr, "The correlation of the indentation size effect measured with indenters of various shapes," *Journal of the Mechanics and Physics of Solids* 50 (2002) 681 – 694.
54. G. Feng and W. Nix, "Indentation size effect in MgO," *Scripta Materialia* 51 (2004) 599–603.
55. R. K. A. Al-Rub, "Prediction of micro and nanoindentation size effect from conical or pyramidal indentation," *Mechanics of Materials* 39 (2007) 787–802.

56. R. K. Abu Al-Rub and G. Z. Voyiadjis, "Analytical and experimental determination of the material intrinsic length scale of strain gradient plasticity theory from micro- and nano-indentation experiments," *International Journal of Plasticity* 20 (2004) 1139–1182.
57. I. Manika, and J. Maniks, "Size effects in micro- and nanoscale indentation," *Acta Materialia* 54 (2006) 2049–2056.
58. K. Durst, B. Backes, and M. Göken, "Indentation size effect in metallic materials: correcting for the size of the plastic zone," *Scripta Materialia* 52 (2005) 1093.
59. G. M. Pharr, E. G. Herbert, and Y. Gao, "The indentation size effect: a critical examination of experimental observations and mechanistic interpretations," *Annual Review of Materials Research* 40 (2010) 271-292 .
60. Y. Huang, F. Zhang, K. Hwang, W. Nix, G. Pharr, and G. Feng, "A model of size effects in nanoindentation," *Journal of the Mechanics and Physics of Solids* 54 (2006) 1668–1686.
61. J. Alkorta, J. M. Martinez-Esnaola, and J. Gil Sevillano, "Detailed assessment of indentation size-effect in recrystallized and highly deformed niobium," *Acta Materialia* 54 (2006) 3445–3452.
62. M. Zhao, W. Slaughter, M. Li, and S. X. Mao, "Material length-scale-controlled nanoindentation size effects due to strain-gradient plasticity," *Acta Materialia* 51

(2003) 4461–4469.

63. W. Yang, B.C. Larson, G. M. Pharr, G. E. Ice, J. D. Budai, et al., "Deformation microstructure under microindents in single-crystal Cu using three-dimensional X-ray structural microscopy," *Journal of Materials Research* 19 (2004) 66–72.
64. E. Demir, D. Raabe, N. Zaafarani, and S. Zaefferer, "Investigation of the indentation size effect through the measurement of the geometrically necessary dislocations beneath small indents of different depths using EBSD tomography," *Acta Materialia* 57 (2009) 559–69.
65. K.K. McLaughlin, W. J. Cleg, "Deformation underneath low-load indentations in copper," *Journal of Physics D* 41 (2008) 074007.
66. D.S. Balint, V. Deshpande, A. Needleman, and E. Van DerGiessen, "Discrete dislocation plasticity analysis of the wedge indentation of films," *Journal of the Mechanics and Physics of Solids* 54 (2006) 2281–303.
67. HGM Kreuzer and R. Pippan, "Discrete dislocation simulation of nanoindentation: indentation size effect and the influence of slip band orientation," *Acta Materialia* 55 (2004) 3229–3235.
68. HGM Kreuzer, and R. Pippan, "Discrete dislocation simulation of nanoindentation: the effect of moving conditions and indenter shape," *Mater. Sci. Eng. A* 387–89 (2004) 254–256.
69. M. Rester, C. Motz, and R. Pippan, "Microstructural investigation of the volume

- beneath nanoindentations in copper," *Acta Materialia* 55 (2007) 6427–6435.
70. T. Scholz, J. Muñoz-Saldaña, M. V. Swain, and G. A. Schneider, "Indentation size effect in barium titanate with spherical tipped nanoindenters," *Applied Physics Letters* 88 (2006) 091908.
 71. R. Buchs, S. Basu, O. A. Elshrief, R. Coward, and M. W. Barsoum, "Spherical nanoindentation and Vickers microhardness study of the deformation of poled BaTiO₃ single crystals," *Journal of Applied Physics* 105 (2009) 093540.
 72. A. Hurtado-Macias, J. Muñoz-Saldaña, F. J. Espinoza-Beltrán, T. Scholz, M. V. Swain, and G. A. Schneider, "Indentation size effect in soft PZT ceramics with tetragonal structure close to the MPB," *Journal of Physics D* 41 (2008) 035407.
 73. S. Bhagavat and I. Kao, "Nanoindentation of lithium niobate: hardness anisotropy and pop-in phenomenon," *Materials Science and Engineering A* 393 (2005) 327–331.
 74. Piezoelectricity: Evolution and Future of a Technology, Eds. W. Heywang, K. Lubitz, and W. Wersing, Springer-Verlag Berlin Heidelberg (2008).
 75. M. E. Lines and A. M. Glass, Principles and Applications of Ferroelectrics and Related Materials, Oxford University Press, Oxford (1977).
 76. S. Basu, A. Zhou, and M. W. Barsoum, "Reversible dislocation motion under contact loading in LiNbO₃ single crystal," *Journal of Materials Research* 23 (2008) 1334-1338.

77. E. Karapetian, M. Kachanov, and S. V. Kalinin, "Nanoelectromechanics of piezoelectric indentation and applications to scanning probe microscopies of ferroelectric materials," *Philosophical Magazine* Vol. 85 NO. 10 (2005) 1017-1051.
78. M.H. Holmes, Introduction to Perturbation Methods, Springer-Verlag New York, Inc., New York (1995).
79. K. Durst, O. Franke, A. Böhner, and M. Göken, "Indentation size effect in Ni-Fe solid solutions," *Acta Materialia* 55 (2007) 6825–6833.
80. G. M. Pharr, J. H. Strader, and W. C. Oliver, "Critical issues in making small-depth mechanical property measurements by nanoindentation with continuous stiffness measurement," *Journal of Materials Research* 24 (2009) 653-666.
81. R. C. Bradt and G. S. Ansell, "Dislocations and 90° Domains in Barium Titanate," *Journal of Applied Physics* 38 (1967) 5407.
82. T. Scholz, K. K. McLaughlin, F. Giuliani, W. J. Clegg, F. J. Espinoza-Beltrán et al., "Nanoindentation initiated dislocations in barium titanate (BaTiO₃)," *Applied Physics Letters* 91 (2007) 062903.
83. J. Hong, G. Catalan, J. F. Scott, and E. Artacho, "The flexoelectricity of barium and strontium titanates from first principles," *Journal of Physics: Condensed Matter* 22 (2010) 112201.
84. K. G. Subhadra, K. K. Rao and D. B. Sirdeshmukh, "Systematic hardness studies

- on lithium niobate crystals," *Bulletin of Materials Science* Vol. 23 NO. 2 (2000) 147–150.
85. B. Anasori, K. E. Sickafus, I. O. Usov, and M. W. Barsoum, "Spherical nanoindentation study of the deformation micromechanisms of LiTaO_3 single crystals," *Journal of Applied Physics* 110 (2011) 023516.
 86. S.-E. E. Park and W. Hackenberger, "High performance single crystal piezoelectrics: applications and issues," *Current Opinion in Solid State and Materials Science* 6 (2002) 11–18.
 87. W. Guo, D. Jin, W. Wei, and H. J. Maris, "Low temperature piezoelectric and dielectric properties of lead magnesium niobate titanate single crystals," *Journal of Applied Physics* 102 (2007) 084104.
 88. N. Di, J. C. Harker, and D. J. Quesnel, "Photoelastic effects in PMN-29%PT single crystals investigated by Hertzian contact experiments," *Journal of Applied Physics* 103 (2008) 053518.
 89. Y. Namba and H. Takahashi, "Ultra-precision surface grinding of PMN-PT relaxor-based ferroelectric single crystals," *Manufacturing Technology* 59 (2010) 589–592.
 90. J. K. Shang and X. Tan, "Indentation-induced domain switching in $\text{Pb}(\text{Mg}_{1/3}\text{Nb}_{2/3})\text{O}_3\text{-PbTiO}_3$ crystal," *Acta Materialia* 49 (2001) 2993–2999.
 91. X.L. Zhong, L. Lu, M.O. Lai, "Growth of highly orientated

- 0.65Pb(Mg_{1/3}Nb_{2/3})O₃-0.35PbTiO₃ films by pulsed laser deposition," *Surface & Coatings Technology* 198 (2005) 400– 405.
92. P. Delobelle, E. Fribourg-Blanc, and D. R emiens, "Mechanical properties determined by nanoindentation tests of Pb(Zr,Ti)O₃ and Pb(Mg_{1/3}Nb_{2/3})-xTiO₃ sputtered thin films," *Thin Solid Films* 515 (2006) 1385–1393.
93. P. Hana, M. Marvan, L. Burianova, S. J. Zhang, E. Furman, and T. R. Shrout, "Study of the inverse flexoelectric phenomena in ceramic lead magnesium niobate-lead titanate," *Ferroelectrics* 336 (2006) 137–144.
94. H. Cao, V. H. Schmidt, R. Zhang, W. Cao, and H. Luo, "Elastic, piezoelectric, and dielectric properties of 0.58Pb(Mg_{1/3}Nb_{2/3})O₃-0.42PbTiO₃ single crystal," *Journal of Applied Physics* 96 (2004) 549-554.
95. R. T Smith and F. S. Welsh, "Temperature dependence of the elastic, piezoelectric, and dielectric constants of lithium tantalate and lithium niobate," *Journal of Applied Physics* Vol. 42 NO. 6 (1971) 2219-2230.
96. Agilent Technologies, Inc., "Agilent Nano Indenter G200," Data Sheet (2011).
97. M. R. Van Landingham, T. F. Juliano, and M. J. Hagon, "Measuring tip shape for instrumented indentation using atomic force microscopy," *Measurement Science and Technology* 16 (2005) 2173–2185.
98. H. St ocker, M. Zschornak, T. Leisegang, I. Shakhverdova, S. Gemming, and D. C. Meyer, "Electric field mediated switching of mechanical properties of

strontium titanate at room temperature," *Crystal Research and Technology* 45 (2010) 13-17.

99. D. Liu, M. Chelf, and K.W. White, "Indentation plasticity of barium titanate single crystals: dislocation influence on ferroelectric domain walls," *Acta Materialia* 54 (2006) 4525–4531.

100. N. M. Everitt, M. I. Davies, and F. J. Smith, "High temperature nanoindentation - the importance of isothermal contact," *Philosophical Magazine* Vol. 91 (2011) 1221-1244.

101. K. Fröhlich, D. Machajdik, A. Rosová, I. Vávra, F. Weiss, B. Bochu, and J. P. Senateur, "Growth of SrTiO₃ thin epitaxial films by aerosol MOCVD," *Thin Solid Films* 260 (1995) 187-191.

Appendix A – High Temperature Nanoindentation

Estimation of flexoelectric properties of solid crystalline dielectrics at elevated temperatures is of great interest for various reasons. For example, dielectric properties of materials such as PMN and BaTiO₃ can increase dramatically in the vicinity of the ferroelectric phase transition, and since flexoelectric properties scale with the dielectric susceptibility, flexoelectric properties may strengthen or diminish with temperature. Nanoindentation based estimations of flexoelectric properties of BaTiO₃ over a range of temperatures including the tetragonal to cubic (and hence non-piezoelectric) phase transition at about 130°C were of chief interest in this project, however a number of factors make such investigations exceedingly difficult. The intent of this section is to discuss nanoindentation experiments at elevated temperatures and difficulties encountered during high temperature nanoindentation work attempted in earlier stages of this project. Note that the term “high temperature” in the context of nanoindentation may be generally understood to refer to testing at any temperatures that deviating significantly, typically more than a few degrees, from normal room temperatures.

The common problem in nanoindentation tests at any non-ambient temperature is that transient heat transfer effects cause thermal “drift” or instability in the displacement measurements. More specifically, thermally induced expansion or contraction of the indentation system components is indistinguishable from true and intentional displacements into the sample surface. Since nanoindentation analysis is predicated on accurate knowledge of indenter geometry and depth of penetration into the sample surface (treated as a fixed reference point), even minute thermally induced dimensional

changes in the indenter or its support column may skew the experimental results. There have been many attempts at high temperature nanoindentation since the mid 1990's with varying degrees of success. Everitt et al. [100] has compiled an extensive list of these studies, and notes that generally two approaches are used to minimize transient thermal effects. In one approach the sample is heated on a heating stage and the indenter tip is brought into contact with the surface at a light nominal load for a long enough period of time that thermal equilibrium is achieved before the testing commences. In the other approach, both the sample and the indenter are heated individually to the same temperature before indentation proceeds. A light load hold segment may also be employed in these tests to further minimize thermal drift. Through their own nanoindentation experiments and finite element analysis (FEA), Everitt et al. [100] demonstrated that the latter approach is more favorable than the first, but neither is ideal. The major relevant findings of Everitt et al. [100] are as follows:

1. The FEA results indicate that for indentations where only the sample is heated, the entire system may reach thermal equilibrium relatively quickly, but the temperature at the indenter-sample interface and the volume of sample material adjacent to the interface should differ from the temperature of the bulk sample. This effect is more pronounced in materials of low thermal conductivity where the thermal gradients under the indenter are more diffuse.
2. Experimental results indicate that while nanoindentation without separate heating of the indenter itself may produce results that are acceptable (in terms of the thermal drift that is observed) for low loads and samples of low thermal

conductivity, the actual temperature of the indentation volume is still unknown.

3. For indentations where only the sample is heated, the changes in contact area that occur as the indentation commences may significantly disrupt thermal equilibrium, resulting in thermal drift and even more uncertainty regarding the true temperature of the indentation volume.

With regard to the present work, high temperature nanoindentation tests exceeding 100°C were carried out on fused silica and MgO samples using the Nano Indenter XP (MTS Nano Instruments, Oak Ridge, TN) indentation system and custom built heating stage. No separate heating of the indenter column was attempted because the Nano Indenter XP indenter column contains an epoxy joint that may not tolerate excessive heating. Standard test methods were modified so that a thermal drift threshold, calculated as the rate of change of raw displacement with respect to time, must be cleared during a constant load hold period before indentation proceeds. These methods proved ineffective, with nearly all load versus displacement curves indicating negative displacements and increasing loads in the holding segment. Such behavior, illustrated in Figure 44, indicates significant transient heat transfer from the sample through the diamond tip and indenter column due to increases in contact area as the indenter presses into the sample. This heat transfer results in thermal expansion of the indenter column and these displacements are impossible to distinguish from both those associated with material responses and those imposed by the indentation system. With separate heating of the indenter column out of the question, and considering the variety of issues addressed by Everitt et al. [100], sufficiently accurate nanoindentation testing at temperatures near

the ferroelectric phase transition of BaTiO₃ with the Nano Indenter XP does not appear feasible. Nanoindentation systems produced by Hysitron (Eden Prairie, MN, US) and Micro Materials Ltd. (Wrexham LL13 7YL, UK) appear better suited to high temperature testing, and have been used with varying degrees of success by many researchers listed in [100].

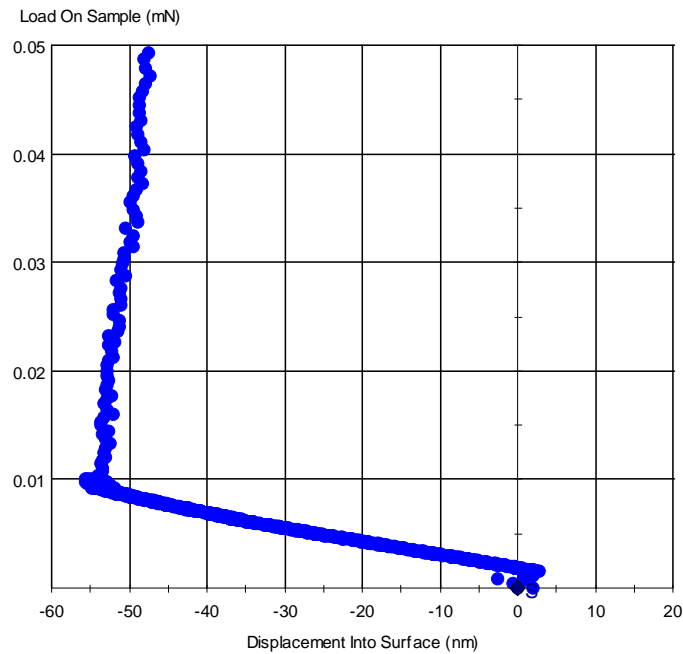


Figure 44. Nanoindentation at 120°C using the Nano Indenter XP and a custom heat stage

Appendix B – Mounding (Pile-up) Effects

As illustrated in Figure 13, mounding leads to underestimation of actual contact area during nanoindentation. Underestimation of contact area of course means effective contact radius is underestimated as well, and so the ratio of contact stiffness to contact radius may become artificially inflated. To establish the severity of these effects, percentages of underestimation of actual effective contact radius due to mounding of various heights have been calculated in Table 11 for actual indentation depths of 100nm and 400nm. The effective contact radii in the table are based on the Berkovich indenter area function in this work using displacement depths equal to the actual indentation depth plus the mounding height. Note that true mound height actually varies around the perimeter of contact during indentation, and so the heights in the table should be considered as effective values.

The degree of underestimation of the actual effective contact radius varies with the mounding as a percentage of the total indentation depth. For example, when the mounding height is 10% of the indentation depth (10nm for 100nm displacement into the surface and 40nm for 400nm of displacement into the surface) the effective contact radius determined during indentation reflects 91-92% of the actual effective contact radius. For mounding that approaches 25% of the actual displacement into the surface, calculated effective contact radii are about 80-81% of their true values. The scaling here ties to the geometric self similarity of the Berkovich indenter.

Table 11. Influence of mounding on the determination of effective contact radius

Actual displacement into surface (nm)	Mound Height (nm)	Effective Contact Radius (nm)	% of Actual Effective Contact Radius
100	0	315	100
	5	330	95
	10	344	92
	15	359	88
	20	373	84
	25	387	81
400	0	1171	100
	20	1228	95
	40	1285	91
	60	1341	87
	80	1398	84
	100	1455	80

Although the actual mounding heights that develop during the indentation tests are unknown, AFM height data from residual impressions imply that mounds significantly taller than about 70nm are unlikely to be encountered at the maximum indentation depth of 400nm in all materials here except BaTiO₃. Based on this observation and the calculations in Table 11, it is reasonable to expect that the effective Berkovich contact radii calculated for the five materials considered here do not deviate by more than 10-15% from their true values at any time during the indentation. This degree of variation should not affect the general behaviors observed in the normalized stiffness versus contact radius plots. If the plots could be corrected, the new graphs should simply appear elongated along the contact radius axis and shifted slightly downward along the stiffness axis. Such changes would not result in the disappearance of the size effects observed in LiNbO₃, LiTaO₃, PMN-30%PT, and BaTiO₃.

Appendix C – X-Ray Diffraction of SrTiO₃

A Siemens D5000 X-ray diffractometer was used to confirm the orientation of the SrTiO₃ crystal. For (001) oriented SrTiO₃, the highest intensity planes are (100), (200), and (300) [101]. Peaks for these planes occur at 22.8°, 46.5°, and 72.5°, respectively, according to PDF-2 database file 00-035-0734. The three highest peaks in the raw scan results in Figure 45 correspond well with those anticipated for (001) oriented SrTiO₃. The remaining peaks are attributable to the colloidal silver paste and steel AFM sample puck used for mounting the SrTiO₃ crystal. For example, according to PDF-2 database file 01-077-6577, (111), (200), and (220) are the highest intensity planes in silver powder samples and correspond to 38.4°, 44.5°, and 64.9°, respectively.

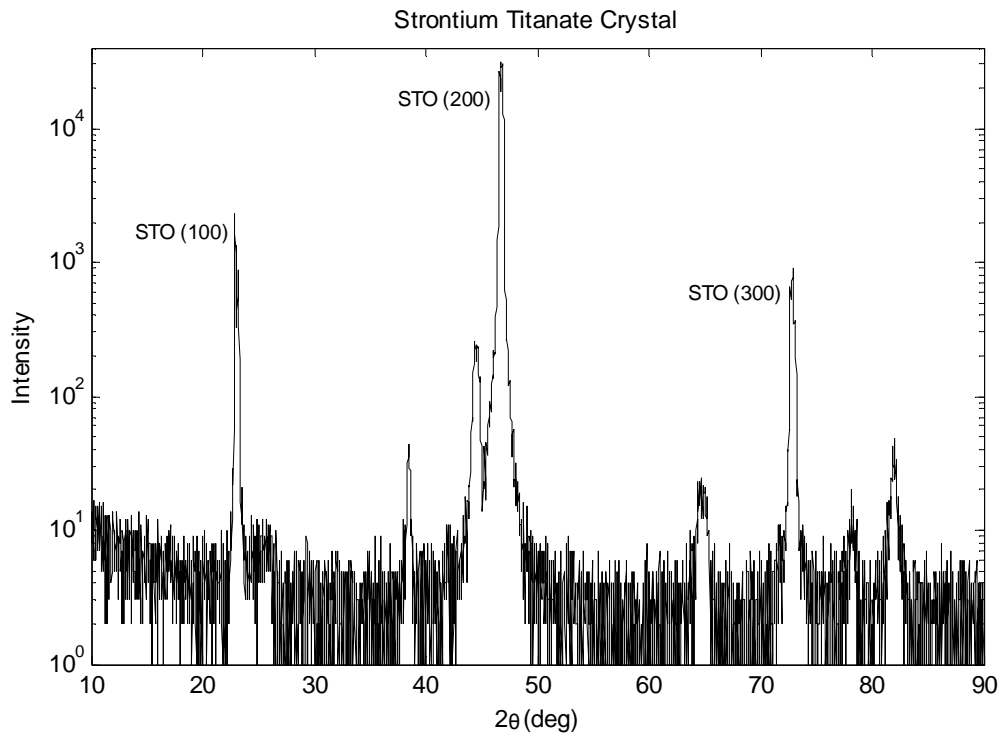


Figure 45. Raw X-ray diffraction data from test on SrTiO₃ crystal

